

**Studies on synchronisation and chimera states in
Hindmarsh-Rose networks with
distance-dependent and cross coupling schemes**

*Thesis submitted to the University of Calicut
in partial fulfillment of the requirements
for the award of the degree of*

Doctor of Philosophy in Physics

Under the Faculty of Science



T. Remi

Department of Physics

Farook College

Farook College Rd, Kozhikode, Kerala, 673632

March 2023

Acknowledgements

I would like to express my heartfelt gratitude to all those who have supported me throughout the journey of completing my thesis. I am truly grateful for the invaluable guidance and encouragement I received from my guide, Prof. P. A. Subha. Her unwavering support and belief in me was the driving force behind my success.

Its my pleasure to acknowledge Dr. K. M. Naseer, the Principal, Farook College, for his support in enabling me to complete my research. I would also like to extend my gratitude to the Mr. Midhun Shah, Head, Department of Physics, Farook College, for providing me with the resources and opportunities necessary to complete my research. Special mention to Dr. Sulfikar Ali, Research Coordinator, Department of Physics, Farook College. I am indebted to all the faculties of Department of Physics, Farook College for their cooperation.

I want to extend a special gratitude to Dr. K. Usha for effortlessly smoothing out the obstacles in my path and for being there with me through thick and thin. I would also like to extend my appreciation to my friends Amal and Thasneem for their support during difficult times and for sharing their valuable ideas and perspectives. Their contributions are invaluable and have greatly enriched the quality of my research. I am also grateful to Sreeshna for her assistance in the final stage of my thesis submission. I extend my heartfelt appreciation to the staffs in informatics centre, Farook College, for providing the technical support.

I am grateful to my family members who provided emotional support and

encouragement during the ups and downs of this journey. Their belief in me was a source of strength and motivation.

Finally, I would like to extend my gratitude to the University Grants Commission for the financial support in the form of the Maulana Azad National Fellowship. Their support was instrumental in making this project a reality.

Thank you to everyone who has been a part of this journey. I am deeply grateful for all your support.

T. Remi

CERTIFICATE

Certified that the work presented in this thesis titled 'Studies on synchronisation and chimera states in Hindmarsh-Rose networks with distance-dependent and cross coupling schemes' is a bonafide work done by Ms. T. Remi under my guidance in the Department of Physics, Farook College, University of Calicut and that this work has not been included in any other thesis submitted previously for the award of any degree.



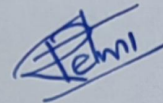
Prof. P. A. SUBHA
Research Supervisor
Department of Physics
Farook College
Kozhikode - 673 632.

Farook College

March 2023

DECLARATION

I hereby declare that the work presented in this thesis titled 'Studies on synchronisation and chimera states in Hindmarsh-Rose networks with distance-dependent and cross coupling schemes' is based on the original work done by me under the guidance of Prof. P. A. Subha, Department of Physics, Farook College, University of Calicut, and has not been included in any other thesis submitted previously for the award of any degree.



T. Remi

Research scholar

Dept. of Physics

Farook College

Farook College

March 2023

CERTIFICATE

This is to certify that the thesis titled 'Studies on synchronisation and chimera states in Hindmarsh-Rose networks with distance-dependent and cross coupling schemes' has been checked for plagiarism using ORIGINAL software at CHMK library, University of Calicut and found that the similarity index of the work is within acceptable limits fixed by the University.

Farook College

March 2023




Prof. P. A. SUBHA
Research Supervisor
Department of Physics
Farook College
Kozhikode - 673 632.

CERTIFICATE

This is to certify that the corrections/suggestions recommended by the adjudicators have been incorporated in the of PhD thesis of Ms.T. Remi, research scholar under my supervision and that the contents in the thesis and the soft copy are one and the same.

20.09.2023

FarookCollege



Prof. P. A. SUBHA
Research Supervisor
Department of Physics
Farook College
Kozhikode - 673 632.

ABSTRACT

The thesis presents the theoretical study of enhancing or suppressing synchrony and the emergence of chimera states in a network of Hindmarsh-Rose neurons, as a nonlinear system. Different methods have been employed to enhance the synchrony in the neural network owing to its vital role in signal transmission and memory processing. However, the unwanted synchrony among neurons results in several pathological conditions. Desynchrony is thought to be important for certain functions in the brain, such as attention and perception, because it allows different neural populations to process information independently and in a flexible manner. The coexistence of synchronised and desynchronised states is called chimera states. It was assumed that nonlocal coupling was an essential condition for the existence of chimera states and obtaining chimeras in globally and locally coupled networks was considered rare. In this thesis, novel techniques like distance dependent coupling, cross coupling and self coupling in multiple variables are introduced to induce chimera states in the Hindmarsh-Rose neuron network.

The external inputs are found to control synchrony in the network. It finds practical application in the treatment of diseases like Parkinson's or Alzheimer's disease. The distance-dependent coupling induces chimera states and reduces synchrony in globally coupled network. Travelling chimeras are obtained on the modification of initial conditions in locally coupled network. The system with self and mixed electrical coupling synchronises at a lower coupling strength compared to the system with cross coupling. We have obtained chimera states in the network with self coupling in multiple variables. The three coupled differential equations is modified to a set of four coupled equations to include the field effects. The system shows changes in firing patterns under the influence of electromagnetic induction. The chemical self coupling enhances synchrony and also induces chimera states in the network whereas the cross coupling is incapable of inducing synchrony and chimera states. The work is extended to two dimensional lattice topology and the threshold for coupling strength to obtain synchrony is found to be independent of the network size. The influence of cross coupling in the two dimensional lattice is found to induce spatial chimeras.

This work helps in understanding the dynamics and collective behavior of a nonlinear system under the influence of external stimuli, synaptic connections, coupling schemes and different topologies. It provides insight into the functioning and control of these interconnected systems. This research can be relevant for understanding the dynamics of real neural networks.

സാരം

ഈ പ്രബന്ധം ഹിന്ദുമാർഷ്-റോസ് ന്യൂയോണുകളെ ഒരു രേഖീയമല്ലാത്ത ഗണിത മാതൃകയായി അനുമാനിച്ചു കൊണ്ട് ശൃംഖലയിൽ സമന്വയം, അസമന്വയം കിമേറ അവസ്ഥകൾ എന്നിവയെ കുറിച്ചുള്ള സൈദ്ധാന്തിക പഠനം അവതരിപ്പിക്കുന്നു. സിഗ്മൽ ട്രാൻസ്മിഷനിലും മെമ്മറി പ്രോസസ്സിംഗിലും സമന്വയത്തിന്റെ സുപ്രധാന പങ്ക് കാരണം ന്യൂറോണുകളുടെ ശൃംഖലയിൽ സമന്വയം വർദ്ധിപ്പിക്കുന്നതിന് വ്യത്യസ്ത രീതികൾ ഉപയോഗിച്ചിരുന്നു. എന്നിരുന്നാലും, ന്യൂറോണുകൾക്കിടയിലുള്ള അനാവശ്യമായ സമന്വയം നിരവധി രോഗാവസ്ഥകൾക്ക് കാരണമാകുന്നു. മാത്രമല്ല, ശ്രദ്ധയും ധാരണയും പോലുള്ള തലച്ചോറിലെ ചില പ്രവർത്തനങ്ങൾക്ക് അസമന്വയം പ്രധാനമാണെന്ന് കരുതപ്പെടുന്നു. കാരണം ഇത് വ്യത്യസ്ത ന്യൂറൽ പോപ്പുലേഷനുകളെ സ്വതന്ത്രമായി വിവരങ്ങൾ പ്രോസസ്സ് ചെയ്യാൻ അനുവദിക്കുന്നു. സമന്വയം അസമന്വയം മിശ്രിതമായിവരുന്ന അവസ്ഥയെ കിമേറ എന്ന് വിളിക്കുന്നു. കിമേറ അവസ്ഥകളുടെ ഉത്ഭവത്തിനും നിലനിൽപ്പിനും നോൺ ലോക്കൽ സംയോജനം അത്യാവശ്യമാണെന്ന് അനുമാനിക്കപ്പെട്ടു. മാത്രമല്ല ആഗോളതലത്തിലും പ്രാദേശികതലത്തിലും സംയോജിക്കപ്പെട്ട ശൃംഖലയിൽ കിമേറുകൾ ലഭിക്കുന്നത് അപൂർവമായി കണക്കാക്കപ്പെട്ടിരുന്നു. ഈ പ്രബന്ധത്തിൽ, ഹിന്ദുമാർഷ്-റോസ് ന്യൂയോണുകളിൽ ദൂരത്തെ ആശ്രയിച്ചുള്ള സംയോജനം, ക്രോസ് സംയോജനം, ഒന്നിലധികം വേരിയബിളുകളിൽ സ്വയം സംയോജനം തുടങ്ങിയ സാങ്കേതിക വിദ്യകൾ ഉപയോഗിച്ച് കിമേറ അവസ്ഥകൾ ഉണ്ടാക്കാനുള്ള നൂതന മാർഗങ്ങൾ അവതരിപ്പിക്കുന്നു.

ബാഹ്യ ഉത്തേജങ്ങൾ ശൃംഖലയിലെ സമന്വയം നിയന്ത്രിക്കുന്നതായി കണ്ടെത്തി. ഇത് പാർക്കിൻസൺസ് അല്ലെങ്കിൽ അൽഷിമേഴ്സ് പോലുള്ള രോഗങ്ങളുടെ ചികിത്സയിൽ പ്രയോജനപ്രദമാവും. ദൂരത്തെ ആശ്രയിച്ചുള്ള സംയോജനം ആഗോള സംയോജിത ശൃംഖലയിൽ കിമേറ അവസ്ഥകളെ പ്രേരിപ്പിക്കുകയും സമന്വയം കുറയ്ക്കുകയും ചെയ്യുന്നു. പ്രാദേശികമായി സംയോജിച്ച ശൃംഖലയിൽ പ്രാരംഭ വ്യവസ്ഥകളുടെ പരിഷ്കരണം മൂലം പ്രചരിക്കുന്ന കിമേറുകൾ ലഭിച്ചു. സ്വയം, മിക്സഡ് ഇലക്ട്രിക്കൽ സംയോജനമായി താരതമ്യപ്പെടുത്തുമ്പോൾ ക്രോസ് സംയോജനം ഉള്ള സിസ്റ്റത്തിൽ വലിയ സംയോജന ശക്തിയിൽ സമന്വയം ലഭിക്കുന്നു. ഫീൽഡ് ഇഫക്റ്റുകൾ ഉൾപ്പെടുത്തുന്നതിനായി മൂന്ന് ഡിഫറൻഷ്യൽ സമവാക്യങ്ങൾ ഉള്ള മാതൃക നാല് സംയോജിത സമവാക്യങ്ങളായി പരിഷ്കരിച്ചു. ഒന്നിലധികം വേരിയബിളുകളിൽ സ്വയം സംയോജിത ശൃംഖലയിൽ കിമേറ അവസ്ഥകൾ ലഭിച്ചു. വൈദ്യുതകാന്തിക ഇൻഡക്ഷന്റെ സ്വാധീനത്തിൽ ന്യൂറോണുകളുടെ ഫയറിംഗ് പാറ്റേണുകളിൽ മാറ്റങ്ങൾ കാണപ്പെടുന്നു. കെമിക്കൽ സ്വയം സംയോജനം സമന്വയം വർദ്ധിപ്പിക്കുകയും ശൃംഖലയിൽ കിമേറ അവസ്ഥകളെ പ്രേരിപ്പിക്കുകയും ചെയ്യുന്നു. അതേസമയം ക്രോസ് സംയോജനത്തിൽ അവയ്ക്ക് കഴിവില്ല. ഒരു ദ്വിമാന ലാറ്റിസിൽ ക്രമീകരിച്ച ശൃംഖല വിശകലനം ചെയ്യുമ്പോൾ സമന്വയം നേടുന്നതിനുള്ള ശക്തി ശൃംഖലയുടെ വലുപ്പത്തിൽ നിന്ന് സ്വതന്ത്രമാണെന്ന് കണ്ടെത്തി. ദ്വിമാന ലാറ്റിസിലെ ക്രോസ് സംയോജനത്തിന്റെ സ്വാധീനം സ്പേഷ്യൽ കിമേറുകളുടെ ഉത്ഭവം പ്രേരിപ്പിക്കുന്നതായി കണ്ടെത്തി.

ഈ പ്രബന്ധം ബാഹ്യ ഉത്തേജനം, വ്യത്യസ്ത സംയോജന-വിന്യാസ രീതികൾ എന്നിവയുടെ സ്വാധീനത്തിൽ രേഖീയമല്ലാത്ത സിസ്റ്റത്തിന്റെ കൂട്ടായ പെരുമാറ്റം മനസ്സിലാക്കാൻ സഹായിക്കുന്നു. ഇത് പരസ്പരബന്ധിത സംവിധാനങ്ങളുടെ നിയന്ത്രണവും പ്രവർത്തനത്തെക്കുറിച്ചുള്ള ഉൾക്കാഴ്ച നൽകുന്നു. ഈ ഗവേഷണം യഥാർത്ഥ ന്യൂറൽ ശൃംഖലയുടെ ചലനാത്മക മനസ്സിലാക്കാൻ സഹായകരമാകും.

Contents

| | |
|---|--------------|
| List of Figures | xii |
| Preface | xviii |
| 1 Fundamental concepts | 1 |
| 1.1 Introduction | 1 |
| 1.2 Neuron models | 2 |
| 1.3 Hindmarsh-Rose neuron model | 3 |
| 1.4 Memristive HR model | 4 |
| 1.5 Coupling and topology | 5 |
| 1.5.1 Electrical, chemical and field coupling schemes | 5 |
| 1.5.2 Chain, ring and lattice topology | 6 |
| 1.6 Distance-dependent coupling and cross interactions | 7 |
| 1.7 Synchrony and pattern formations | 8 |
| 1.8 Quantifiers | 10 |
| 1.8.1 Statistical factor of synchronisation | 10 |
| 1.8.2 Kuramoto order parameter | 10 |
| 1.8.3 Coefficient of variability | 11 |
| 1.8.4 Transverse Lyapunov exponent | 12 |
| 1.8.5 Strength of incoherence and discontinuity measure | 14 |
| 1.9 Outline of the thesis | 15 |

| | | |
|----------|---|-----------|
| 2 | Linear chain of mean field coupled Hindmarsh-Rose neurons | 17 |
| 2.1 | Introduction | 17 |
| 2.2 | Phase synchrony | 19 |
| 2.2.1 | The bursting phase | 21 |
| 2.2.2 | The coefficient of variability | 23 |
| 2.2.3 | The Kuramoto order parameter | 24 |
| 2.3 | Controlling phase synchrony using external input | 24 |
| 2.3.1 | Intermittent phase synchrony | 25 |
| 2.3.2 | Phase synchronised system | 27 |
| 2.4 | Influence of decaying coupling strength | 30 |
| 2.4.1 | Synchronisation scenario | 32 |
| 2.4.2 | Emergence of chimera states | 33 |
| 2.5 | Results and conclusions | 34 |
| 3 | Chimera states in HR network with ring topology | 36 |
| 3.1 | Introduction | 36 |
| 3.2 | The model and connection architecture | 38 |
| 3.3 | Global interaction | 39 |
| 3.4 | Nonlocal coupling | 43 |
| 3.5 | Nearest neighbour coupling | 46 |
| 3.6 | Results and conclusions | 50 |
| 4 | Synchrony and pattern formations by varying coupling phase | 51 |
| 4.1 | Introduction | 51 |
| 4.2 | In-phase and anti-phase oscillations | 53 |
| 4.2.1 | Synchronisation scenario | 56 |
| 4.2.2 | Stability of synchronisation | 57 |
| 4.3 | Global, nonlocal and local interactions | 62 |
| 4.3.1 | Emergence of chimera, MOS and clusters | 63 |

| | | |
|----------|---|------------|
| 4.3.2 | Strength of incoherence and discontinuity measure | 65 |
| 4.4 | Results and conclusions | 68 |
| 5 | Collective behaviour of magnetically coupled HR network | 70 |
| 5.1 | Introduction | 70 |
| 5.2 | Controlling synchrony using external stimuli | 72 |
| 5.2.1 | Constant external current | 73 |
| 5.2.2 | Time varying external currents | 75 |
| 5.2.3 | Quantifying synchrony | 78 |
| 5.3 | Distance-dependent field couplings | 79 |
| 5.3.1 | Uniform global interaction | 81 |
| 5.3.2 | Emergence of chimera states | 84 |
| 5.4 | Results and conclusions | 88 |
| 6 | Memristive Hindmarsh-Rose neurons with chemical cross coupling | 90 |
| 6.1 | Introduction | 90 |
| 6.2 | Two coupled system | 91 |
| 6.3 | The N coupled system | 99 |
| 6.3.1 | The synchronisation scenario | 101 |
| 6.3.2 | The pattern formations | 101 |
| 6.3.3 | Quantifying chimeras | 105 |
| 6.4 | Results and conclusions | 107 |
| 7 | Memristive Hindmrash-Rose neurons with distance-dependent coupling in 2D lattice | 109 |
| 7.1 | Introduction | 109 |
| 7.2 | HR network in 2D lattice | 110 |
| 7.3 | Synchronisation scenario | 114 |
| 7.3.1 | Coordination number and synchrony | 116 |

| | | |
|----------|---|------------|
| 7.3.2 | Network size and stability of synchrony | 116 |
| 7.4 | Spatiotemporal patterns | 119 |
| 7.5 | Results and conclusions | 124 |
| 8 | Emergence of spatial chimeras in cross coupled network of 2D lattice | 125 |
| 8.1 | Introduction | 125 |
| 8.2 | Chemical cross coupling in 2D lattice | 126 |
| 8.3 | The synchronisation scenario | 128 |
| 8.4 | Emergence of spatial chimeras | 129 |
| 8.5 | Energy aspects | 130 |
| 8.6 | Results and conclusions | 131 |
| 9 | Conclusions and future prospects | 133 |
| 9.1 | Summary | 133 |
| 9.2 | Future prospects | 137 |
| | Bibliography | 138 |

List of Figures

| | | |
|------|---|----|
| 2.1 | Schematic diagram of the coupling strategy in the mean field approach | 20 |
| 2.2 | Inter Spike Interval (ISI) of a single neuron in the excitatory mean field coupled HR network | 21 |
| 2.3 | Time series and bursting phase of a single HR neuron | 22 |
| 2.4 | Average of bursting phase lines neurons with error bars | 23 |
| 2.5 | Variation of the Coefficient of variability with coupling strength | 24 |
| 2.6 | Variation of the averaged Kuramoto order parameter with the coupling strength | 25 |
| 2.7 | Average of bursting phase lines with the error bar of the system with intermittent synchrony and spike input | 25 |
| 2.8 | Variation of the coefficient of variability and the Kuramoto order parameter for mean field coupled HR neurons | 26 |
| 2.9 | Parameter space showing the synchrony pattern for mean field coupled HR neurons with intermittent phase synchrony under the influence of the external spike input | 28 |
| 2.10 | Average of bursting phase lines with the error bar of the system with phase synchrony and spike input | 28 |
| 2.11 | Variation of the coefficient of variability and the Kuramoto order parameter for mean field coupled HR neurons with phase synchrony | 29 |

| | | |
|------|---|----|
| 2.12 | Parameter space showing the synchrony pattern for excitatory mean field coupled HR neurons under the influence of the external spike input | 31 |
| 2.13 | Variation of the statistical factor of synchronisation with coupling constant for different values of decay constant | 32 |
| 2.14 | Emergence of chimera states under the influence of decaying coupling strength | 33 |
| 2.15 | Variation of the strength of incoherence with coupling constant for different values of decay constant | 34 |
| 3.1 | Variation of the statistical factor of synchronisation and synchronisation error with coupling strength for different values of power law exponent | 40 |
| 3.2 | Non-existence of chimera states in the network with global interaction | 41 |
| 3.3 | Emergence of chimera states under the influence of power law exponent in the network with global interaction | 42 |
| 3.4 | Strength of incoherence and discontinuity measure plotted against coupling strength | 43 |
| 3.5 | Variation of the statistical factor of synchronisation and the synchronisation error with the coupling strength in the network with nonlocal interactions, for $\alpha = 0.1$ | 44 |
| 3.6 | Variation of the statistical factor of synchronisation and the synchronisation error with coupling strength in the network with nonlocal interaction, for $\alpha = 0.5$ | 44 |
| 3.7 | Emergence of chimera and multichimera states induced by the interplay of nonlocal coupling and power exponent law | 45 |
| 3.8 | Strength of incoherence and discontinuity measure are plotted against the coupling strength, for $\alpha = 0.1$ | 46 |

| | | |
|------|---|----|
| 3.9 | Strength of incoherence and discontinuity measure are plotted against the coupling strength, for $\alpha = 0.5$ | 47 |
| 3.10 | Variation of the statistical factor of synchronisation and the synchronisation error with the coupling strength for local coupling in mean field coupled HR neurons in ring topology. | 47 |
| 3.11 | Strength of incoherence of mean field coupled HR neurons with local coupling without modifications in initial conditions | 48 |
| 3.12 | Emergence of the chimera states by modified initial conditions in the network with local coupling | 49 |
| 3.13 | Variation of strength of incoherence and discontinuity measure for different values of mean field coupling strength for locally coupled Hindmarsh-Rose neurons with modified initial conditions | 49 |
| 4.1 | Time series of the membrane potential of two coupled HR neurons for different coupling phases | 55 |
| 4.2 | Synchronisation error of two coupled HR neurons with self coupling in the state variables. | 56 |
| 4.3 | Variation of the derivative of Lyapunov function with coupling strengths for different values of coupling phase | 59 |
| 4.4 | Colour coded variation of the time derivative of the Lyapunov function with coupling strength and phase | 61 |
| 4.5 | Variation of the statistical factor of synchronisation with coupling strength in the HR neural network with global interaction for different values of coupling phase | 64 |
| 4.6 | Emergence of interesting patterns in the HR network by the variation of coupling phase in nonlocal and local interactions | 66 |
| 4.7 | Strength of incoherence and discontinuity measure for different coupling phases in nonlocal interactions | 67 |

| | | |
|------|---|----|
| 5.1 | Time series of the discrete and average membrane potentials of the magnetically coupled neural network with constant external current | 74 |
| 5.2 | Phase portraits of the neural network with magnetic coupling and constant external current | 75 |
| 5.3 | Time series of the discrete and average membrane potentials of the magnetically coupled neural network with time varying external stimuli | 76 |
| 5.4 | Phase space with sinusoidal and square input | 77 |
| 5.5 | Variation of the statistical factor of synchronisation with magnetic coupling strength and amplitude of external input, under the influence of external stimuli | 78 |
| 5.6 | Variation of the statistical factor of synchronisation for different parameters of the time varying input | 80 |
| 5.7 | Dynamical changes induced by the interplay of memristor and mean field effects | 82 |
| 5.8 | Spatiotemporal patterns of the HR neurons with memristor and mean field coupling | 83 |
| 5.9 | Variation of the statistical factor of synchronisation of HR neurons with the mean field coupling strength, for different values of memristor coupling strength | 84 |
| 5.10 | Snapshots of the HR neuron network with memristor and mean field effects | 85 |
| 5.11 | Variation of the statistical factor of synchronisation with mean field coupling, for different values of power law exponent | 85 |
| 5.12 | Snapshots of the HR network with distance-dependent memristor and mean field effects | 87 |

| | | |
|------|--|-----|
| 5.13 | Variation of the strength of incoherence and discontinuity measure for different values of the mean field coupling strength | 87 |
| 5.14 | Parameter phase diagram for a network of memristive HR neurons | 88 |
| 6.1 | Time series of two coupled HR neurons, $k_1 = 0.4$ | 92 |
| 6.2 | Time series of two coupled HR neurons, $k_1 = 1.5$ | 93 |
| 6.3 | Time series of two coupled HR neurons, $k_1 = 2.4$ | 94 |
| 6.4 | Variation of the MTLE with coupling strength for different values of coupling phase | 96 |
| 6.5 | Colour coded variation of MTLE for different values of g and δ . . | 98 |
| 6.6 | Variation of the statistical factor of synchronisation with coupling strength for different values of δ | 100 |
| 6.7 | Snapshots of membrane potential under the influence of mixed in- teractions in chemically coupled HR neurons with magnetic coupling | 102 |
| 6.8 | The variation of energies of the neurons in the network | 103 |
| 6.9 | The spatiotemporal patterns of the network | 104 |
| 6.10 | Variation of the strength of incoherence and discontinuity measure with coupling strength for self, mixed and cross couplings | 106 |
| 7.1 | Scheme of coupling between the neurons in the network | 111 |
| 7.2 | Dynamics of HR neuron | 113 |
| 7.3 | Variation of the statistical factor of synchronisation within each 1D array of the 2D lattice network | 114 |
| 7.4 | Variation of the inter array error between the 1D arrays of the 2D lattice network | 115 |
| 7.5 | Variation of the statistical factor of synchronisation with coupling threshold for different coordination number | 115 |

| | | |
|-----|---|-----|
| 7.6 | Variation of statistical factor of synchronisation and maximum transverse Lyapunov exponent with coupling strength for different network size | 117 |
| 7.7 | Spatiotemporal evaluation of membrane potential | 120 |
| 7.8 | Snapshots of the different 1D arrays of the network | 121 |
| 7.9 | Variation of the strength of incoherence and discontinuity measure for different values of coupling strength | 122 |
| 8.1 | Variation of the statistical factor of synchronisation with coupling constant for different values of coupling phase | 128 |
| 8.2 | Snapshots of spatial chimeras | 129 |
| 8.3 | Snapshots of travelling chimeras | 130 |
| 8.4 | Snapshots of Hamilton energy function | 131 |

Preface

Nonlinear systems play a vital role in our modern world ranging from modelling physical phenomena to engineering applications. These systems are complex and challenging to understand, yet essential to various fields. The aim of the present work is to analyse synchronisation behaviour of a network of nonlinear biological oscillators and provide a comprehensive understanding of their behaviour and properties. The results obtained from the study contribute to the development of better methods for the design, control and analysis of these nonlinear systems. The thesis presents the findings of our research in a clear and concise manner and highlights the importance of nonlinear systems in various fields.

Nonlinear systems have widespread applications in various fields, including engineering, robotics, biology, economics, finance, machine learning and environmental studies. They are used to model complex systems and to design controls that ensure stability and performance. Neural networks, which are based on biological neurons, also use nonlinear models to comprehend data and make predictions. The nonlinearity of neuron models allows them to mimic the dynamics of real life neurons.

This thesis presents a theoretical study of the different methods through which a network is driven into synchrony, desynchrony and chimera states. The thesis is organised as follows: **Chapter 1** provides an overview of basic terminologies used in the thesis. In **chapter 2**, the Hindmarsh-Rose (HR) network with mean field coupling is analysed under the influence of external stimuli and an exponentially decaying coupling strength. The stimuli helps to control the synchrony in the network whereas the decaying coupling strength induces chimera

states. In **chapter 3**, the mean field coupling is given a distance dependence governed by power law factor. The synchrony decreases with an increase in the power law factor and chimera states are induced in the network with global, non-local and local interactions. **Chapter 4** analyses the influence of cross coupling of state variables in the electrical mode. In-phase and anti-phase oscillations are induced in the two coupled system under the influence of activator and inhibitor coupling, respectively. In **chapter 5**, the modified HR network which incorporates electromagnetic induction with the help of memristor is analysed under the influence of external stimuli and distance-dependent field couplings. The memristor induces changes in the firing patterns of the neurons. In **chapter 6**, the memristive HR network in ring topology is analysed with chemical cross connections in membrane potential and electromagnetic flux. The self and mixed interactions induces synchrony in the network whereas cross coupling is incapable of it. In **chapter 7**, the memristive HR network is analysed in 2D lattice topology with distance-dependent coupling. The coordination number and network size is varied for the analysis. In **chapter 8**, the study has been extended to a network in 2D lattice with cross coupling and distance-dependent chemical coupling. **Chapter 9** summarises the findings of the thesis and describes future prospects of the work.

Papers

Published/ Accepted/ Communicated

1. **T. Remi**, P. A. Subha, K. Usha, "Controlling phase synchrony in the mean field coupled Hindmarsh–Rose neurons." *International Journal of Modern Physics C*, 33.05 (2022): 2250058.
2. **T. Remi**, P. A. Subha, K. Usha, "Collective dynamics of neural network with distance dependent field coupling." *Communications in Nonlinear Science and Numerical Simulation*, 110 (2022): 106390.
3. **T. Remi**, P. A. Subha, "In-phase and anti-phase bursting dynamics and synchronisation scenario in neural network by varying coupling phase". *Journal of biological physics*, 1-17(2023).
4. **T. Remi**, P. A. Subha, "Memristive Hindmarsh-Rose network in 2D lattice with distance-dependent chemical synapses." *Nonlinear Dynamics* (2023): 1-12.
5. **T. Remi**, P. A. Subha, "Chemically coupled Hindmarsh–Rose neurons with cross interactions between membrane potential and magnetic flux." *Journal of Physics A: Mathematical and Theoretical* 56, no. 34 (2023): 345701.
6. **T. Remi**, P. A. Subha, "Emergence of chimera states in neural networks with distance-dependent mean field coupling". (Under Review)

Conference Presentations

1. **T. Remi**, P. A. Subha, K. Usha, Mean field coupled Hindmarsh-Rose neurons in the presence of external stimuli. International Conference on Theoretical and Experimental Physics (ICTEP), Farook College, February 2020.
2. **T. Remi**, P. A. Subha, Chimera states in neural network with decaying coupling strength. 12th Conference on nonlinear systems and Dynamics (CNSD), Sasthra Deemed University, Thanjavur, December 2021.
3. **T. Remi**, P. A. Subha, The Collective Behavior of Magnetically Coupled Neural Network Under the Influence of External Stimuli. International Conference on Nonlinear Dynamics and Applications (ICNDA), Sikkim Manipal Institute of Technology, March 2022.
Nonlinear Dynamics and Applications: Proceedings of the ICNDA 2022 (pp. 1275-1285). Cham: Springer International Publishing.

Chapter 1

Fundamental concepts

1.1 Introduction

Every process in nature that seems chaotic has a hidden order of action. A wild and unpredictable storm with howling wind and heavy rain may seem like complete chaos and disorder at first glance. But random patterns seem to emerge on closer observation. The electric charge distribution in the case of lightning strikes also follows random patterns. Chaotic characteristics have been proven to exist in wind flow following the principles of fluid dynamics. The raindrops may appear chaotic, but they always follow the laws of gravity and motion. The study that assists in uncovering the underlying order in seemingly chaotic processes, analysing it, controlling it and making predictions is called nonlinear dynamics. Nonlinear systems are found in a wide range of fields including physics, engineering, economics, biology and more [1, 2]. Examples of nonlinear systems include chaotic systems like weather, electronic oscillators, coupled physical oscillators, robot and aircraft. Despite the practical and theoretical challenges that come with the study of nonlinear systems, such as the difficulty in solving nonlinear equations analytically, this field is crucial in our understanding of nature. To overcome these challenges, numerical methods are often utilised to analyse and control nonlinear systems. One of the most significant applications of nonlinear systems is in the field of biological systems, such as studying neurodynamics or

modelling the cardiovascular cycle. In neuroscience, the principles of nonlinearity play a crucial role in understanding the complex behaviour and dynamics of neural networks and how they process information. Some examples of the use of nonlinear systems in neural science include the modeling of neural activity through nonlinear models, the study of synaptic plasticity and learning rules and the analysis of large scale network dynamics. The neuron models are represented by a set of nonlinear differential equations that explain the firing patterns of a single neuron as well as the collective behaviour of a network of neurons.

1.2 Neuron models

Nonlinear models are used to study the individual and collective dynamics of neurons[3, 4]. Neuron models are mathematical representations of the behaviour and properties of neurons. Neurons are specialised cells that transmit signals in the nervous system and ion channels are key to this process. When a neuron receives a signal, it generates an electrical impulse known as action potential. The generation of an action potential involves the movement of ions across the neuron's membrane. At rest, the neuron has a negative charge inside relative to the outside, maintained by a higher concentration of potassium ions inside and a higher concentration of sodium and calcium ions outside. When a stimulus triggers an action potential, sodium channels open and allow sodium ions to flow into the neuron, which depolarises the membrane potential. This depolarisation then causes potassium channels to open, allowing potassium ions to flow out of the neuron, which repolarises the membrane potential and brings it back to its resting state.

Calcium ions are also involved in processes like learning and memory. They can enter the neuron through specialised channels and trigger the release of neurotransmitters, which are chemicals that carry signals between neurons. The neurotransmitters, which get bound to specialised receptor proteins on the receiving neuron, generate a new electrical signal that can either excite or inhibit the neuron in the chain. The electrical signals generated at the synapses are

summed up in the receiving neuron and can either reach the threshold for triggering an action potential or not, depending on the strength of the inputs. This process is repeated across many neurons to transmit signals throughout the nervous system, resulting in the processing of information and the ability to respond to stimuli in the environment [5]. They are used in computational neuroscience to study the function and dynamics of neuronal networks. There are various types of neuron models including Hodgkin-Huxley model [6], FitzHugh-Nagumo model [7], Izhikevich model [8], Hindmarsh-Rose model [9] and Leaky Integrate and Fire model [10], among others. Each model represents different aspects of neuronal behaviour and is used to study different phenomena in brain.

1.3 Hindmarsh-Rose neuron model

The Hindmarsh-Rose (HR) neuron model has several advantages over other models, making it a popular choice in various applications. The HR model is versatile, capable of reproducing multiple types of dynamic behaviours, such as bifurcations, limit cycles and chaos, which makes it suitable for a wide range of scenarios [9]. Its mathematical structure is relatively simple, making it easier to understand and analyse. The HR model also incorporates biologically realistic features, such as slow and fast variables, which accurately describe the behaviour of real neurons [11]. Additionally, the model's ability to capture multiple time scales in the dynamics of a single neuron is another advantage that sets it apart from other models [12]. The HR model has been successfully applied in various fields, such as neuroscience, physics and engineering, demonstrating its predictive power in a variety of contexts [13–16].

The HR model is mathematically expressed as a set of three nonlinear ordinary differential equations, which are functions of the dimensionless dynamical

variables $x(t)$, $y(t)$ and $z(t)$ [9]:

$$\begin{aligned}
 \dot{x} &= y + ax^2 - bx^3 - z + I, \\
 \dot{y} &= c - dx^2 - y, \\
 \dot{z} &= r(s(x - x_e) - z).
 \end{aligned}
 \tag{1.1}$$

The variable x denotes the membrane potential, y denotes the spiking variable and z denotes the bursting variable. The y variable is influenced by the flow of sodium and potassium ions, while the z variable is influenced by the flow of calcium ions. The fast oscillations of x and y correspond to spikes, while the slow oscillations of the z variable cause bursts. The qualitative behaviour of the neurons is controlled by an external current, I [17]. The parameters a, b, c and d are used to represent the behaviour of the fast ion channels. The parameter r is used to model the behaviour of the slow ion channels. The values of the parameters are fixed as: $a = 3, b = 1, c = 1, d = 5, r = 0.006, s = 4$ and $x_e = -1.61$ [18].

1.4 Memristive HR model

The memristor is an electronic component with two terminals that operates passively and it was first proposed by Leon Chua in 1971 [19]. It is a non-volatile device that can remember its resistance state even after power is turned off, making it useful in memory applications. Memristors have been proposed as potential candidates for building next generation computing and memory devices, as they offer several advantages such as high density, low power consumption and fast switching times [20]. At the molecular level, the ionic current crosses the cell membrane, leading to variations in ion concentration and resulting in electromagnetic induction. The effect of alternating electromagnetic fields is depicted by magnetic flux and memristors act as a bridge between the membrane potential and magnetic flux [21, 22]. The transfer of charged ions results in fluctuations of intracellular and extracellular charged ions causing a fluctuating

electromagnetic field. This field modulates the membrane potential of neurons and thus allows communication between neurons even in the absence of synaptic coupling. The modified HR neuron model is given as:

$$\begin{aligned}
 \dot{x} &= y - ax^3 + bx^2 - z + I - k_1\rho(\phi)x, \\
 \dot{y} &= c - dx^2 - y, \\
 \dot{z} &= r(s(x - x_e) - z), \\
 \dot{\phi} &= k_2x - k_3\phi.
 \end{aligned}
 \tag{1.2}$$

ϕ describes the magnetic flux across the membrane, $k_1\rho(\phi)x$ denotes induction current and k_1 is induction coefficient [21, 22]. The term $\rho(\phi)$ is the memory conductance of a magnetic flux controlled memristor. This term describes the coupling between magnetic flux and membrane potential of the neuron. The change in magnetic flux induced by membrane potential is given by k_2x and the leakage of the magnetic flux is represented by $k_3\phi$.

1.5 Coupling and topology

Coupling and topology are important concepts in neural networks, as they have a significant impact on the performance and behaviour of the network. The proper design of coupling and topology can greatly improve the ability of the network to learn and generalise new data. [23]. Coupling refers to the connections between neurons in a network. The strength of these connections determines how much influence one neuron has on another [24].

1.5.1 Electrical, chemical and field coupling schemes

A synapse is a specialised junction that allows communication between neurons or between neurons and other types of cells such as muscles or glands. Electrical synapses are types of synapses that enable direct electrical communication between neurons. They are formed by gap junctions, which are specialised protein channels that create a direct pathway between the cytoplasm of adjacent neu-

rons. Electrical synapses allow rapid and bidirectional transmission of electrical signals between neurons and are found in many regions of the brain and nervous system [25]. A chemical synapse uses neurotransmitters to transmit signals from one neuron to another, or to other types of cells [26]. When an action potential reaches the presynaptic terminal, it triggers the release of neurotransmitters which diffuse across the synaptic cleft and bind to receptors on the post synaptic terminal. Chemical synapses are the most common type of synapse in the nervous system and they are responsible for many important functions, including sensory processing, motor control, learning and memory.

In mean field coupling of neurons, the activity of each neuron is influenced by the average activity of a large population of neurons, rather than by the activity of individual neurons. This approach is often used to model large scale neural networks, where the number of neurons is so large that it is computationally infeasible to simulate the activity of each individual neuron [27]. Electromagnetic field coupling of neurons refers to the influence of electromagnetic induction produced by the change in concentration of ions across the neuron membrane [21, 22]. Electromagnetic fields can affect behaviour of neurons in a variety of ways, including altering their firing rates and synchronising their activity.

1.5.2 Chain, ring and lattice topology

Topology refers to the arrangement of neurons in a network. The networks with more layers or nodes can often learn more complex representations, while networks with fewer layers or nodes may be limited in their representation capacity. The choice of topology should depend on the problem to be solved and the amount of data available for learning. The combination of well designed couplings and topology can allow neural networks to learn and generalise effectively [28]. The choice of topology can have a significant impact on the representational capacity of a neural network and demonstrate how different topologies can lead to different types of representations being learned [29]. Thus, the coupling and topology play a crucial role in the design of neural networks and the proper selection of these elements can greatly impact the performance and behaviour of

the network [30, 31].

As the name suggests, a linear chain topology of neurons refers to a network that is arranged in a linear sequence or chain with the neurons at both ends not connected to each other [32]. If the first and last neurons are connected it forms the ring topology [33]. A network of neurons that are arranged in a regular and repeating pattern form a lattice, resulting in a highly structured and ordered network [34, 35]. In all these topologies, if each neuron is connected only to its closest neighbours, this is known as nearest neighbour or local coupling. On the other hand, if the connections between neurons extend to a fixed number of neurons in their vicinity, this is referred to as nonlocal coupling. Finally, if each neuron is connected to all of the neurons in the network, this is known as global coupling.

1.6 Distance-dependent coupling and cross interactions

The distance-dependent coupling refers to the dependence of the strength of connections on the distance between neurons. The idea is that neurons that are farther apart have weaker connections than those that are close together [36]. This concept has been studied in both theoretical and experimental contexts and has been shown to play a significant role in the functioning of neural networks [37, 38].

Theoretical studies have demonstrated that distance-dependent coupling can help to create more efficient and robust neural networks. It helps to reduce the number of connections needed to achieve a given level of accuracy in a network and increase the stability of the network against external perturbations [39]. Experimental studies have also provided evidence for the importance of distance-dependent coupling in the nervous system. The studies in both invertebrates and vertebrates have shown that the strength of synaptic connections between neurons decreases with increasing distance [40, 41]. Additionally, imaging studies

have shown that the distribution of synapses on dendritic arbors is non-uniform and can be influenced by factors such as the distance between neurons and the presence of intervening barriers [42].

In a neuron model, cross coupling refers to the interaction between different state variables that describe the behaviour of a neuron [43]. A large number of studies have been carried out considering interactions between same variables and ignoring the cross interactions. This cross interaction is important because it helps to capture the complex and dynamic nature of neural behaviour and can provide a more accurate representation of how neurons interact and communicate with each other in the brain [44]. By including cross coupling between these state variables, the model can better reflect the interplay between these different factors and provide a more complete picture of neural behaviour [45].

The cross coupling can help to account for nonlinear and feedback interactions between state variables, which are often important for capturing the complex and dynamic behaviour of neurons [46]. The cross coupled neuron models can provide a better insight into the mechanisms underlying various neural disorders and diseases [44]. The cross coupling is an important aspect of neuron modelling that helps to provide a complete and accurate representation of the behaviour of neurons and the interactions between different factors that shape this behaviour.

1.7 Synchrony and pattern formations

Synchrony in neurons refers to the phenomenon where groups of neurons fire action potentials in a coordinated manner, producing oscillations or waves of activity in the brain. This synchronous activity is thought to play a crucial role in neural coding and information processing in the brain [47]. Neuron models have been successful in explaining various phenomena in neuroscience, including the synchronisation of neurons in the retina, the generation of brain waves in the cortex and the underlying mechanisms of epilepsy [48–50].

Desynchrony in neurons refers to the absence of coordinated firing of action potentials among groups of neurons. Instead, the neurons exhibit more random

and independent patterns of activity. Desynchrony is thought to be important for certain functions in the brain, such as attention and perception [51], because it allows different neural populations to process information independently and in a flexible manner. Research on desynchrony in neurons has implications for understanding various neurological and psychiatric disorders, such as schizophrenia, depression and anxiety [52].

Chimera states are complex spatiotemporal patterns of synchronised and desynchronised behaviour that arise in the networks of coupled neurons. The occurrence of chimera states is closely associated with actual phenomena observed in nature, including unihemispheric slow wave sleep in selected aquatic animals and birds that migrate [53]. The studies have shown that chimera states can emerge from a wide range of initial conditions [54, 55] and can exhibit a rich variety of dynamics, including travelling waves, spiral waves and chaotic behaviour [35, 56–58]. Chimera states have been observed in various experimental settings, such as in brain, chemical reactions and mechanical systems [59–61]. The study of chimera states is an active area of research in nonlinear dynamics and neuroscience, with many open questions and avenues for future exploration.

Multichimera states refer to complex dynamical patterns where some subsets of oscillators synchronise in different ways while other subsets remain desynchronised [62]. These states are characterised by a coexistence of multiple synchronous and asynchronous regions in the network. Multichimera states have been observed in electronic circuits [63] and biological systems, particularly in networks of neurons [64]. In the brain, multichimera states can arise due to the complex interactions between different types of neurons and synapses. It causes a variety of cognitive and behavioural phenomena. The multichimera states have been suggested to play a significant role in epilepsy, where some regions of the brain exhibit synchronous activity while others remain asynchronous. Multichimera states have also been observed in other biological systems, such as populations of cells in microbial colonies or cardiac cells in the heart. Understanding the dynamics of multichimera states in biological systems is an active area of research, with potential implications for the diagnosis and treatment of

various neurological and cardiovascular disorders.

Mixed oscillatory systems exhibit multiple types of oscillatory activities simultaneously, often in the form of a combination of low frequency and high frequency oscillations. These types of neurons have been observed in various brain regions and are thought to play a significant role in information processing and communication between different brain regions. It was first discovered in neural networks when the desynchronised neurons are interspersed among those that are either stationary or oscillate in synchrony [65]. Later, it was also observed in HR neurons under the influence of a controller [66].

Another type of pattern formation exhibited by neurons is clusterisation, where a group of neurons in the network show similar dynamics [66]. These neurons can form functional units in the brain, such as a sensory processing module and are thought to communicate with each other to process information.

1.8 Quantifiers

1.8.1 Statistical factor of synchronisation

The complete synchronisation of coupled oscillators is quantified using various statistical measures. One of the important quantity is statistical factor of synchronisation [22].

$$R = \frac{\langle F^2 \rangle - \langle F \rangle^2}{\frac{1}{N} \sum_{i=1}^N [\langle x_i^2 \rangle - \langle x_i \rangle^2]} \quad (1.3)$$

where $F = \frac{1}{N} \sum_{i=1}^N x_i$ and ' $\langle \rangle$ ' represent the average of the variable over time. x_i is the state variable of the i th oscillator in the network. i runs from 1 to N , N being the total number of oscillators in the network. The value of R ranges from 0 to 1, with higher values indicating stronger synchronisation.

1.8.2 Kuramoto order parameter

Phase synchrony refers to the degree to which the phase of the ongoing oscillations of different neurons become coordinated over time. In other words, it is a

measure of how closely the timing of the oscillations is aligned. While complete synchrony between neurons can be important for certain functions, such as in the synchronisation of heart cells in the heartbeat, in many cases, phase synchrony also has its own relevance. This is because phase synchrony allows for selective and flexible communication between neurons, as the specific timing of spikes in each neuron can carry information about the nature and context of the neural activity.

The Kuramoto order parameter, introduced by Kuramoto, is faithfully used to distinguish between the systems with phase synchrony, intermittent phase synchrony and desynchrony [67]. The order parameter has been calculated using the formula:

$$R(t)e^{i\psi(t)} \equiv \frac{1}{N} \sum_{j=1}^N e^{i\Phi_j(t)}, \quad (1.4)$$

where $R(t)$, ψ represent the magnitude and angle of a centroid phase vector, respectively. Φ_j represents the phase of j th neuron, with $j = 1, 2, \dots, N$.

In a phase synchronised system, the value of R approaches unity and for a desynchronised system, the value is 0. The time averaged Kuramoto order parameter, \bar{R} , has been computed as:

$$\bar{R} = \lim_{T \rightarrow \infty} (1/T) \int_0^T R(t) dt. \quad (1.5)$$

1.8.3 Coefficient of variability

The inter burst intervals (IBI) are an important aspect of neuronal activity that provide valuable information about neuronal firing patterns and communication. The temporal and spatial characteristics of IBI have been distinguished by studying the coefficient of variability (CV). Generally, variability signifies the measure of deviations from a central value. The term CV reveals the variations in the characteristics of IBI collectively [68]. Spatial coefficient of variability, CV_s , represents deviations in the IBIs of k th burst of every neuron, whereas, the temporal coefficient of variability, denoted by CV_t , gives the deviations in IBIs of each neuron, during its time evolution [69]. The low value of deviations in $CV_{s/t}$

shows that the system attains phase synchrony.

The coefficients of variability, CV_s and CV_t are defined as:

$$CV_{s/t} = \frac{\sigma_{s/t}(IBI)}{\langle IBI \rangle} \quad (1.6)$$

where $\sigma(IBI)$ is the standard deviation of the IBIs and $\langle IBI \rangle$ is the time average taken over the IBIs of all neurons.

The spatial and temporal standard deviations are obtained using the formulae:

$$\begin{aligned} \sigma_s &= \frac{1}{k_{max}} \sum_{k=1}^{k_{max}} \sigma(IBI_{k,i}), & \text{where, } i = 1, 2, \dots, N \\ \sigma_t &= \frac{1}{N} \sum_{i=1}^N \sigma(IBI_{k,i}), & \text{where, } k = 1, 2, \dots, k_{max} \end{aligned} \quad (1.7)$$

1.8.4 Transverse Lyapunov exponent

Lyapunov exponents provide a qualitative and quantitative characterisation of dynamical behaviour of a chaotic system. It represents the exponentially fast divergence or convergence of nearby orbits in phase space. If a system has one or more positive Lyapunov exponents, it is considered chaotic, indicating a high level of unpredictability. This concept has been applied to analyse the dynamics of various systems [70].

The transverse Lyapunov exponent (TLE), in turn is a measure of the rate of divergence of nearby trajectories in a dynamic system, in directions perpendicular to the direction of motion [71]. It provides an idea about the condition at which the coupled system is synchronised [72]. The maximum transverse Lyapunov exponent (MTLE) is used as the bifurcation parameter to get the point of transition to synchrony. The MTLE becomes negative when system is synchronised.

The fundamental approach for determining TLE of any coupled system remains the same [73–75]. Let N identical coupled oscillators be represented by

the dynamical equations of the form:

$$\begin{aligned}
\frac{dx^1}{dt} &= F^1(x^1, x^2, \dots, x^N) + cG(x^1, x^2, \dots, x^N), \\
\frac{dx^2}{dt} &= F^2(x^1, x^2, \dots, x^N) + cG(x^1, x^2, \dots, x^N), \\
&\vdots \\
\frac{dx^N}{dt} &= F^N(x^1, x^2, \dots, x^N) + cG(x^1, x^2, \dots, x^N),
\end{aligned} \tag{1.8}$$

Here, the x^i are oscillator coordinates such that $(x_1^i, x_2^i, \dots, x_n^i) \in R^n$ and $F: R^n \rightarrow R^n$ is the nonlinear vector field controlling the dynamics of a single oscillator. The function $G^i: R^m \rightarrow R^n$, where $m = nM$, describe the coupling of the i th oscillator to all other oscillators and c is a scalar coupling constant.

The geometry of the synchronous attractor is such that it lies on a hyperplane determined by the $n - 1$ vector equalities

$$(x_1^1, x_1^2, \dots, x_1^N) = (x_2^1, x_2^2, \dots, x_2^N) = \dots = (x_n^1, x_n^2, \dots, x_n^N) \tag{1.9}$$

The hyperplane is called the synchronisation manifold and has dimension N . As long as the entire system's phase space point remains on the synchronisation manifold the systems remain in synchrony. Thus all the motions that are transverse to the synchronisation manifold should be damped out. For this, the Jacobian matrix has been formed which has the following structure:

$$\left(\begin{array}{cccccc}
\mathbf{J}_1 + \mathbf{G}\gamma_{1,1} & \mathbf{G}\gamma_{1,2} & \mathbf{G}\gamma_{1,3} & \mathbf{G}\gamma_{1,4} & \cdots & \mathbf{G}\gamma_{1,n} \\
\mathbf{G}\gamma_{2,1} & \mathbf{J}_2 + \mathbf{G}\gamma_{2,2} & \mathbf{G}\gamma_{2,3} & \mathbf{G}\gamma_{2,4} & \cdots & \mathbf{G}\gamma_{2,n} \\
\mathbf{G}\gamma_{3,1} & \mathbf{G}\gamma_{3,2} & \mathbf{J}_3 + \mathbf{G}\gamma_{3,3} & \mathbf{G}\gamma_{3,4} & \cdots & \mathbf{G}\gamma_{3,n} \\
\vdots & \vdots & \vdots & \vdots & \cdots & \vdots \\
\mathbf{G}\gamma_{n,1} & \mathbf{G}\gamma_{n,2} & \mathbf{G}\gamma_{n,3} & \mathbf{G}\gamma_{n,4} & \vdots & \mathbf{J}_n + \mathbf{G}\gamma_{n,n}
\end{array} \right) \tag{1.10}$$

Where,

$$\mathbf{J}_i = \begin{pmatrix} \frac{\partial F^1}{\partial x_i^1} & \frac{\partial F^1}{\partial x_i^2} & \frac{\partial F^1}{\partial x_i^3} & \frac{\partial F^1}{\partial x_i^4} & \cdots & \frac{\partial F^1}{\partial x_i^N} \\ \frac{\partial F^2}{\partial x_i^1} & \frac{\partial F^2}{\partial x_i^2} & \frac{\partial F^2}{\partial x_i^3} & \frac{\partial F^2}{\partial x_i^4} & \cdots & \frac{\partial F^2}{\partial x_i^N} \\ \frac{\partial F^3}{\partial x_i^1} & \frac{\partial F^3}{\partial x_i^2} & \frac{\partial F^3}{\partial x_i^3} & \frac{\partial F^3}{\partial x_i^4} & \cdots & \frac{\partial F^3}{\partial x_i^N} \\ \vdots & \vdots & \vdots & \vdots & \cdots & \vdots \\ \frac{\partial F^N}{\partial x_i^1} & \frac{\partial F^N}{\partial x_i^2} & \frac{\partial F^N}{\partial x_i^3} & \frac{\partial F^N}{\partial x_i^4} & \cdots & \frac{\partial F^N}{\partial x_i^N} \end{pmatrix} \quad (1.11)$$

The terms $\gamma_{i,i}$ and $\gamma_{i,j}$ is obtained by partially differentiating the coupling term with respect to f_i^N and f_j^N , respectively, f being the state variable. The Jacobian given by eqn. 1.10 is diagonalised in a coordinate system that isolates the stability of the synchronisation manifold from the transverse directions. The system attains stabilised synchrony when MTLE becomes negative.

1.8.5 Strength of incoherence and discontinuity measure

The strength of incoherence is a term used to verify the occurrence of chimera states. For this purpose, the local standard deviation, $\sigma(m)$, has been evaluated from the time series. The total number of oscillators, N , is split into ‘M’ bins of equal length ‘ n' ’ = N/M and the difference dynamical variable $\omega_j = x_j - x_{j+1}$ has been obtained. Then the local standard deviation is defined as [76]:

$$\sigma(m) = \left\langle \sqrt{\frac{1}{n'} \sum_{j=n'(m-1)+1}^{mn'} [\omega_j - \langle \omega \rangle]^2} \right\rangle_t, \quad (1.12)$$

where, $m = 1, 2, \dots, M$; $\langle \omega \rangle = \frac{1}{N} \sum_{i=1}^N \omega_i(t)$. $\langle \dots \rangle_t$ denotes the average over time. The term SI is defined as:

$$SI = 1 - \frac{\sum_{m=1}^M s_m}{M}, \quad s_m = \mathcal{H}(\epsilon - \sigma(m)). \quad (1.13)$$

Here, \mathcal{H} is the Heaviside step function and ϵ is a predefined threshold. The values of SI are 1, 0 or between 1 and 0, representing incoherent, coherent and chimera or multichimera states, respectively. In order to distinguish chimera from multichimera states, discontinuity measure (DM) is calculated [76], which is defined as:

$$DM = \frac{\sum_{i=1}^M |s_{i+1} - s_i|}{2}, \quad (1.14)$$

where, $s_{M+1} = s_1$. For chimera, $DM = 1$ and for multichimera $2 \leq DM \leq \frac{M}{2}$.

1.9 Outline of the thesis

This thesis presents the studies on the synchronisation and the emergence of chimera states in HR networks under the influence of external inputs, distance-dependent coupling and cross interactions between the state variables. The thesis is organised as follows: chapters 2, 3 and 4 analyse the HR network in linear and ring topologies under the influence of external stimuli, as well as distance-dependent and cross interactions. The HR network is then modified to incorporate electromagnetic induction effects and its behaviour in the presence of external inputs, distance-dependent coupling and cross coupling schemes are analysed, which is presented in chapters 5 and 6. The study has been extended to network with higher dimension and network size and is presented in chapters 7 and 8. Chapter 9 summarises the results of the thesis.

In chapter 2, the influence of spike input is analysed in HR network arranged in linear chain topology with uniform mean field coupling. Mean field coupling in the network is highly relevant because the neurons behave collectively. The HR networks are also analysed under the influence of exponentially decaying coupling strength. The synchrony is controlled by the external input, while decaying coupling strength induces chimera states. In chapter 3, the HR network is analysed in ring topology with global, nonlocal and local interactions. The contribution from the neighbouring neurons is given a distance dependence by taking the ratio of coupling strength to the distance between neurons. But the decrease in the contribution is very steep. To avoid this, power law exponent is introduced which produces a slower decrease in contribution from neurons as the distance between them increases. In chapter 4, the HR neural network is analysed with cross coupling between state variables in electrical mode. The cross interactions are modelled using a rotation matrix, through which the self, mixed

and cross interactions are realised by varying coupling phase. Electrical coupling involves the connection of neurons through a gap junction and is mathematically represented using a linear equation.

In chapter 5, the memristive network of HR neurons is analysed under the influence of external time varying inputs in linear chain topology. The network is further analysed under the combined effects of distance-dependent memristors and mean field coupling. In chapter 6, the chemical cross interactions of state variables are analysed in memristive HR neural neural network in ring topology. In chemical coupling, the propagation of information occurs through the release and diffusion of a chemical known as neurotransmitter, which is expressed using a nonlinear equation.

In chapter 7, the memristive HR neurons are analysed in a 2D lattice topology, with distance-dependent chemical coupling governed by power law exponent. The lattice arrangement of neurons is a useful tool for modelling spatial relationships between neurons which helps to understand the underlying structure of neural networks. Chapter 8 analyses the cross coupling of state variables in a 2D lattice with distance-dependent chemical coupling. The network exhibits spatial chimeras, which are observed in networks with both regular and random connectivity.

Chapter 9 summarises the main findings of the thesis and presents potential future directions for further research in the current work.

Chapter 2

Linear chain of mean field coupled Hindmarsh-Rose neurons

2.1 Introduction

The basic principle behind memory and signal transmission in humans is synchronised oscillations in the brain. The human brain has approximately 10^{11} neurons. The collective behaviour of neuronal synapses can be effectively expressed through mean field coupling [77, 78], which is an all to all coupling that has been studied in various systems such as FitzHugh-Nagumo and Hodgkin-Huxley neurons [79, 80]. The existence and stability of localised solutions in a network of quadratic integrate and fire neurons with a mean field coupling have been analysed [81]. A large number of coordinated neurons, which is typical in mean field models [82, 83], exhibit a Kuramoto self synchronisation transition with sufficient coupling strength [84, 85].

However, synchronisation is not always desirable. There have been various methods developed to suppress synchronisation in oscillatory networks with [27] and without feedback [86]. Neuron models can respond to different external stimuli by altering bursting modes and neuronal activities [87, 88]. An effective technique for controlling synchrony in a globally coupled ensemble using precisely timed pulses has been reported [89, 90]. The dependence of pathological

conditions such as epilepsy, Parkinson's disease (PD) and schizophrenia on the unwanted synchronisation of independent nuclei has been demonstrated both experimentally [91, 92] and theoretically [93, 94]. This pathological synchronisation is modelled using mean field coupling [27, 95]. Externally applied electrical impulses could partially or completely control the collective behaviour of neurons, which forms the theoretical foundation for the surgical technique known as Deep Brain Stimulation (DBS). This has been studied successfully using the Hodgkin-Huxley neuron model [96, 97]. It is hypothesised that abnormal synchronisation of independent neurons causes PD and that DBS suppresses the tremors of PD by desynchronising neurons [98]. The high desynchronising ability of high frequency spikes with optimal amplitude and pulse width in DBS has been proven clinically [99]. The automated adaptation of DBS treatment to the fluctuations in disease symptoms is highly valued [100].

This chapter analyses the phase synchrony and its control by an external input, in a network of mean field coupled HR neurons. The influence of the coupling strength, which exponentially decays with distance, is also analysed. The chapter is organised as follows: The mean field coupled model is described in section 2.2. Section 2.2.1 studies the phase synchrony in the network using bursting phase. The synchronisation pattern is analysed using the coefficient of variability and the Kuramoto order parameter in section 2.2.2 and 2.2.3, respectively. The capability of spike input, in controlling phase synchrony, in the excitatory mean field coupled HR neurons is presented in section 2.3. The system with intermittent phase synchrony under the influence of the external input is presented in section 2.3.1. The effect of the input on the well synchronised system is presented in section 2.3.2. The system with coupling strength that decays with distance is analysed in section 2.4. The synchronisation scenario and the emergence of chimeras are analysed in sections 2.4.1 and 2.4.2, respectively. Section 2.5 presents the results of the chapter.

2.2 Phase synchrony

The mean field coupling assumes that each neuron is globally (all to all) coupled to other neurons, which is typical for a neural population [101].

The modified HR model with spike input has the form:

$$\begin{aligned} \dot{x}_i &= y_i + ax_i^2 - bx_i^3 - z_i + I + gI_i^{mf} + I^{sp}, \\ \dot{y}_i &= c - dx_i^2 - y_i, \\ \dot{z}_i &= r(s(x_i - x_e) - z_i), \quad i = 1, 2, \dots, N. \end{aligned} \quad (2.1)$$

x_i , y_i and z_i represent the membrane potential, spiking variable and bursting variable of i th neuron, respectively. y_i is constituted by the flow of Na^+ and K^+ ions and the flow of Ca^+ ions constitute the z_i term. The fast oscillations of x_i and y_i correspond to spikes, whereas, the slow oscillations of the z_i variable cause burst. The external current, I , controls the qualitative behaviour of the neurons [17].

In a network of mean field coupled neurons, each neuron is driven by the force, gI_i^{mf} [27]. g is the coupling strength and I_i^{mf} is the mean field term. It represents the average of contributions from the membrane potentials of all neurons and is directly proportional to the synaptic current which is given as:

$$I_i^{mf}(t) = \frac{1}{N-1} \sum_{\substack{j=1 \\ j \neq i}}^N \epsilon_{ij} x_j(t). \quad (2.2)$$

Indices i and j denote the postsynaptic and presynaptic neuron, respectively. N is the total number of neurons. x_j is the membrane potential of the j th neuron. In mean field approach, the potential, x_i , is influenced by the average of potentials, x_j , where, $j = 1, 2, 3, \dots, N; j \neq i$. The matrix element, ϵ_{ij} , can take values, 0, 1 or -1 , if the presynaptic neuron j is disconnected, excitatory or inhibitory, respectively, with respect to postsynaptic neuron, i . Fig. 2.1 shows the mean field coupling topology in which the first neuron is coupled to the mean potential of neurons 2 to N .

The term I^{sp} represents the external input [96], which has the form:

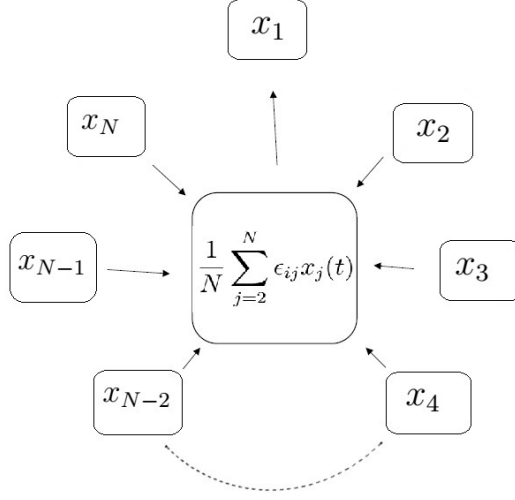


Figure 2.1: Schematic diagram of the coupling strategy in the mean field approach. The combined effect of potentials of neurons, from 2 to N, influences the potential of the first neuron. The value of ϵ_{ij} decides the nature of coupling *viz.* disconnected, excitatory or inhibitory.

$$I^{sp} = AH \left(\sin \left(\frac{2\pi t}{\rho} \right) \right) \left(1 - \mathcal{H} \left(\sin \left(\frac{2\pi t + D}{\rho} \right) \right) \right), \quad (2.3)$$

where A , ρ and D represent the amplitude, interval and pulse width of spike input, respectively. \mathcal{H} is the bi-valued Heaviside step function, whose value is zero for negative arguments and one for positive arguments.

The variation of ISI with increasing g have been studied for a single neuron in a mean field coupled HR network, given by Eq. (2.1), with $I^{sp} = 0$. The parameters of the network are fixed as $a = 3.0$, $b = 1.0$, $c = 1$, $d = 5$, $r = 0.006$, $s = 4.0$ and $x_e = -1.61$ [18]. The initial conditions are chosen randomly between 0 and 1 and the external current, I , is taken as 3.1. The study shows that the inhibitory mode has no influence on individual neuron dynamics, whereas the excitatory mode induces dynamical change in each neuron under coupling. The $ISI-g$ diagram of a single neuron in an excitatory mean field coupled network is shown in fig. 2.2. The scattered points near $g = 0$ represent the irregular bursting dynamics of the system. With an increase in value upto $g \approx 0.2$, regular bursting character is observed, which is visible as the clustering of points

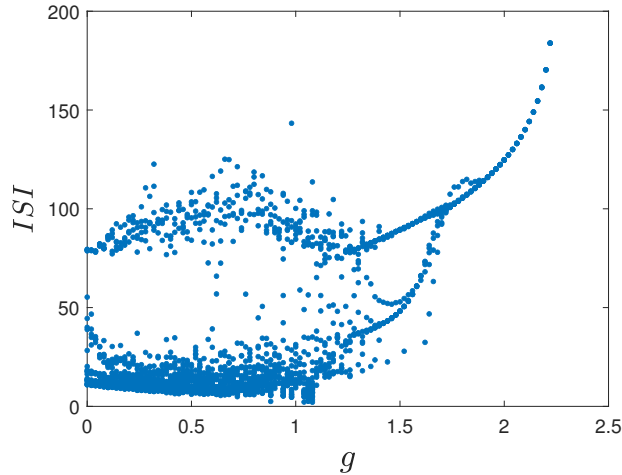


Figure 2.2: Inter Spike Interval (ISI) of a single neuron in the excitatory mean field coupled HR network with $N = 100$. The behaviour represented for single neuron is consistent for every neuron in the network.

into two categories. The region, from $g \approx 0.2$ to $g \approx 1.2$, shows spreading of points, which represents the irregularity induced in bursting. The accumulation of points, from $g \approx 1.2$ to 1.7 , into two sections substantiates the dynamical change to regular bursting, with two spikes per burst. For $g > 1.7$, the character of the system is changed to tonic spiking represented by single bifurcation line. Above the value $g = 2.2$, the system rests to a stable state and no oscillations are produced. So, the studies are focused to the excitatory mean field network, with $0 \lesssim g < 0.2$, for which the system shows regular bursting.

2.2.1 The bursting phase

The bursting dynamics of HR neurons are periodic in nature and this periodicity is used to calculate the bursting phase of the neurons [102]. The bursting phase description is made simple by considering that, a burst begins at phase, $\Phi = 0$ and evolves until $\Phi = 2\pi$. The points in between evolve as:

$$\Phi_i(t) = 2\pi k_i + 2\pi \frac{t - t_{k,i}}{t_{k+1,i} - t_{k,i}}, \quad (t_k < t < t_{k+1}), \quad (2.4)$$

where $t_{k,i}$ is the time at which the k th burst of the i th neuron gets initiated. Fig. 2.3(a) depicts time series of variables x (blue) and z (red). It is evident

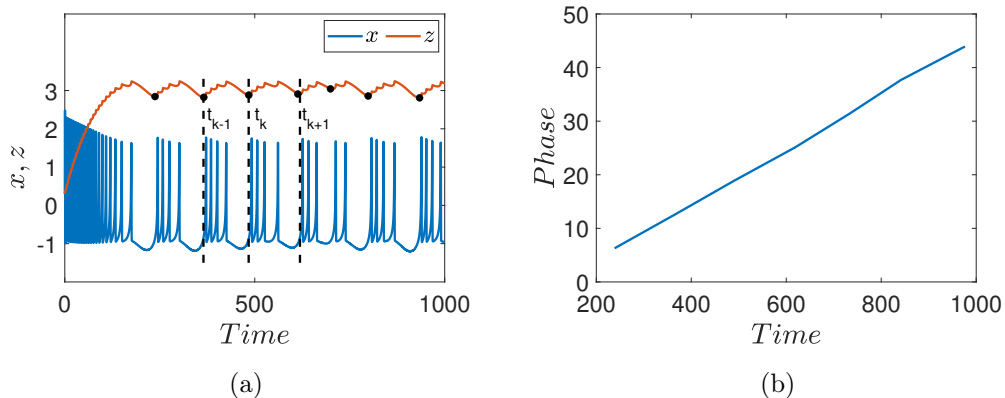


Figure 2.3: Time series and bursting phase of a single HR neuron. (a) Time series of single HR neuron, exhibiting regular bursting. The blue and red lines represent x and z variable, respectively. The black dashed lines corresponds to the beginning of three consecutive bursts, represented as t_{k-1} , t_k , t_{k+1} . (b) Bursting phase, Φ , of the system.

from fig. 2.3(a) that the minima of the z variable coincides temporally with the beginning of each burst in x variable, as shown by the black dashed lines. The bursting phase of a single system has been calculated using Eq. (2.4) and is shown in fig. 2.3(b). The linearly increasing phase proves the regularity in Inter Burst Intervals (IBIs). The slight change in IBI is evident in the bending of the phase line after $t \approx 800$.

The phase synchronisation in the network of mean field coupled HR neurons, given by Eq. (2.1), with $I^{sp} = 0$, has been studied numerically using the bursting phase. The analysis has been carried out for three coupling schemes, *viz.*, disconnected, excitatory and inhibitory, by assigning values 0, +1 and -1, for ϵ_{ij} , respectively, in Eq. (2.1). The bursting phase lines of neurons with these coupling schemes are shown in fig. 2.4.

The bursting phase lines of disconnected, excitatory and inhibitory neurons are presented in fig. 2.4. The average phases of 20 neurons with error bars are plotted in the figure. The error bar signifies the separation of each phase line from the average. The low value of error bar depicts the phase synchrony in the system with excitatory coupling, whereas the high error bar values of disconnected and inhibitory connected neurons represent the desynchrony in the system. From the studies, it is found that complete phase synchrony is observed

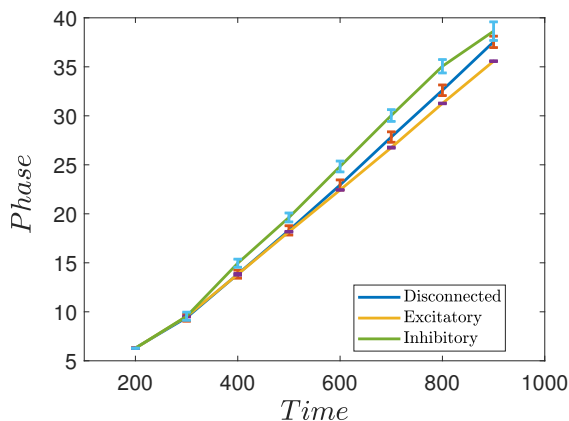


Figure 2.4: Average of bursting phase lines of $N = 20$ neurons, with error bars, in disconnected ($\epsilon_{ij} = 0$, $g = 0$), excitatory ($\epsilon_{ij} = +1$, $g = 0.2$) and inhibitory ($\epsilon_{ij} = -1$, $g = 0.2$) connections.

in the excitatory mean field network. The synchronisation behaviour has been analysed using the coefficient of variability and the Kuramoto order parameter.

2.2.2 The coefficient of variability

The temporal and spatial characteristics of IBI have been distinguished by studying the coefficient of variability (CV). Generally, variability signifies the measure of deviations from a central value. The term CV reveals the variations in the characteristics of IBI collectively [68]. The spatial coefficient of variability, CV_s , represents deviations in the IBIs of k th burst of every neuron, whereas the temporal coefficient of variability, CV_t , gives the deviations in IBIs of each neuron during its time evolution [69]. The low value of deviations in $CV_{s/t}$ shows that the system attains phase synchrony.

The coefficients of variability, CV_s and CV_t , are calculated using the formulae given in Eq. (1.6)

The variation of CV_t (blue) and CV_s (red) with increasing g are presented in fig. 2.5. The high values of $CV_{s/t}$ at $g = 0$ specify the deviations in the firing times of neurons in an uncoupled system. As g increases, $CV_{s/t}$ decreases, which implies that neurons possess same firing times. For values, $0 < g \lesssim 0.1$, the value of CV_t is small compared to CV_s , signifying that regularity in bursting across neurons trails behind the regularity of bursting in each neuron. When $g > 0.1$,

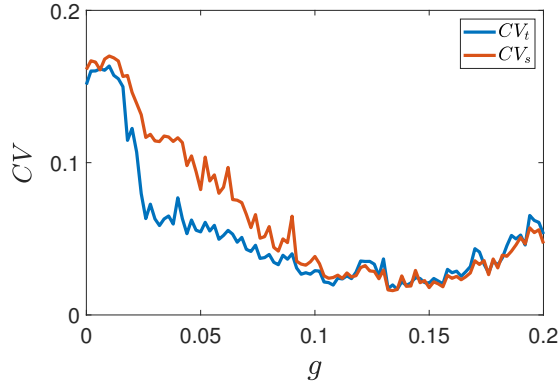


Figure 2.5: Variation of the $CV_{s/t}$ with coupling strength (g), plotted on the Y-axis and X-axis, respectively.

$CV_{s/t}$ become low, representing that the system has attained phase synchrony.

2.2.3 The Kuramoto order parameter

The Kuramoto order parameter is calculated using the Eq. (1.4). The variation of averaged Kuramoto order parameter, \bar{R} , with coupling strength, g , of an excitatory mean field coupled system represented by Eq. (2.1), with $N = 100$ and $I^{sp} = 0$, have been studied, using the formula given in Eq. (1.5). As shown in fig. 2.6, \bar{R} increases as g increases. The system attains an intermittent phase synchrony, $\bar{R} = 0.52$, at $g = 0.022$ and a well synchronised state with $\bar{R} = 0.94$, at $g = 0.15$ [103].

2.3 Controlling phase synchrony using external input

The effects of spike input on the excitatory mean field coupled system with phase synchrony have been analysed in this section. The bursting phase, coefficient of variability and Kuramoto order parameter have been studied by varying the amplitude, A , pulse width, D and interval, ρ , of the input.

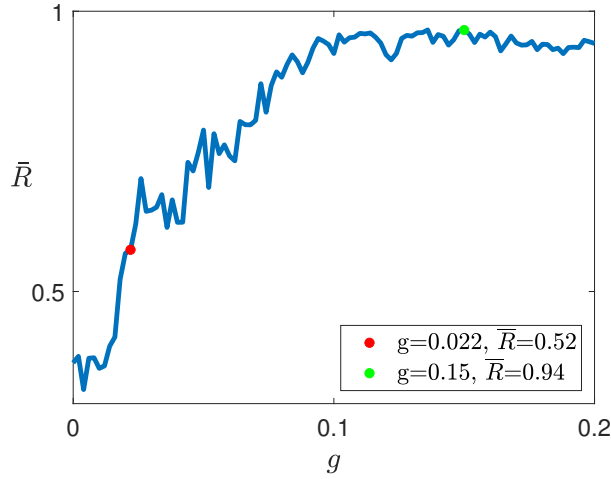


Figure 2.6: Variation of the averaged Kuramoto order parameter (\bar{R}) with the increase in coupling strength (g), plotted on the Y-axis and X-axis, respectively. $\bar{R} \approx 1$ and $\bar{R} \approx 0$ denotes synchrony and desynchrony, respectively. The value of g corresponding to the intermittent synchrony, $\bar{R} = 0.52$, is displayed along with the well synchronised system with $\bar{R} = 0.94$.

2.3.1 Intermittent phase synchrony

The influence of spike input on an excitatory mean field coupled system with intermittent phase synchrony has been analysed by studying the phase of bursts, coefficient of variability and Kuramoto order parameter.

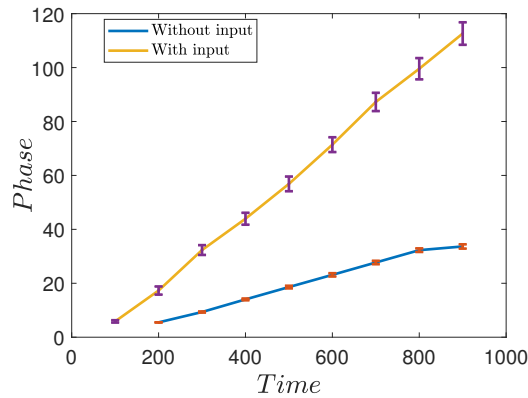


Figure 2.7: Average of bursting phase lines of $N = 20$ neurons with the error bar, in excitatory mean field coupled HR neurons with intermittent phase synchrony ($g = 0.022$), under the influence of spike input ($A = 3$, $D = 0.6$, $\rho = 3$).

The intermittent phase synchrony at $g = 0.022$ and the control of synchrony by the external stimulus are shown in fig. 2.7. The low value of the error bar

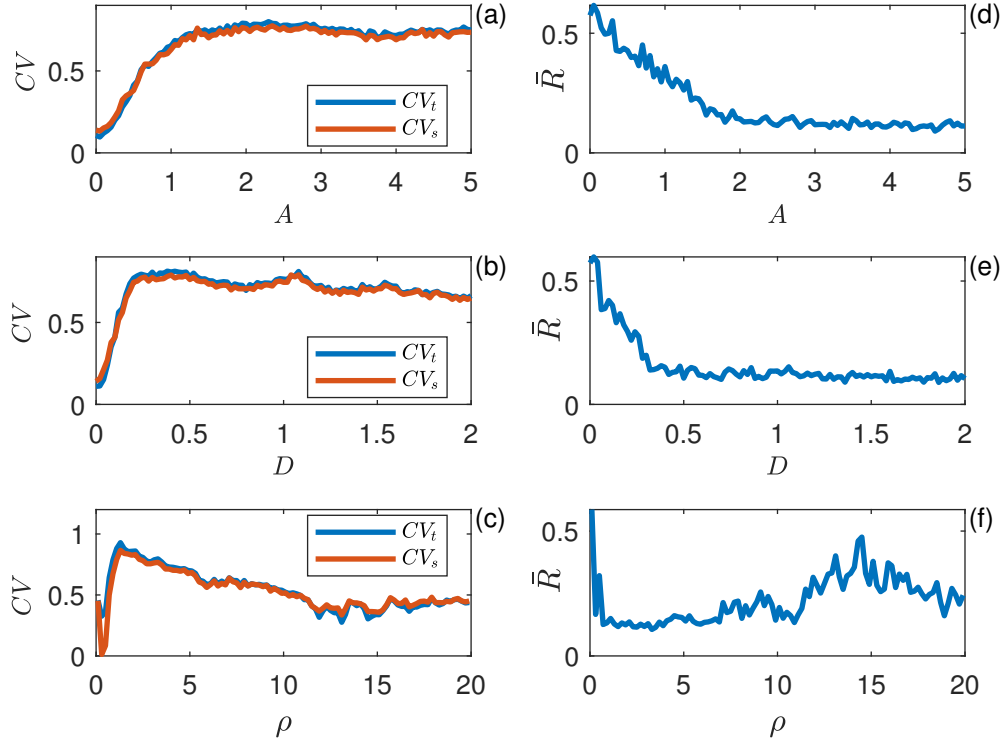


Figure 2.8: Variation of the coefficient of variability ($CV_{s/t}$) and the Kuramoto order parameter (\bar{R}) for mean field coupled HR neurons with intermittent phase synchrony ($N = 100$, $g = 0.022$, $\epsilon_{ij} = +1$) under the influence of spike input. Figures on the left panel represent variation of $CV_{s/t}$. (a) $D = 0.6$, $\rho = 3$, (b) $A = 3$, $\rho = 3$, (c) $A = 3$, $D = 0.6$. Figures in the right panel represent the variation of \bar{R} . (d) $D = 0.6$, $\rho = 3$, (e) $A = 3$, $\rho = 3$, (f) $A = 3$, $D = 0.6$.

in the system without input represents the similarities in burst phase lines. The suppression of intermittent phase synchrony under the influence of spike input is visible from the high valued error bars. The increase in the average value of phases in the presence of external stimuli is due to the additional bursts introduced by the input.

The variation of $CV_{s/t}$ with amplitude of the input is shown in fig. 2.8(a). When $A = 0$, the system shows intermittent phase synchrony. As A increases, $CV_{s/t}$ increases, which shows the capability of the input to desynchronise and cause changes in the firing times of each neuron. At higher values of A , the term $CV_{s/t}$ remains constant, showing its desynchronising ability. The correspondence between values of $CV_{s/t}$ implies that an excitatory mean field coupled system

loses synchrony in the temporal and spatial characteristics of IBIs, identically, in the presence of the input. The variation of $CV_{s/t}$ with respect to change in pulse width of the input are shown in fig. 2.8(b). The variation of $CV_{s/t}$ shows that greater desynchronising ability is visible for values, $D > 0.3$. The variation in $CV_{s/t}$ with the interval of the input is shown in fig. 2.8(c). The $CV_{s/t}$ shows a high value, signifying phase desynchrony and irregularities in bursts, for low ρ values (*i.e.*, high frequency).

The capability of the spike input to desynchronise the mean field coupled system is quantified by studying the variation of \bar{R} with A , D and ρ . The variation of \bar{R} with the change in parameter, A , is shown in fig. 2.8(d). The capability of high frequency input to suppress the synchrony is found to be at $A > 3$, compared to the low amplitudes. The variation of \bar{R} , with change in D is as shown in fig. 2.8(e). The control of synchrony is higher at values of $D > 0.3$. The change in desynchronising ability of the input with change in interval is presented in fig. 2.8(f). Input with low interval, *i.e.*, high frequency, is found to have higher desynchronising ability. From the above studies, it is clear that a spike input with high amplitude, high pulse width and low interval has greater ability to desynchronise the coupled system and the variation of $CV_{s/t}$ is found to be opposite to those of \bar{R} .

The parameter space diagram A - ρ , presented in fig. 2.9, reveals the richer dynamics of the excitatory mean field coupled system with intermittent phase synchrony in the presence of input. Input with high interval (low frequency) is found to have less desynchronising capability. A high number of blue points, signifying desynchrony, is visible for inputs with high amplitude and low interval (high frequency).

2.3.2 Phase synchronised system

The study is extended to the analysis of the influence of spike input on an excitatory mean field coupled system, represented by Eq. (2.1), exhibiting phase synchrony, at $g = 0.15$.

The phase synchrony, at $g = 0.15$ and its control by the external stimulus

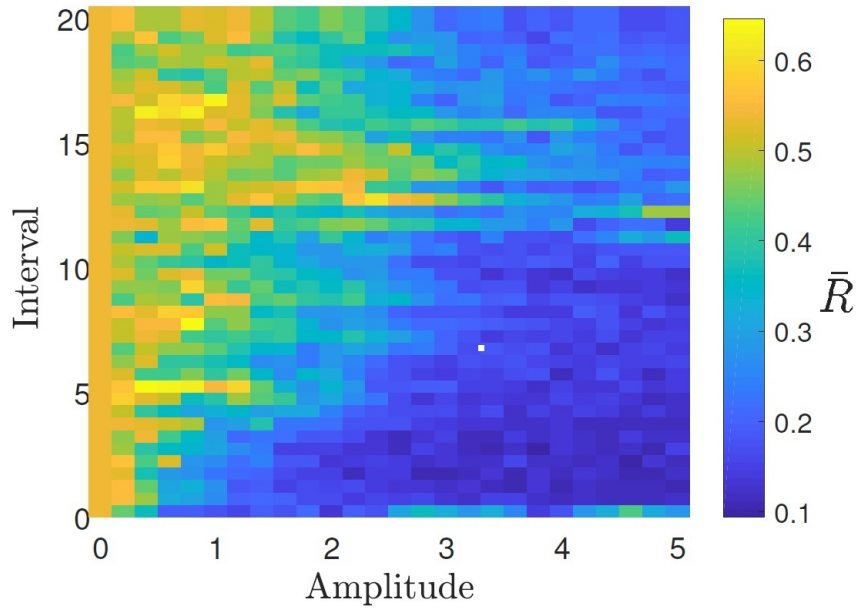


Figure 2.9: Parameter space showing the synchrony pattern for mean field coupled HR neurons with intermittent phase synchrony under the influence of the external spike input. A is plotted along X-axis and ρ along Y-axis. Here, $D = 0.6$ and $g = 0.022$. Yellow and blue colours represent synchrony and desynchrony, respectively.

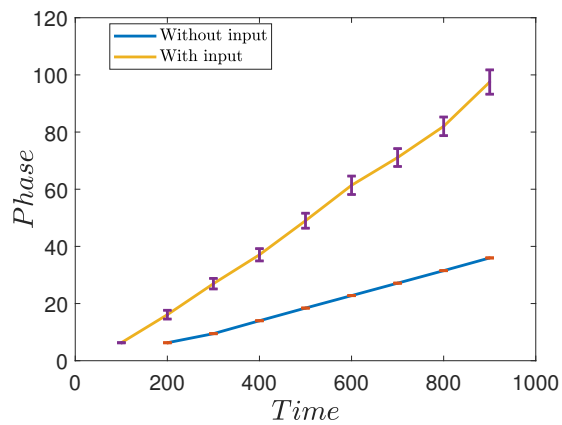


Figure 2.10: Average of bursting phase lines of $N = 20$ neurons, with the error bars in excitatory mean field system with phase synchrony ($g = 0.15$), under the influence of spike input ($A = 3$, $D = 0.6$, $\rho = 3$).

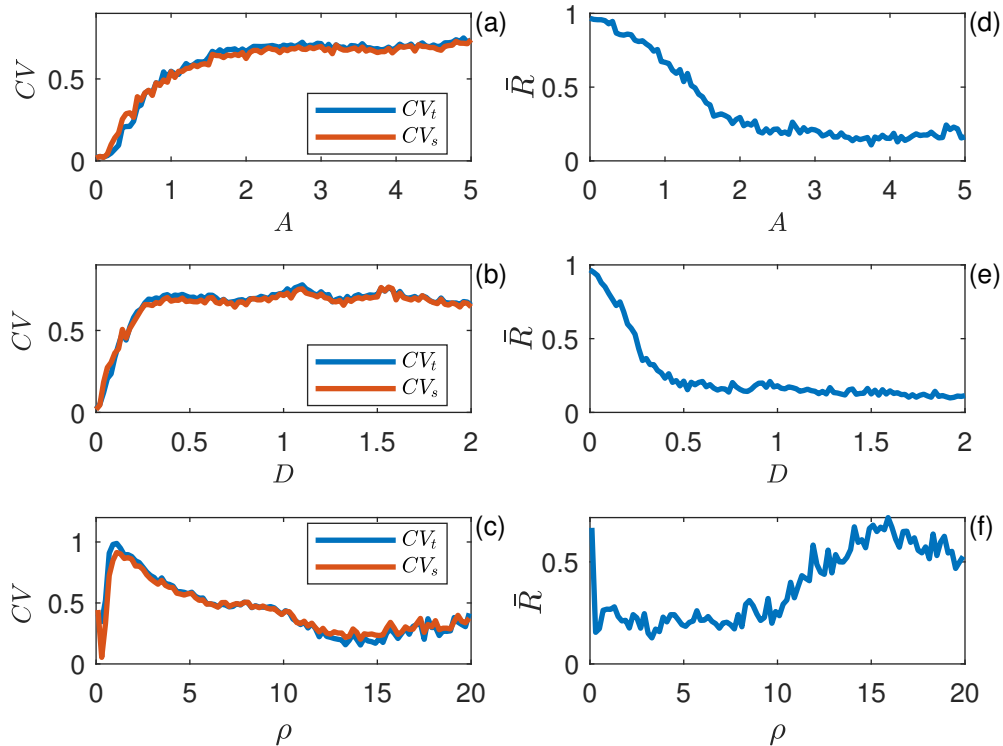


Figure 2.11: Variation of the coefficient of variability ($CV_{s/t}$) and the Kuramoto order parameter (\bar{R}) for mean field coupled HR neurons with phase synchrony ($N = 100$, $g = 0.15$, $\epsilon_{ij} = +1$) under the influence of spike input. Figures on the left panel represent variation of $CV_{s/t}$. (a) $D = 0.6$, $\rho = 3$, (b) $A = 3$, $\rho = 3$, (c) $A = 3$, $D = 0.6$. Figures in right panel represent the variation of \bar{R} . (d) $D = 0.6$, $\rho = 3$, (e) $A = 3$, $\rho = 3$, (f) $A = 3$, $D = 0.6$.

are shown in fig. 2.10. The low valued error bars represent the phase synchrony in the coupled neurons and the high valued error bars represent the reduction in phase synchrony by the external stimulus. The introduction of additional bursts by the external stimulus is visible from the increase in the value of the average bursting phase.

The irregularities induced by the spike input are studied using $CV_{s/t}$ and \bar{R} , with change in A , D and ρ , as shown in fig. 2.11. The variation of $CV_{s/t}$ with A confirm that high amplitude inputs have better ability to bring irregularity in bursting, as shown in fig. 2.11(a). The variation of $CV_{s/t}$ with D is presented in fig.2.11(b). A high value of $CV_{s/t}$ is found for values, $D > 0.2$. The higher desynchronising ability of high frequency input is presented in fig. 2.11(c). The desynchronising ability of the spike input is quantified using \bar{R} . The variation of

\bar{R} with A is shown in fig. 2.11(d). The higher the amplitude of the input, the better the desynchronising ability, represented by the low values of \bar{R} . The low value of \bar{R} for input is visible, with values $D > 0.3$, indicating high desynchronising ability, as shown in fig. 2.11(e). The better desynchronising ability for inputs with a low interval is shown in fig. 2.11(f).

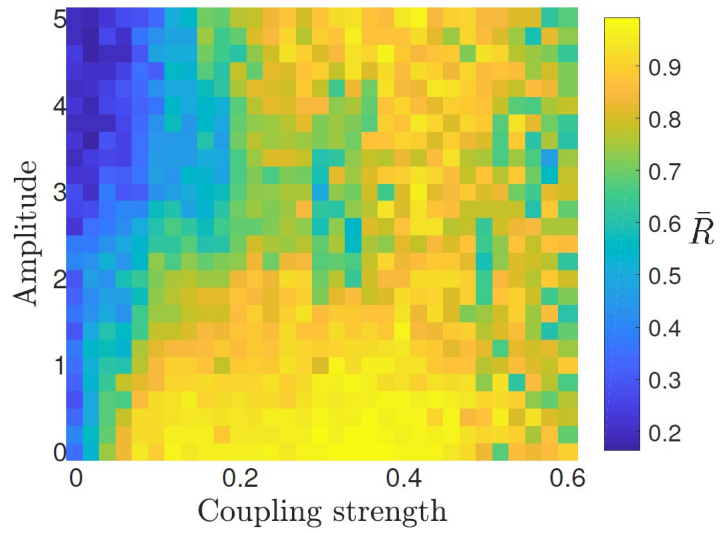
The studies on the influence of spike input on an excitatory mean field coupled system with intermittent synchrony is consistent with the results of the well synchronised system as well. It is found that high frequency input with optimum amplitude and pulse width has a better desynchronising ability.

The studies on the effect of spike input have been extended by analysing the parameter space g - A for low and high frequency inputs. Fig. 2.12(a) shows the parameter space diagram g - A for low frequency input. The lower number points representing desynchrony (blue points) in the figure show the inability of input to desynchronise the system. The system shows phase synchrony for strong coupling ($0.1 \leq g \leq 0.6$). Fig. 2.12(b) shows the parameter space diagram g - A for high frequency input. The abundance of blue points over yellow points proves the higher desynchronising ability of high frequency input. For low amplitudes, the input is unable to desynchronise the system, even if the frequency is high.

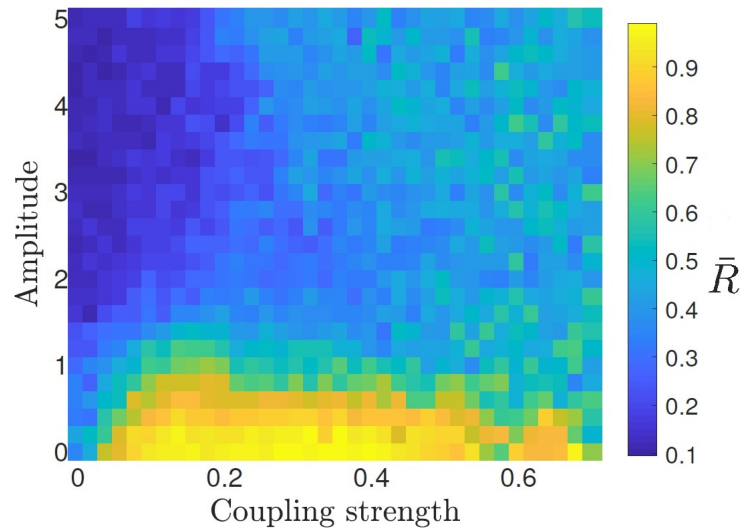
2.4 Influence of decaying coupling strength

Chimera states are complex and interesting spatiotemporal patterns in which coherent and incoherent states coexist. Even though chimera states are abundant in synaptically coupled neural network with nonlocal coupling, their emergence in non-synaptically coupled and globally coupled network is of great interest nowadays [104]. The decaying of coupling strength with distance is relevant in many real world systems like electromagnetic force, gravitational interaction, radioactive decay, etc.

In this section, the coupling strength is considered in a varying form, which decreases exponentially with distance between the neurons. The dynamic equation with decaying coupling strength is given by [9, 27]:



(a) $D = 0.6$ and $\rho = 20$



(b) $D = 0.6$ and $\rho = 3$

Figure 2.12: Parameter space showing the synchrony pattern for excitatory mean field coupled HR neurons under the influence of the external spike input. g is plotted along X-axis and A along Y-axis. (a) $D = 0.6$ and $\rho = 20$ (low frequency), (b) $D = 0.6$ and $\rho = 3$ (high frequency). Yellow and blue colours represent synchrony and desynchrony, respectively.

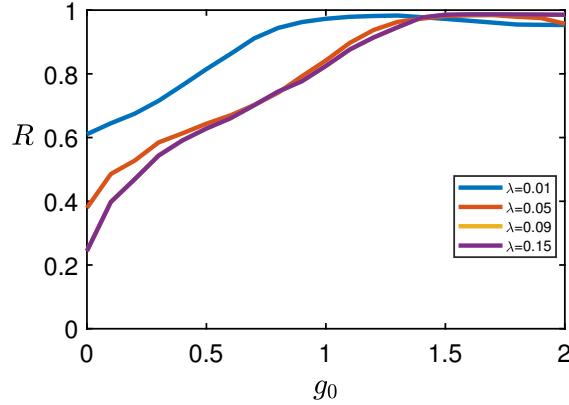


Figure 2.13: Variation of the statistical factor of synchronisation (R) with coupling constant (g) for different values of decay constant (λ).

$$\begin{aligned}
 \dot{x}_i &= y_i + ax_i^2 - bx_i^3 - z_i + I + \frac{1}{N-1} \sum_{\substack{j=1 \\ j \neq i}}^N g_{i,j}, \\
 \dot{y}_i &= c - dx_i^2 - y_i, \\
 \dot{z}_i &= r(s(x_i - x_e) - z_i), \quad i = 1, 2, \dots, N.
 \end{aligned} \tag{2.5}$$

The coupling term is given as $g_{i,j} = g_0 + \exp(-\lambda|i-j|)$, where g_0 is a constant, λ is the decay constant and $|i-j|$ gives the weight factor, which indicates the distance between the neurons.

2.4.1 Synchronisation scenario

The synchronisation scenario of a linear chain of HR neurons in the presence of decaying coupling constant is analysed in this section. The amount of synchrony is quantified using the statistical factor of synchronisation, R , given by the Eq. (1.3)

The total number of neurons in the network, N , is fixed at 135. The variation of R with g_0 for different values of λ is presented in fig. 2.13. At low values of g_0 , synchrony is found to decrease with an increase in the value of λ , up to a particular value of λ . Beyond that value, λ has no effect on the synchrony. But

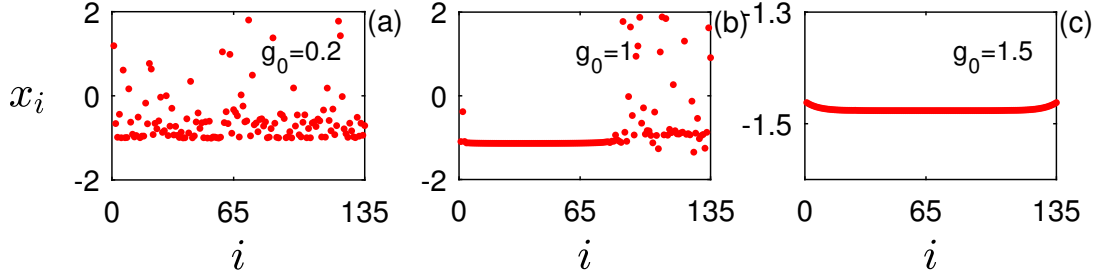


Figure 2.14: Emergence of chimera states under the influence of decaying coupling strength. (a) $g_0 = 0.2$, (b) $g_0 = 1$, (c) $g_0 = 1.5$. Here, $\lambda = 0.15$.

at higher values of g_0 , the synchrony is unaltered by the value of λ .

2.4.2 Emergence of chimera states

This section exhibits the different patterns induced in the network by the decaying coupling strength. The incoherence, chimera and coherent patterns obtained for different values of g_0 is shown in fig. 2.14. The value of λ is fixed at 0.15. At $g_0 = 0.2$, the system exhibits incoherent state, as shown in fig. 2.14(a). At $g_0 = 1$, chimera state is obtained and is presented in 2.14(b). The system exhibits complete coherence at $g_0 = 1.5$, which is shown in 2.14(c).

The emergence of chimera in the network due to the distance-dependent coupling is analysed with the help of a quantitative measure called strength of incoherence (SI) given in Eq. (1.13).

The variation of SI for different values of λ are presented in fig. 2.15. At low value of λ , the system exhibits chimeras at low values of g_0 , as shown in fig. 2.15(a). At higher values of g_0 , the system is at coherence. With the increase in value of λ , the probability of obtaining chimeras is also high, as shown in fig. 2.15(b). The chimera and coherent states obtained for $\lambda = 0.09$ are shown in fig. 2.15(c). At high values of λ , the system exhibits incoherent, chimera and coherent states which are shown in fig. 2.15(d). It is found that the probability of obtaining chimera states is high at moderate values of λ .

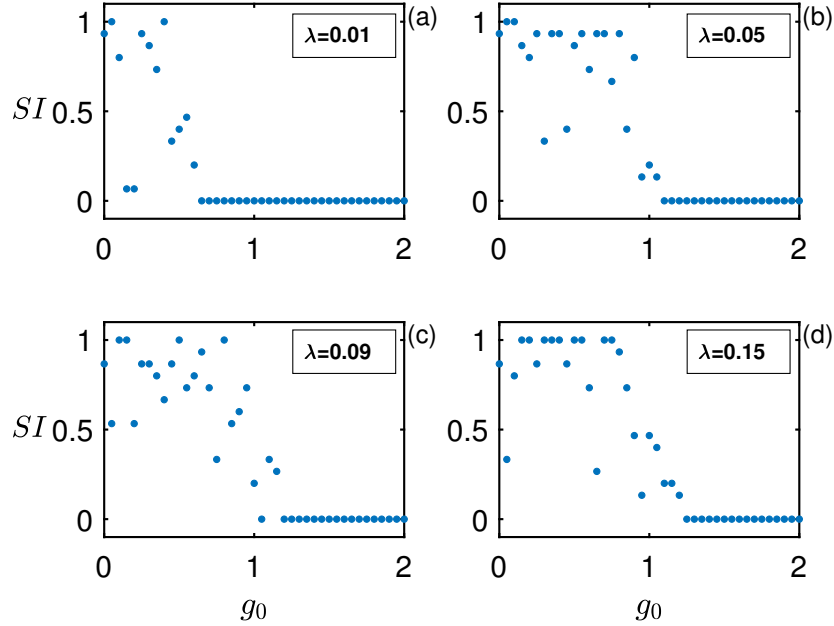


Figure 2.15: Variation of the strength of incoherence (SI) with coupling constant (g) for different values of decay constant (λ).

2.5 Results and conclusions

In this chapter, the mean field coupled HR network is analysed under the influence of a uniform and distance-dependent coupling scheme. The phase synchrony in a network of HR neurons with uniform mean field coupling and the capability of the external input to control the synchrony have been analysed. The $ISI-g$ diagram has been analysed to study the change in the dynamics of each neuron in the mean field network. In inhibitory mode, the mean field coupling has no influence on individual neuron dynamics, whereas in excitatory mode, the system shows regular bursting, irregular bursting, tonic spiking and eventually a stable state condition with an increase in coupling strength. The average phase lines with low valued error bars show that excitatory mean field coupling induces phase synchrony in the system, whereas inhibitory coupling induces desynchrony. The change in firing times of each neuron under mean field coupling has been studied using the coefficient of variability in spatial and temporal domains. The excitatory mean field coupling makes the neurons fire at the same time. The phase synchrony attained by the system has been quantified using the Kuramoto

order parameter. The system shows intermittent phase synchrony at weak coupling strength. The system shows well synchronised state for strong coupling. The capability of the input in controlling the synchrony of the excitatory mean field coupled system with phase synchrony is studied by varying amplitude, pulse width and interval. It is found that high frequency spike input with optimum amplitude and pulse width has a better capability to induce desynchrony in the system. The parameter space analysis substantiates the result. This study may find application in programming of the stimulator used in DBS treatment by focusing on three parameters (amplitude, frequency and pulse width), to deliver maximum efficacy and safety.

The network is studied under the influence of a coupling constant that decays exponentially with distance. The synchrony is found to decrease with an increase in the decay constant. However, the distance-dependent interactions are found to induce chimera states in the network. The probability of obtaining chimera states is found to be high at optimum values of the decay constant. At lower values of the decay constant, the system tends to be more in coherent states and chimera states are also observed. On the other hand, the system with a high decay constant exhibits incoherent, coherent and chimera states.

Chapter 3

Chimera states in HR network with ring topology

3.1 Introduction

Global coupling finds relevance in oscillators which acts back on themselves. In real life systems, neurons are connected by an enormous number of synapses and global coupling is the most suitable coupling scheme to represent them. The dynamics of globally coupled oscillators have attracted large attention recently [77, 78]. The synchronisation scenario of uniform mean field coupled neural network has been studied [105]. The symmetric coupling between identical oscillators leads to multistable states in which the synchronised and incoherently oscillating groups coexist [106–108]. Kuramoto and Battogtokh discovered the existence of these interesting spatiotemporal patterns in a ring network of symmetrically coupled phase oscillators [109] and named them chimera states. The coupling function always plays an important role in the studies on chimera. Earlier, the chimera patterns were limited to non-neural systems like phase oscillators. But in recent years, the existence of chimeras in neural networks has become a vastly studied research area. Many brain diseases such as Parkinson’s disease, epilepsy, Alzheimer’s disease, schizophrenia and brain tumours are related with chimera states in neural systems [110, 111].

Initially, it was assumed that nonlocal coupling was an essential condition for the existence of chimera states. This demand was reasonable because in nonlocal coupling, regions with different dynamics can coexist. The coupling range and coupling strength are the two control parameters to induce chimera states in the nonlocal coupling. But later, chimera states in oscillators with all to all coupling that emerged from the breaking of symmetry were discovered [112, 113]. Chimera like states were observed by Mishra *et al.* in globally coupled oscillators with attractive and repulsive mean field feedback [114]. The emergence of chimera states was demonstrated both theoretically and experimentally in an ensemble of Stuart–Landau oscillators under nonlinear global coupling [115]. Omelchenko *et al.* have observed the presence of multichimera states in nonlocally coupled Van der Pol oscillators by increasing nonlinearity in the local dynamics [116]. Chimera states were also observed in a network with purely local coupling [117].

The decaying of coupling strength with the distance between two oscillators is a more general and universal scheme that is relevant to real world systems. However, this coupling scheme was not widely studied in the context of chimeras and neural networks. But recently, chimera states were induced in ecological systems with global, nonlocal and local interactions, which were realised by power law exponent [118]. Long range interactions obeying a power law have also been taken into account in the synchronisation of ferromagnetic spin models [119], biological networks [120], hydrodynamic interactions of active particles [121, 122], coupled map lattices [123] and phase oscillators [124].

The phase transition of a one dimensional ring of coupled nonlinear phase oscillators from synchrony to complete desynchrony was induced by decreasing the range of interactions [125]. The control of connections in animal brains by a long range interaction with an algebraic scale has been studied [126]. The synchronisation properties of neural networks with distance-dependent coupling governed by a power law exponent have been analysed recently and are a newly emerging field of interest [37, 127]. Chimera states were also induced in systems for certain class of initial conditions [128–131]. The emergence of chimera states in a chemically coupled ring network with global, nonlocal and local interactions

and modified initial conditions were studied [64].

In this chapter, we have analysed the methods by which chimera states are induced in a network of mean field coupled HR neurons. The ring structure with global, nonlocal and local interactions is modified by introducing a power law exponent that reduces the contribution of neurons involved in coupling as the distance increases. The model and connection architecture are explained in section 3.2. The emergence of chimera pattern and synchronisation behaviour with power law exponent in a network with global interaction is numerically studied in section 3.3. Section 3.4 deals with the synchrony pattern and chimera states in nonlocally coupled network. The chimera states are induced in the system with local coupling by modifying the initial conditions and are presented in section 3.5. Section 3.6 summarises the results of the chapter.

3.2 The model and connection architecture

The collective dynamics of the mean field coupled HR neural network in ring topology with global, nonlocal and local interactions have been analysed in this section. These interactions are realised by controlling the number of neurons taking part in the coupling. The advantage of using this scheme is that we clearly get the number of interacting neurons, which is very important in mean field coupling. In addition to it, we have also given a distance gradient effect to the coupling using power law exponent. The value of power law exponent is so adjusted that even the farthest neuron in the coupling has a contribution. The model has the form [37]:

$$\begin{aligned}
 \dot{x}_i &= y_i + ax_i^2 - bx_i^3 - z_i + I + \frac{g}{2p} \sum_{j=1}^p \frac{x_{i-j} + x_{i+j}}{j^\alpha} \\
 \dot{y}_i &= c - dx_i^2 - y_i, \\
 \dot{z}_i &= r(s(x_i - x_e) - z_i), \quad i = 1, 2, \dots, N.
 \end{aligned} \tag{3.1}$$

Where N represents the total number of neurons in the network. The variables x_i , y_i and z_i , represent the membrane potential, spiking variable and bursting variable of i th neuron, respectively. y_i is constituted by the flow of Na^+ and K^+ ions and the flow of Ca^+ ions constitutes the z_i term [132]. The constant parameters a , b , c and d model the working of the fast ion channel and r represents the slow ion channel. s and x_e are other constant parameters of the system. I is the external current that controls the qualitative behaviour of the neurons and g is the mean field coupling strength. p is the number of neighbours to which each neuron is coupled in either direction of the ring and helps to limit the number of neurons in the coupling. So the coupling circle with radius, $r = \frac{p}{N}$ contains $2p$ neurons. α is the power law exponent, which gives the distance gradient effect in the structure. The power law exponent ensures that the nearest neighbour has a greater contribution to the coupling term.

The collective dynamics of mean field coupled HR neural network with global, nonlocal and local interactions and distance gradient effect have been studied by analysing Eq. (3.1). The values of the parameters are chosen as $a = 3$, $b = 1$, $c = 1$, $d = 5$, $r = 0.006$, $s = 4$, $x_e = -1.61$ and $I = 3.1$ [18, 133]. Neurons from 1 to N are placed in a ring structure. A periodic boundary condition $x_0 = x_N$, $x_{-1} = x_{N-1}$ and $x_{N+1} = x_1$ is considered to realise the ring configuration. The synchronisation scenario of the network is quantified with the statistical factor of synchronisation (R) and synchronisation error (E). The collective pattern formations are distinguished by the strength of incoherence (SI) and discontinuity measure (DM).

3.3 Global interaction

The network of HR neurons in ring topology with distance gradient effect induced by power law exponent has been analysed. The number of oscillators considered is 135. We have taken $p = \frac{N-1}{2}$ in Eq. (3.1) to realise global interaction. The collective dynamics and pattern formations are studied in this section.

The error in the network is another indicator of synchrony in the network.

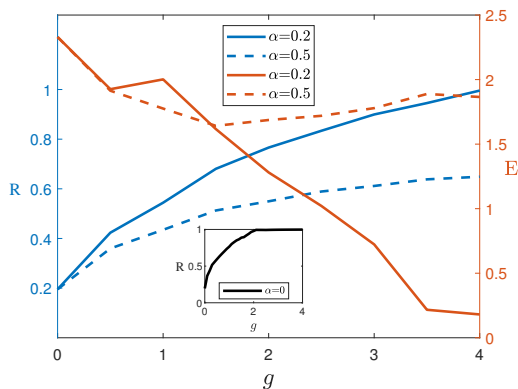


Figure 3.1: Variation of the statistical factor of synchronisation (R) and synchronisation error (E) with coupling strength (g) for different values of power law exponent (α). The variation of R with g for $\alpha = 0$ is shown in the inset.

The synchronisation error is obtained as [134]:

$$E = \left\langle \frac{1}{N-1} \sum_{j=2}^N \sqrt{(x_j - x_1)^2 + (y_j - x_1)^2 + (z_j - x_1)^2} \right\rangle_t \quad (3.2)$$

A zero value of synchronisation error suggests that all neurons follow the same trajectory and corresponds to complete synchrony. The variation of R and E with coupling strength, g has been analysed for different values of α , as shown in fig. 3.1. The plot in the inset shows the statistical factor of synchronisation for $\alpha = 0$. It shows that without distance gradient effect, the system acquires complete synchrony at $g = 2$. But as the values of α increases the value of coupling strength at which the system attains synchrony also increases. For higher values of α , the synchrony is unattainable. The variation of R , presented on the left side of the Y-axis, shows that complete synchrony is unattainable for high values of α . This result is substantiated by the variation of E on the right Y-axis. We have studied the system for different values of α and it is inferred that for $\alpha > 0.5$, the global interaction transforms to nonlocal coupling. So, we have analysed the system for $\alpha \leq 0.5$.

The non-existence of chimeras in the mean field coupled HR neurons with global interaction, for $\alpha = 0$, has been analysed in fig. 3.2. The left panel of the figure depicts the snapshots of the network and the right panel shows

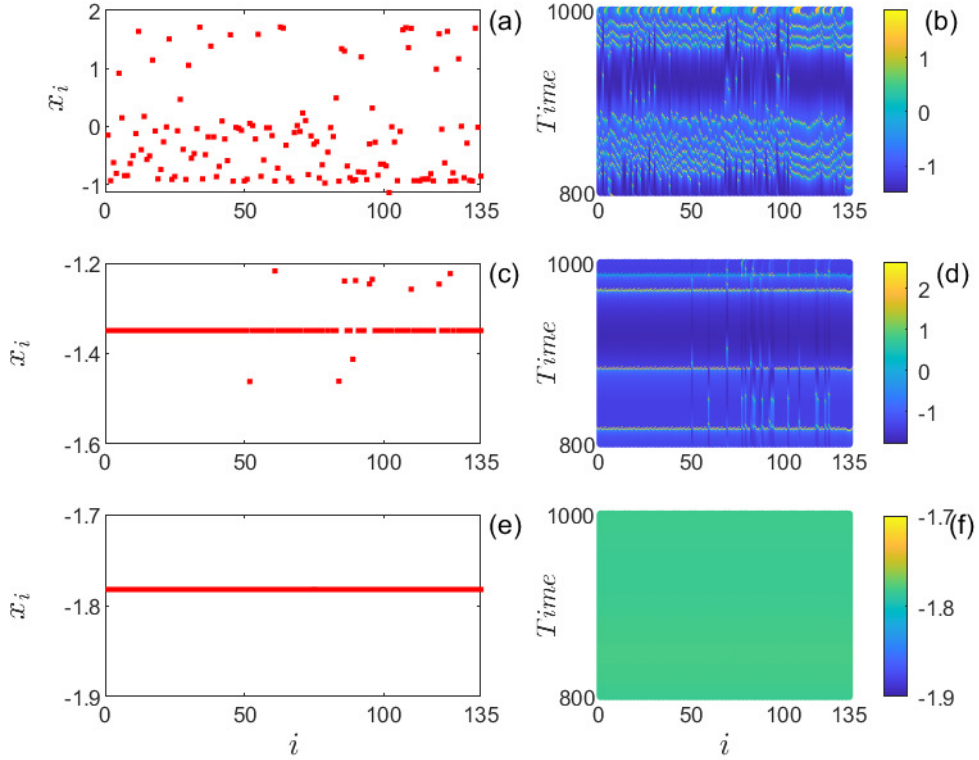


Figure 3.2: Non-existence of chimera states in the network with global interaction. Left panel shows the snapshots of membrane potential with $\alpha = 0$, for various values of coupling strength (g). (a) desynchrony at $g = 0.1$, (c) imperfect synchrony at $g = 1.1$, (e) synchrony at $g = 2.3$. The right panel ((b), (d) and (f)) shows the corresponding spatiotemporal patterns. The colourbar in the right panel represents the membrane potential, x .

the corresponding spatiotemporal patterns. Fig. 3.2(a) presents the incoherent system. The corresponding spatiotemporal pattern is presented in fig. 3.2(b) shows that the dynamics is chaotic bursting. The imperfect synchronised system is shown in fig. 3.2(c) and the dynamics of the network is chaotic spiking as presented in fig. 3.2(d). The coherent system is presented in fig. 3.2(e). Fig. 3.2(f) shows that the dynamics is amplitude death for coherent state.

The distance gradient effect induces chimera patterns in the network. The interesting patterns in mean field coupled HR neurons for different values of g and α are analysed. The system passes through incoherent, multichimera, chimera and coherent states as the value of g is increased, which is shown in the left panel of fig. 3.3. The incoherent system is presented in fig. 3.3(a) and the corresponding spatiotemporal pattern in fig. 3.3(b) indicates that the dynamics

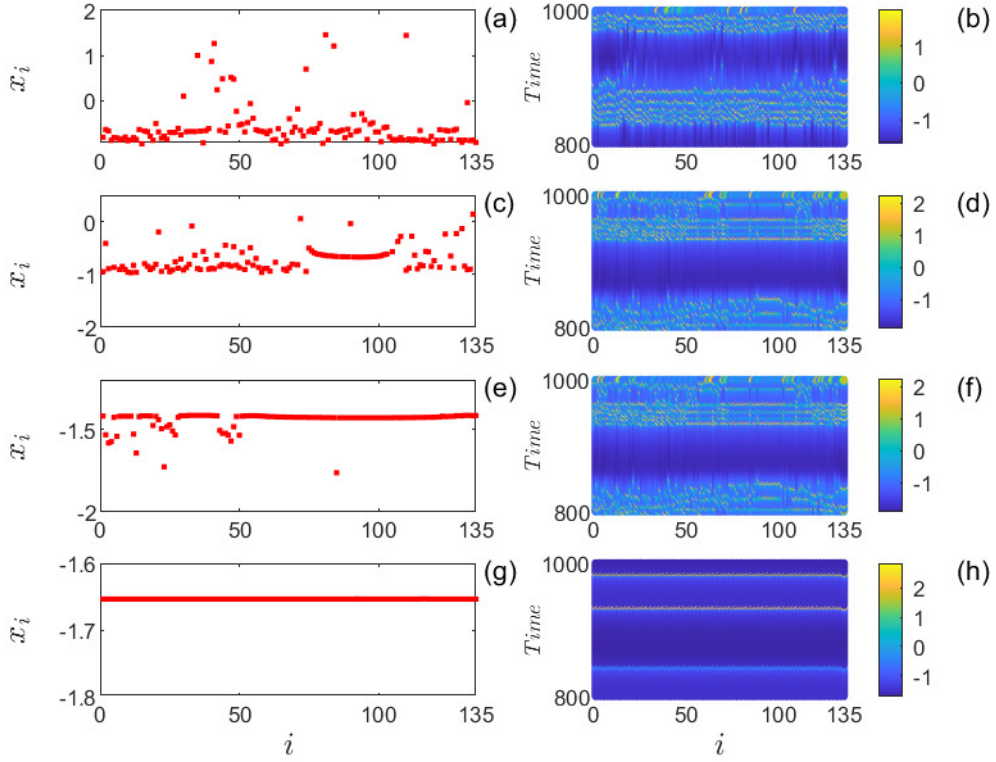


Figure 3.3: Emergence of chimera states under the influence of power law exponent in the network with global interaction. Left panel shows the snapshots of membrane potential with $\alpha = 0.2$, for various values of coupling strength (g). (a) incoherence at $g = 0.5$, (c) chimera at $g = 1.3$, (e) multichimera at $g = 2.2$, (g) coherence at $g = 2.5$. The right panel ((b), (d), (f) and (h)) shows the corresponding spatiotemporal patterns. The colourbar in the right panel represents the membrane potential, x .

is chaotic bursting. The chimera state obtained for $g = 1.3$ is presented in fig. 3.3(c). The dynamics is chaotic bursting as presented in the fig. 3.3(d). The multichimera state obtained is presented in fig. 3.3(e). The dynamics is chaotic bursting as represented in the fig. 3.3(f). The coherent system is presented in fig. 3.3(g) and the dynamics is chaotic spiking which is presented in fig. 3.3(h).

The existence of incoherent, chimera, multichimera and coherent states in a mean field coupled HR neural network with distance gradient effect is studied using Eqs. (1.13) and (1.14), respectively, by varying α and g , as shown in fig. 3.4. The values of other parameters are chosen as follows: $M = 15$ and $\epsilon = 0.01$. For $\alpha = 0$, the unattainability of chimera states is justified, as shown in figs. 3.4(a) and 3.4(b). The variation of SI with g for different values of α is shown

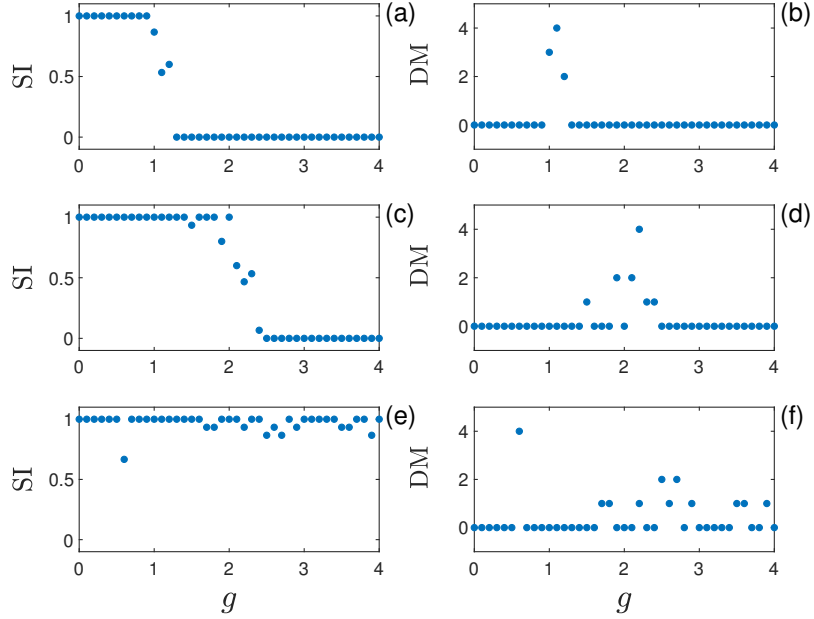


Figure 3.4: Strength of incoherence (SI) and discontinuity measure (DM) are plotted against coupling strength (g). The left panel shows SI at (a) $\alpha = 0$, (c) $\alpha = 0.2$ and (e) $\alpha = 0.5$. The right panel ((b), (d) and (e)) shows the DM for the corresponding values. Here $N = 135$, $M = 15$ and $\epsilon = 0.01$.

in figs. 3.4(c) and 3.4(e) and the corresponding plots for DM are shown in figs. 3.4(d) and 3.4(f). The emergence of chimera and multichimera states with the introduction of power law exponent in network with global interaction are well visible from them. The state of coherence is unattainable at high values of α . This is in complete agreement with the results of synchronisation analysis.

The analysis of mean field coupled HR neurons with the distance gradient effect in ring topology with global interaction shows that the power law exponent reduces the synchrony and induces chimera states in the network.

3.4 Nonlocal coupling

The nonlocal interaction in the neural network of HR neurons is realised by limiting the number of neurons with the help of p . α induces the distance gradient effect in the network. The synchrony pattern is quantified with statistical factor of synchronisation and error analysis. The existence of chimera and multichimera patterns are also analysed, for various values of α and p . The maximum value

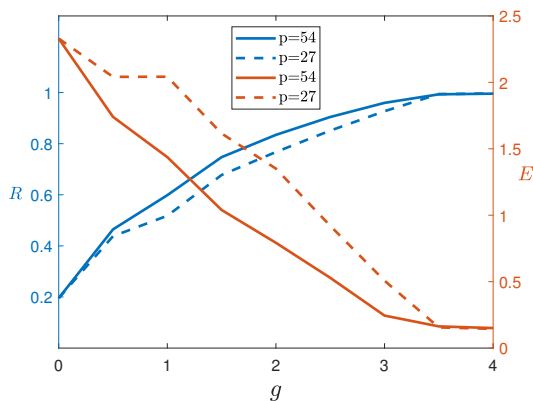


Figure 3.5: Variation of the statistical factor of synchronisation (R) and the synchronisation error (E) with the coupling strength (g) in the network with nonlocal interactions. Here $\alpha = 0.1$.

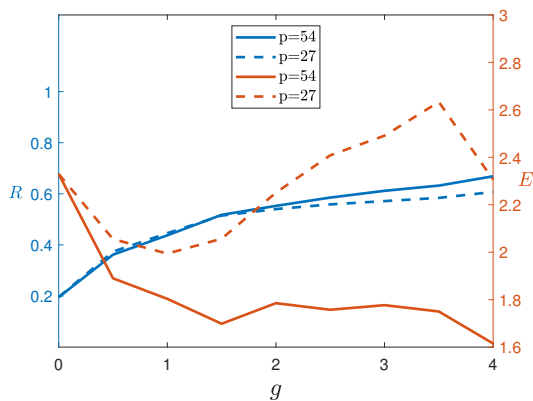


Figure 3.6: Variation of the statistical factor of synchronisation (R) and the synchronisation error (E) with coupling strength (g) in the network with nonlocal interaction. Here, $\alpha = 0.5$.

of α is chosen as 0.5, so that the farthest neuron on the coupling circle marks its contribution towards the coupling term.

The variation of the statistical factor of synchronisation and the synchronisation error for low value of α is presented in fig. 3.5. The number of coupling neurons is taken as $p = 54$ (*i.e.*, $r = 0.4$) and $p = 27$ (*i.e.*, $r = 0.2$). From the figure, it is clear that the synchrony is independent of the number of neurons taking part in the coupling. The system shows complete synchrony or coherence state, for low values of α .

The variation of synchrony level with g for a high value of α is shown in fig. 3.6. This study verifies that the synchrony level is independent of the number of neurons in the coupling circle. The synchrony is low in the system with a high

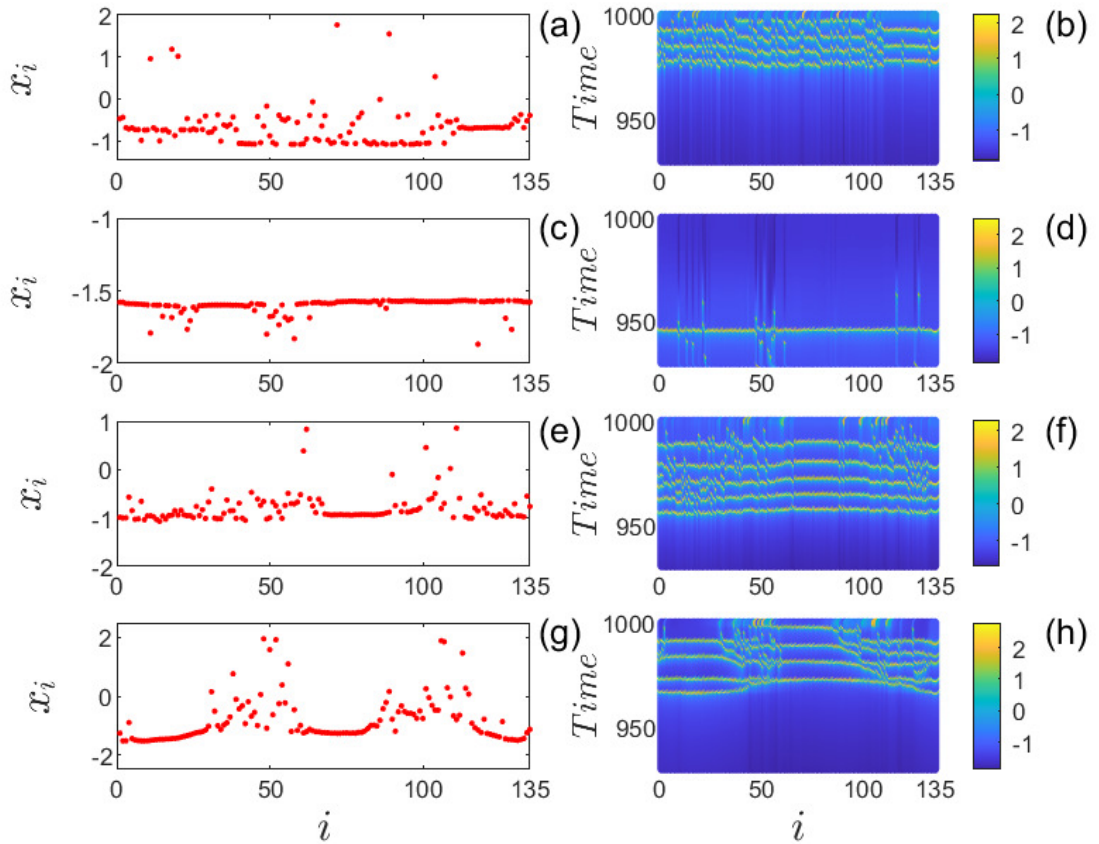


Figure 3.7: Emergence of chimera and multichimera states induced by the interplay of nonlocal coupling and power exponent law. Left panel shows the snapshots of membrane potential. (a) chimera at $p = 57$, $\alpha = 0$, $g = 0.8$, (c) multichimera at $p = 60$, $\alpha = 0.1$, $g = 1.4$, (e) chimera at $p = 54$, $\alpha = 0.2$, $g = 1.7$, (g) multichimera $p = 27$, $\alpha = 0.1$, $g = 2.2$. The right panel shows the corresponding spatiotemporal patterns. The colourbar represents the membrane potential, x .

power law exponent.

The existence of chimera or multichimera patterns in the mean field coupled neural network for different values of p and α is shown in fig. 3.7. It is observed that system exhibits chimera states by limiting the number of neurons in the coupling circle alone, *i.e.*, for $\alpha = 0$, as shown in fig. 3.7(a). The corresponding spatiotemporal pattern in fig. 3.7(b) shows that the dynamics is chaotic bursting. The multichimera state is presented in fig. 3.7(c) and the corresponding dynamics is spiking as shown in fig. 3.7(d). Fig. 3.7(e) presents the chimera state and the corresponding chaotic bursting character is shown in fig. 3.7(f). Fig. 3.7(g) again shows the multichimera state and the dynamics is chaotic bursting as shown in

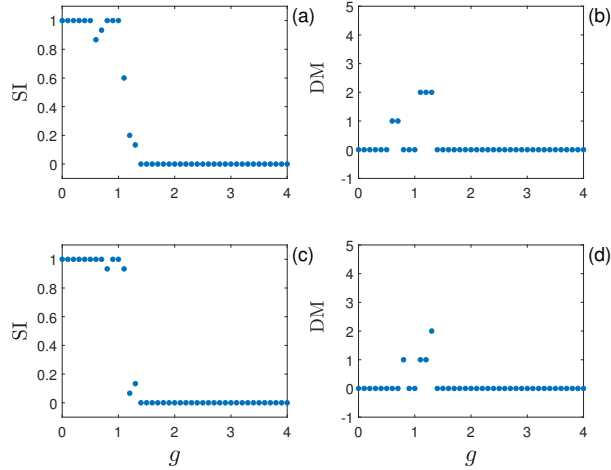


Figure 3.8: Strength of incoherence (SI) and discontinuity measure (DM) are plotted against the coupling strength (g). The left panel shows SI for (a) $p = 54$ and (c) $p = 27$. The right panel (b) and (d) shows DM for the corresponding values. Here, $\alpha = 0.1$.

fig. 3.7(h).

The variation of SI and DM with g for different values of α and p has been analysed. The left panel of fig. 3.8 represents the variation of SI with g for a low value of α and the right panel shows the corresponding variation of DM. The chimera and multichimera states for the network with high values of α are presented in fig. 3.9. The variation of SI with g is plotted in the left panel and that for DM is shown in the right panel. It is found that for fixed value of p , the power law exponent enhances the possibility of obtaining chimera or multichimera states in the network.

3.5 Nearest neighbour coupling

The network of HR neurons with local (nearest neighbour) interaction is analysed in this section by fixing $p = 1$ in Eq. (3.1). The statistical factor of synchronisation and synchronisation error have been studied by varying, g , as shown in fig. 3.10. The synchronisation pattern on the left Y-axis shows a step like function and error analysis on the right Y-axis of the plot substantiates the result. This marks the abrupt transition of the system from desynchrony to complete synchrony.

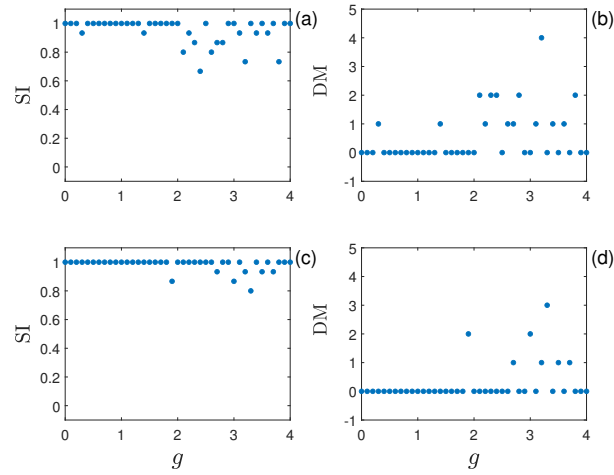


Figure 3.9: Strength of incoherence (SI) and discontinuity measure (DM) are plotted against coupling strength (g). The left panel shows the SI at (a) $p = 54$ and (c) $p = 27$. The right panel (b) and (d) shows the DM for corresponding values. Here, $\alpha = 0.5$.

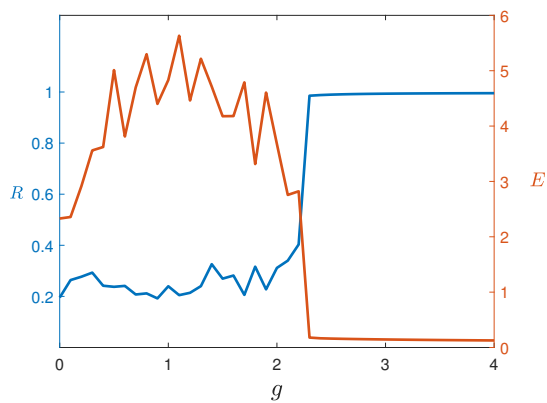


Figure 3.10: Variation of the statistical factor of synchronisation and the synchronisation error with the coupling strength for local coupling in mean field coupled HR neurons in ring topology.

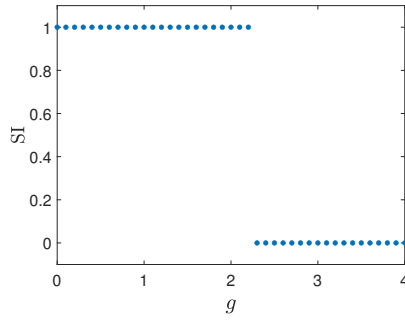


Figure 3.11: Strength of incoherence (SI) of mean field coupled HR neurons with local coupling without modifications in initial conditions.

On studying the SI for local coupling, it is found that the system is incapable of attaining chimera or multichimera states, as shown in fig. 3.11. The complete incoherence upto $g < 2.3$ and coherence for $g \geq 2.3$ are in good agreement with the synchrony analysis.

Since the nearest neighbour coupling is incapable of inducing chimera or multichimera states, we have analysed the system by modifying the initial conditions as follows: $x_{i0} = 0.01(i - \frac{N-1}{2})$, $y_{i0} = 0.02(i - \frac{N-1}{2})$, $z_{i0} = 0.03(i - \frac{N-1}{2})$ for $i = 1, 2, \dots, \frac{N-1}{2}$ and $x_{i0} = 0.1(\frac{N-1}{2} - i)$, $y_{i0} = 0.12(\frac{N-1}{2} - i)$, $z_{i0} = 0.21(\frac{N-1}{2} - i)$ for $i = \frac{N-1}{2} + 1, \dots, N$ [64].

The snapshot of the chimera state is presented in fig. 3.12(a). The spatiotemporal pattern shown in fig. 3.12(b) suggests that the chimeras observed are travelling chimera, i.e, it has a propagating nature over space and time. At a particular time, a sub population of neurons show desynchronised state and others show synchronised state. As time changes, the states also change. The fig. 3.12(c) shows the multichimera state and the fig. 3.12(d) shows that the multichimera state is travelling in nature.

The variation of SI and DM with g is presented in figs. 3.13(a) and 3.13(b), respectively. This analysis supports the emergence of chimera and multichimera states as a result of modified initial conditions.

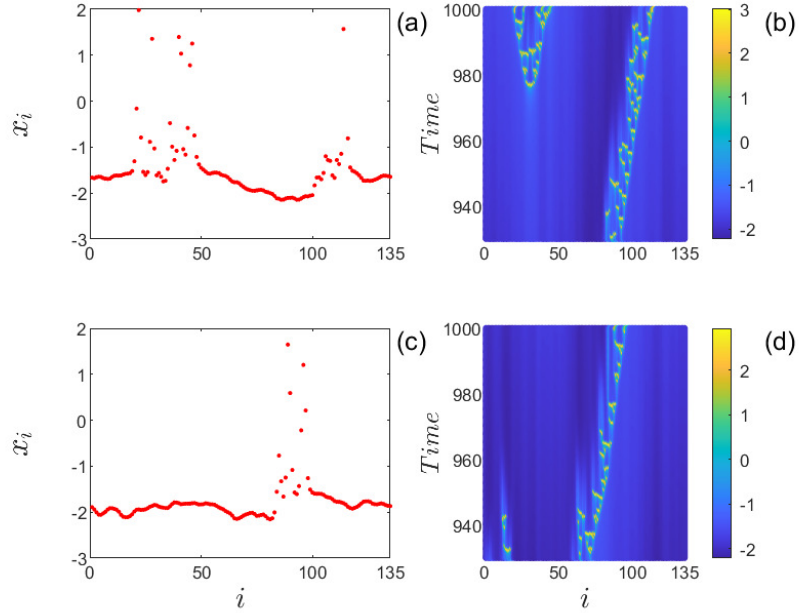


Figure 3.12: Emergence of the chimera states by modified initial conditions in the network with local coupling. Left panel shows the snapshots of membrane potential. (a) multichimera at $g = 2.19$, (c) chimera at $g = 2.21$. Right panel (b) and (d) shows the spatiotemporal patterns for corresponding values. The colourbar represents the membrane potential, x .

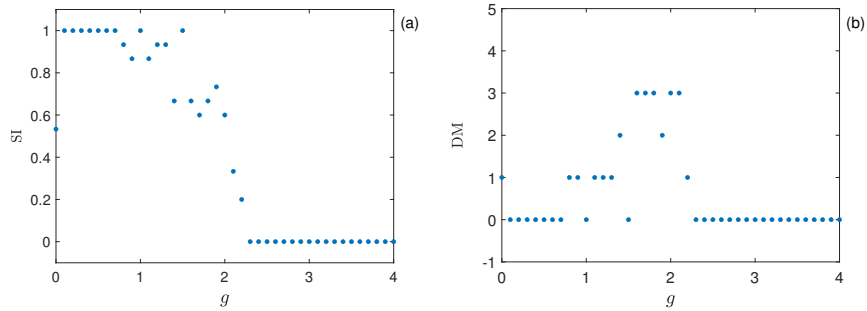


Figure 3.13: Variation of (a) strength of incoherence (SI) and (b) discontinuity measure (DM) for different values of mean field coupling strength (g) for locally coupled Hindmarsh-Rose neurons with modified initial conditions. Here $N = 135$, $M = 15$ and $\epsilon = 0.01$.

3.6 Results and conclusions

The techniques for inducing chimera states in neural networks with non-synaptic coupling are presented in this chapter. Global, nonlocal and local interactions are realised in the mean field coupled HR neurons with ring topology by limiting the number of neurons involved in the coupling. In addition, the contribution from the neurons is given a slow gradient effect using the power law exponent. The synchrony level is quantified using the statistical factor of synchronisation and the synchronisation error. The existence of chimera states is verified using strength of incoherence. The discontinuity measure distinguishes the chimera from multichimera states. In global interaction, it is found that power law exponent reduces synchrony in the network and also induces chimera states. In nonlocal coupling, the synchrony level is found to be independent of the number of neurons contributing to the coupling term, whereas the distance gradient effect reduces synchrony in the network. The chimera states are induced by limiting the number of neurons in the coupling. The power law exponent enhances the possibility of chimera states in the network. In the nearest neighbour or local coupling, chimera and multichimera states are induced by modifications in initial conditions of the network.

The emergence of chimera states in networks with time delayed synaptic coupling, non-synaptic (ephaptic) coupling, distance gradient coupling and modified initial conditions is an area of great interest nowadays. The studies on chimera states aim to explore the complex functions of the brain with the help of networks of interconnected neurons.

Chapter 4

Synchrony and pattern formations by varying coupling phase

4.1 Introduction

The synchronisation of neural networks in numerous brain regions, including the hippocampus, thalamus, neocortex and cerebellar cortex, is characterised by the transition between anti-phase and in-phase oscillations in neurons [135]. When the coupled neurons fire at the same time, then it is called in-phase oscillations. Anti-phase oscillations arise when one neuron exhibits spiking behavior while the other neuron is at rest [136]. The long range in-phase oscillations are considered to be beneficial for the coordination of various functions taking part in different parts of the brain [137]. These rhythmic transitions are also crucial for animal mobility [138]. Anti-phase oscillations were observed experimentally in different functions such as attention task, sleeping and resting state of the neurons [139–144]. A model consisting of two electrically coupled pacemakers was analysed to study the in-phase and anti-phase oscillations [145]. The factors that lead to stable anti-phase oscillations were analysed in the model of neurons with biological applications [146, 147]. Travelling chimera were used to identify the tumorous cells [44]. Researchers have proposed various methods to induce these oscillations [138, 148]. Experiments on electronic neurons showed in-phase

synchrony for positive electrical couplings and anti-phase oscillations for negative couplings. In chemical coupling, in-phase synchrony was found in excitatory mode and anti-phase oscillations in inhibitory mode [149]. The HR network showed interesting in-phase and anti-phase oscillations in electrical synapses for moderate and strong couplings [150].

Chimera states and travelling waves in neural networks are of interest in clinical studies and research, with numerically confirmed results using FitzHugh-Nagumo (FHN) and leaky integrate and fire models [108]. Omelchenko *et al.* introduced multichimera states in FHN oscillators using a rotation matrix and cross coupling of state variables [62]. Researchers analysed the influence of rotation matrix on FHN and HR neurons, fixing coupling phase [108, 151, 152]. These spatiotemporal patterns can be brought about by different means, including distance-dependent coupling [127, 153], nonlocal interactions [154], cross coupling or coupling through rotation matrices [152]. The formation of chimera states can also be attributed to changes in initial conditions or network structure [155]. Another possibility is that chimera states emerge inherently as a result of the stabilisation effect of an incoherent subgroup on a coherent subgroup [156]. The underlying principle behind these methods is symmetry breaking [157].

The synchronisation scenario and pattern formations in the HR neural network coupled by a rotation matrix, which helps to realise different coupling schemes such as self, cross and mixed modes by varying the coupling phase are analysed. This chapter is organised as follows: The model for two coupled HR systems and the generation of in-phase and anti-phase oscillations are presented in section 4.2. The synchronisation scenario and the analysis of its stability using the Lyapunov function approach are also discussed in this section 4.2.1 and 4.2.2, respectively. Section 4.3 is devoted to the analysis of N coupled network with self and cross coupling of variables. The synchrony of the network is quantified and the patterns obtained are presented. The quantifiers for incoherence, chimera, multichimera and coherence are also calculated. Results are discussed in Section 4.4.

4.2 In-phase and anti-phase oscillations

The influence of self, mixed and cross coupling of state variables on two coupled HR neurons has been studied [44, 152]. The dynamical system is expressed by the equations of the form:

$$\begin{aligned}
 \dot{x}_i &= y_i - ax_i^3 + bx_i^2 - z_i + I + g[b_{11}(x_j - x_i) + b_{12}(y_j - y_i) + b_{13}(z_j - z_i)], \\
 \dot{y}_i &= c - dx_i^2 - y_i + g[b_{21}(x_j - x_i) + b_{22}(y_j - y_i) + b_{23}(z_j - z_i)], \\
 \dot{z}_i &= r(s(x_i - x_e) - z_i) + g[b_{31}(x_j - x_i) + b_{32}(y_j - y_i) + b_{33}(z_j - z_i)], \quad i, j = 1, 2.
 \end{aligned}
 \tag{4.1}$$

The membrane potential of the neuron is represented by x_i . The flow of Na^+ ions constitute the spiking variable, y_i , whereas, the bursting variable z_i is constituted by the flow of Ca^+ ions [102]. The constant parameters a , b , c and d model the working of the fast ion channel and r represents the slow ion channel. s and x_e are other constant parameters of the system [9, 158]. Constants r and s approximate the biological behaviour of the model [159]. g represents the coupling strength and I is the external current entering the neuron. The interaction takes place through a cross coupling scheme between the variables x_i , y_i and z_i , which has been modelled by a coupling matrix as,

$$B = \begin{pmatrix} b_{11} & b_{12} & b_{13} \\ b_{21} & b_{22} & b_{23} \\ b_{31} & b_{32} & b_{33} \end{pmatrix}$$

The system is analysed under the influence of rotational matrix of the form:

$$B = \begin{pmatrix} \cos \delta & \sin \delta & 0 \\ -\sin \delta & \cos \delta & 0 \\ 0 & 0 & 0 \end{pmatrix}
 \tag{4.2}$$

where δ , belonging to $[-\pi, \pi)$, is the coupling phase. The different values of δ give

the coupling matrices that enable us to realise self, mixed and cross couplings, in inhibitory and excitatory modes. For example, when $\delta = 0$, the elements of the matrix are $b_{11} = 1, b_{12} = 0, b_{21} = 0$ and $b_{22} = 1$. These elements induce the self coupling in x and y of Eq. (4.1). When $\delta = \pi/2$, we have $b_{11} = 0, b_{12} = 1, b_{21} = -1$ and $b_{22} = 0$. Here the x variable is cross coupled to y and vice versa. Also, the cross coupling of x in y is inhibitory. Similarly, when $\delta = \pi/4$, we have mixed interactions between the x and y variables. Thus, the coupling phase represents how a variable is coupled to another variable of the same neuron. The coupling matrix in Eq. (4.2) helps to simplify the representation and realisation of these interactions by adjusting a single parameter δ . By continuously varying the value of δ , we have analysed the bifurcation point at which the effect of cross interaction overrides the effect of self coupling and vice versa. The parameters are chosen as: $a = 1, b = 3, c = 1, d = 5, r = 0.006, s = 4, x_e = -1.61, I = 3.1$ [18]. Initial conditions are chosen randomly to lie in the range $[-0.5, 0.5]$. The results presented in the entire work are consistent for any choice of initial values.

The anti-phase and in-phase bursting dynamics in the system with electrical coupling in self, mixed and cross interactions in x and y variables is analysed by varying δ in Eq. (4.2) and the plots are shown in fig. 4.1. When $\delta = -\pi$, the self coupling is inhibitor in x and y . The system shows anti-phase bursts as shown in fig. 4.1(a). When $\delta = -\frac{\pi}{2}$, the coupling is cross in x and y , that is, activator-inhibitor mode and the system exhibits anti-phase bursting as shown in fig. 4.1(b). In this case, the cross coupling of y variable to x is inhibitory. The self activator synapse in x and y is realised with $\delta = 0$ and the system shows in-phase burst synchrony as shown in fig. 4.1(c). When $\delta = \frac{\pi}{4}$, the coupling is mixed (self and cross), with activator self coupling and activator-inhibitor cross coupling. The oscillations of the neurons are in-phase as shown in fig. 4.1(d). The activator cross coupling of y variable in x , when $\delta = \frac{\pi}{2}$, induces in-phase synchrony, as shown in fig. 4.1(e). However, the synchrony is obtained at a comparatively high coupling strength as the coupling of x in y is inhibitory. An activator-activator cross coupling is realised when b_{21} is chosen to be positive which promotes synchronisation at a weaker coupling strength as shown in fig.

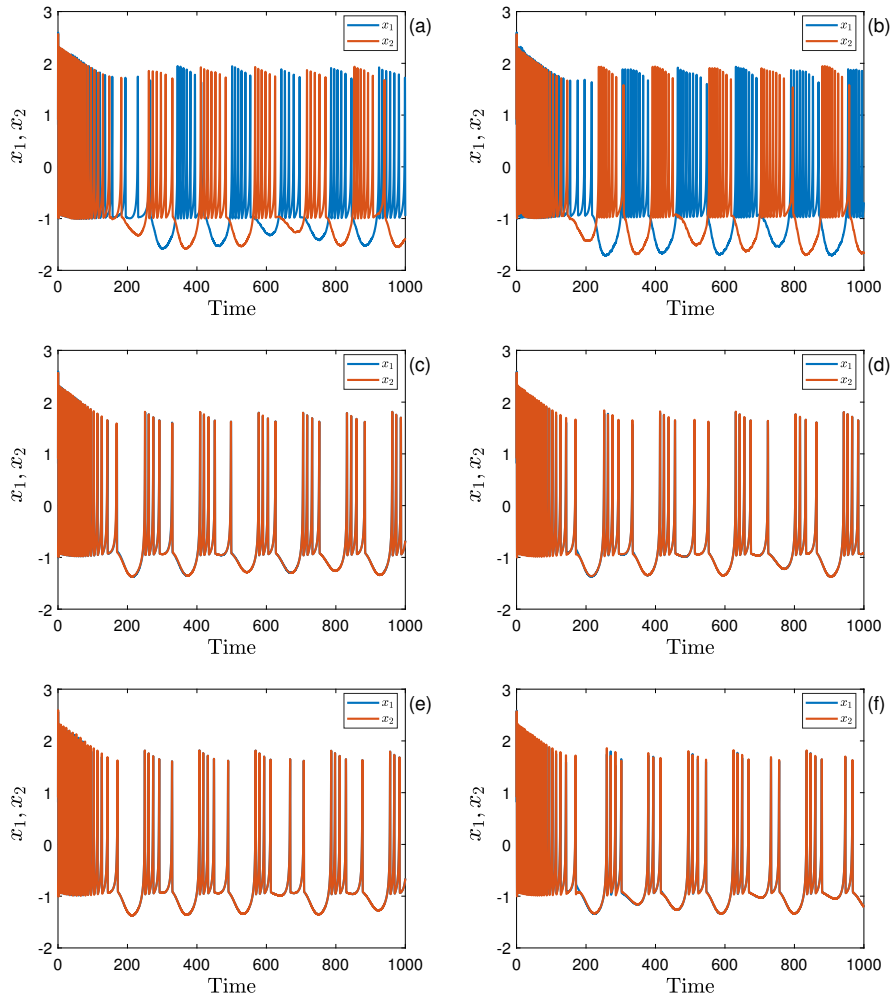


Figure 4.1: Time series of the membrane potential of two coupled HR neurons for different coupling phases. (a) $\delta = -\pi$, $g = 0.02$ (b) $\delta = \frac{-\pi}{2}$, $g = 0.04$, (c) $\delta = 0$, $g = 0.02$, (d) $\delta = \frac{\pi}{4}$, $g = 0.09$. (e) $\delta = \frac{\pi}{2}$, $g = 0.32$, (f) $\delta = \frac{\pi}{2}$, $g = 0.12$, $b_{21} = \sin \delta$.

4.1(f). The system exhibits anti-phase oscillations for inhibitor coupling in the x variable and in-phase synchrony for activator coupling, whether the coupling is self or cross. Synchrony is obtained at a lower coupling strength when the nature of the connection is activator-activator in cross coupling.

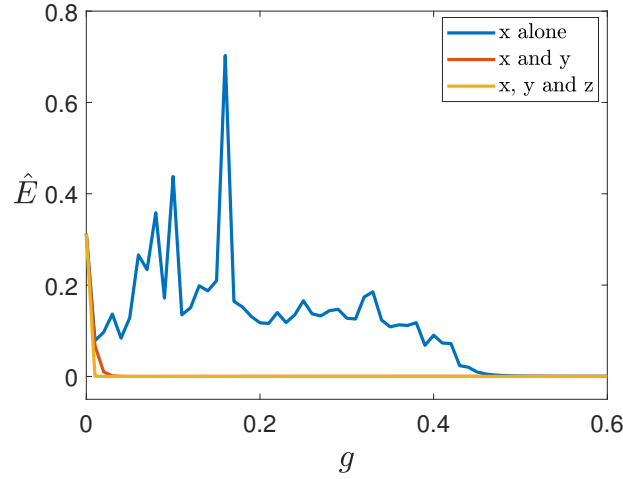


Figure 4.2: Synchronisation error of two coupled HR neurons with self coupling in the state variables.

4.2.1 Synchronisation scenario

The synchrony in the system is analysed with the help of normalised synchronisation error given by the equation [160]:

$$\hat{E} = \sqrt{\frac{e_x^2 + e_y^2 + e_z^2}{x_1^2 + y_1^2 + z_1^2 + x_2^2 + y_2^2 + z_2^2}}. \quad (4.3)$$

Where $e_x = x_2 - x_1$, $e_y = y_2 - y_1$, $e_z = z_2 - z_1$. The synchronisation scenario of two coupled system has been analysed for self coupling in x , y and z variables and is shown in fig. 4.2. The blue line represents the synchronisation error with self coupling in x alone which is realised with $b_{11} = 1$ and all the other components are zero. The synchrony is obtained at $g \approx 0.5$. The self coupling in y along with x , realised with $b_{11} = b_{22} = 1$, helps to induce synchrony at a lower coupling strength. The red line shows that synchrony is obtained at $g \approx 0.01$. When $b_{11} = b_{22} = b_{33} = 1$ *i.e.*, self coupling in x , y and z variables further reduces the value of g at which synchrony is obtained, as represented by yellow line. The coupling strength at which synchronisation is obtained decreases as the number of self coupled variables increases.

4.2.2 Stability of synchronisation

The stability of the synchrony induced under in-phase bursting dynamics is verified in this section. The coupling matrix is taken of the form as in Eq. (4.2). This matrix is a simple way to realise self activator coupling (b_{11}, b_{22}) and activator–inhibitor cross coupling (b_{12}, b_{21}) by a single parameter δ . The choice of cross coupling in and of z variable is discarded, because only cross coupling in x and y exhibits bursting dynamics. We have analysed the system of HR neurons in three different cases: (i) Self coupling in x and y , $\delta = 0$. (ii) mixed coupling in x and y , $\delta = \frac{\pi}{4}$. (iii) Cross coupling in x and y , $\delta = \frac{\pi}{2}$.

The time derivative of the Lyapunov function is used to determine the stability of the system under the influence of different coupling phases [161]. The complete synchronisation of the coupled system occurs when the two neurons exhibit identical behaviour, that is,

$$\begin{aligned} \|x_2(t) - x_1(t)\| &\rightarrow 0 \\ \|y_2(t) - y_1(t)\| &\rightarrow 0 \\ \|z_2(t) - z_1(t)\| &\rightarrow 0 \end{aligned} \tag{4.4}$$

At synchronised states,

$$\begin{aligned} x_1(t) &= x_2(t) = x(t) \\ y_1(t) &= y_2(t) = y(t) \\ z_1(t) &= z_2(t) = z(t) \end{aligned} \tag{4.5}$$

The error states $e_x = x_2 - x_1, e_y = y_2 - y_1, e_z = z_2 - z_1$, are defined by introducing coordinates that are transverse to the synchronisation manifold. We

have the error dynamics of the system without self coupling in z variable as:

$$\begin{aligned}\dot{e}_x &= e_y - a(x_2^3 - x_1^3) + b(x_2^2 - x_1^2) - e_z - 2g \cos \delta e_x - 2g \sin \delta e_y \\ \dot{e}_y &= -d(x_2^2 - x_1^2) - e_y + 2g \sin \delta e_x - 2g \cos \delta e_y \\ \dot{e}_z &= rse_x - re_z\end{aligned}\tag{4.6}$$

We define a new variable $U = x_2 + x_1$. Then, $x_2^2 - x_1^2 = Ue_x$ and $x_2^3 - x_1^3 = e_x(e_x^2 + 3U^2)/4$

On simplifying,

$$\begin{aligned}\dot{e}_x &= (-0.25a(e_x^2 + 3U^2) + bU - 2g \cos \delta)e_x + (1 - 2g \sin \delta)e_y - e_z \\ \dot{e}_y &= (2g \sin \delta - dU)e_x - (1 + 2g \cos \delta)e_y \\ \dot{e}_z &= rse_x - re_z\end{aligned}\tag{4.7}$$

The Lyapunov functions are evaluated from this error dynamics. In Lyapunov function approach, we define a continuous, positive definite Lyapunov function, V , using the Eq. (4.7), which has the form:

$$V(e_x, e_y, e_z) = \frac{1}{2}[e_x^2 + e_y^2 + e_z^2]\tag{4.8}$$

The first derivative of the Lyapunov function is continuous and the time derivative along trajectories of the error dynamical system gives

$$\frac{dV}{dt} = e_x \dot{e}_x + e_y \dot{e}_y + e_z \dot{e}_z\tag{4.9}$$

On substitution and simplifying,

$$\begin{aligned}\frac{dV}{dt} &= (-0.25a(e_x^2 + 3U^2) + bU - 2g \cos \delta)e_x^2 - (1 + 2g \\ &\quad \cos \delta)e_y^2 - re_z^2 + (1 - dU)e_x e_y + (rs - 1)e_x e_z\end{aligned}\tag{4.10}$$

The terms x_1, x_2, e_x, e_y, e_z in Eq. (4.10) is obtained by solving Eqs. (4.1) and

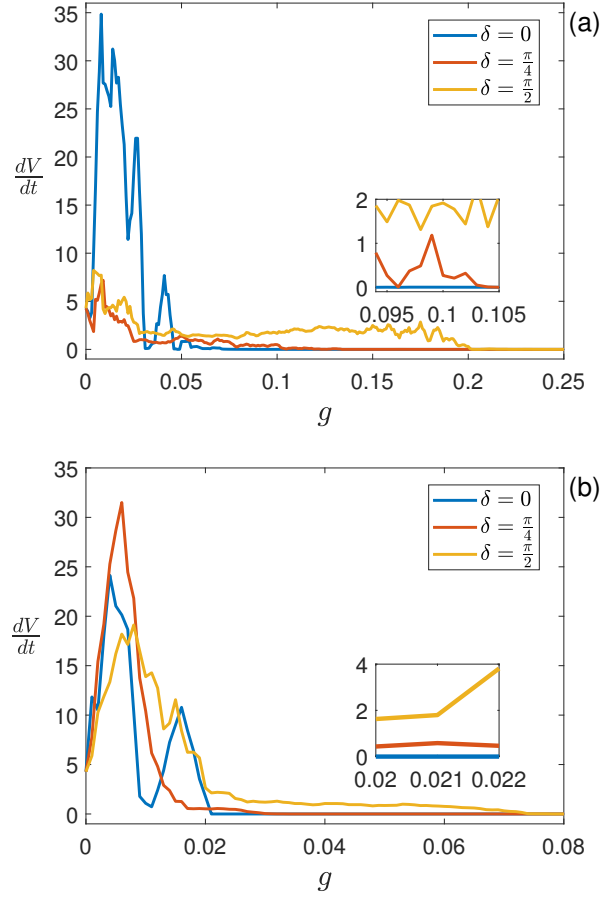


Figure 4.3: Variation of the derivative of Lyapunov function with coupling strengths for different values of δ . (a) $b_{33} = 0$, (b) $b_{33} = 1$.

(4.7), simultaneously. Similarly, the Lyapunov function for the system with self coupling in z variable is obtained as:

$$\begin{aligned} \frac{dV}{dt} = & (-0.25a(e_x^2 + 3U^2) + bU - 2g \cos \delta)e_x^2 - (1 + 2g \\ & \cos \delta)e_y^2 - (r + 2g)e_z^2 + (1 - dU)e_x e_y + (rs - 1)e_x e_z \end{aligned} \quad (4.11)$$

The stability of the synchrony in the system by varying coupling phases given in Eq. (4.2) is analysed with $b_{33} = 0$ and $b_{33} = 1$ using Eqs. (4.10) and (4.11), respectively. The variation of $\frac{dV}{dt}$ with g and $b_{33} = 0$ is presented in fig. 4.3(a). The value of $\frac{dV}{dt}$ is greater than 0 for $g < 0.06$ in the system with self coupling in x and y ($\delta = 0$), represented by the blue line. The system exhibits desynchrony

in this region. For $g > 0.06$, the system is synchronised with $\frac{dV}{dt} = 0$. For the system with mixed coupling ($\delta = \frac{\pi}{4}$), the synchrony is obtained at a higher value of $g = 0.12$, represented by the red line. The complete synchrony in the system with cross coupling ($\delta = \frac{\pi}{2}$) is obtained at $g = 0.2$. The inset shows that synchrony is more difficult to achieve in systems with mixed coupling than in systems with self coupling. The variation of $\frac{dV}{dt}$ for the system with self coupling in z variable ($b_{33} = 1$) along with cross coupling in x and y is analysed using Eq. (4.11) and is presented in fig. 4.3(b). In contrast to a system lacking self coupling in z , synchrony stabilisation occurs at lower values of g . The synchrony is attained at $g = 0.02, 0.03, 0.07$ for self, mixed and cross couplings, respectively. In the inset, it is justified that in mixed coupled systems the coupling strength at which synchrony is obtained is greater than self coupled systems. When $\delta = \frac{\pi}{2}$, the interaction is cross alone and the synchrony is obtained at high coupling strength compared to the system with self and mixed coupling. The system with self coupling attains synchrony at a lower coupling strength compared to the system with sole cross coupling.

The parameter space shown in fig. 4.4 explains the complete synchronisation scenario by varying g and δ , for $b_{33} = 0$ and $b_{33} = 1$, at low and high coupling strengths. When there is self coupling in y and z variable, the synchrony is highly sensitive to the coupling strength, g , when compared to the system with self coupling in x alone, as shown in fig. 4.2. The variation of the time derivative of the Lyapunov function with $b_{33} = 0$ for low and high values of g is presented in figs. 4.4(a) and 4.4(b), respectively. For values near $\delta = 0$, the system has self interactions and synchrony is obtained at $g \approx 0.05$, which is visible from fig. 4.4(a). With the increase in the value of δ , the coupling strength at which the stabilised synchrony is obtained increases due to the contributions from cross coupling. On further increase in the value of δ , the interaction from self coupling decreases and cross coupling increases and the synchrony is obtained at a higher value of g . When $\delta = \frac{\pi}{2}$, the interaction is cross coupling alone and the synchrony is obtained at $g \approx 0.2$, which is observed from fig. 4.4(b).

The synchronisation scenario of the system with $b_{33} = 1$ as shown in fig.

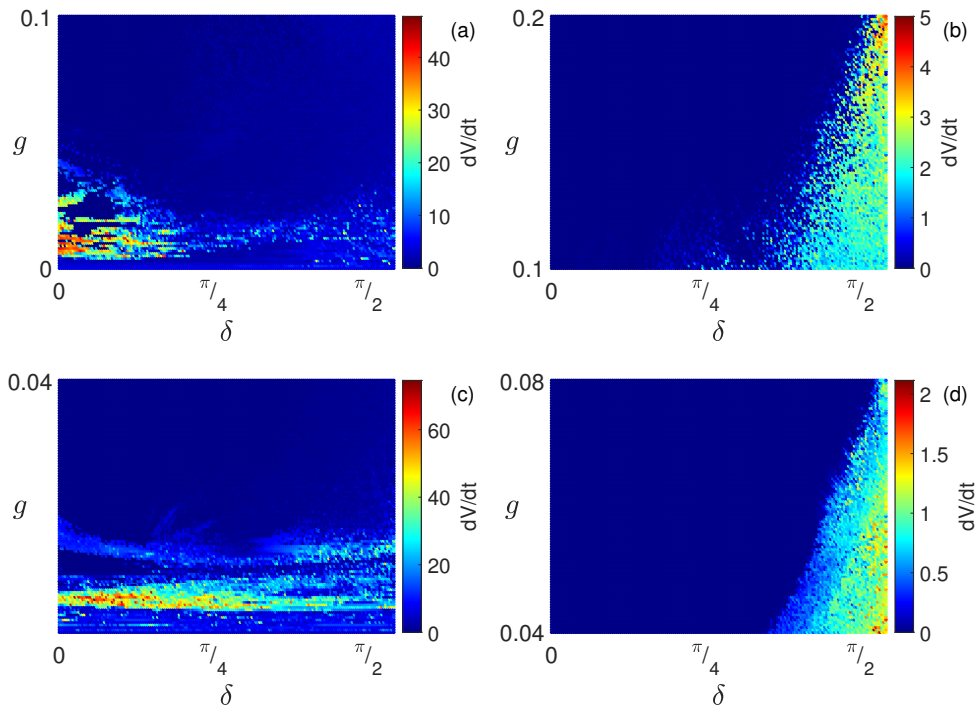


Figure 4.4: Colour coded variation of the time derivative of the Lyapunov function with coupling strength and phase. Coupling phase is plotted along the X-axis, coupling strength along the Y-axis and the derivative of the Lyapunov function is represented by colourbar. (a) $b_{33} = 0$ (low coupling strength), (b) $b_{33} = 0$ (high coupling strength), (c) $b_{33} = 1$ (low coupling strength), (d) $b_{33} = 1$ (high coupling strength).

4.4(c) and 4.4(d). For low values of δ , the interaction is self coupling and the synchrony is obtained at $g \approx 0.02$, as shown in fig. 4.4(c). With the increase in δ , cross coupling works along with self coupling and the value at which synchrony is obtained increases to $g \approx 0.03$. With further increase in δ , interactions are solely from cross coupling and the value of g at which synchrony obtained increases, as visible from fig. 4.4(d). The coupling strength at which system attains synchrony is the lowest when there is self coupling in all the three variables. The parameter space is rich and complex due to the coupling scheme of the network and it remains consistent for any values of initial conditions.

4.3 Global, nonlocal and local interactions

A network of HR neurons with interactions represented by a rotation matrix, with global, nonlocal and local (nearest neighbour) interactions has been analysed in ring topology.

The dynamical equations are of the form:

$$\begin{aligned}
\dot{x}_i &= y_i + ax_i^2 - bx_i^3 - z_i + I + \frac{g}{2p} \sum_{j=i-p}^{j=i+p} [b_{11}(x_j - x_i) + b_{12}(y_j - y_i) + b_{13}(z_j - z_i)], \\
\dot{y}_i &= c - dx_i^2 - y_i + \frac{g}{2p} \sum_{j=i-p}^{j=i+p} [b_{21}(x_j - x_i) + b_{22}(y_j - y_i) + b_{23}(z_j - z_i)], \\
\dot{z}_i &= r(s(x_i - x_e) - z_i) + \frac{g}{2p} \sum_{j=i-p}^{j=i+p} [b_{31}(x_j - x_i) + b_{32}(y_j - y_i) + b_{33}(z_j - z_i)].
\end{aligned}
\tag{4.12}$$

Where i runs from 1 to N , N being the total number of neurons in the network. A periodic boundary condition $x_0 = x_N$, $x_{-1} = x_{N-1}$ and $x_{N+1} = x_1$ is considered to realise the ring configuration. p is the number of neighbours to which each neuron is coupled in either direction of the ring. The network is analysed with $N = 525$. The global, nonlocal and local interactions are realised by fixing $p = \frac{N-1}{2}$, 10 and 1, respectively. The synchrony pattern in the net-

work with global interaction for different coupling phases is quantified using the statistical factor of synchronisation, R , given by Eq. (1.3).

The variation of R with g , for different values of coupling phases is shown in fig. 4.5. The synchrony in the network with self coupling is presented in fig. 4.5(a). The synchrony attained in the system with self coupling in x variable alone is presented by blue line. The red and yellow lines represent the synchrony pattern with self coupling in x, y and x, y, z variables, respectively. With increase in number of variables having self coupling, the coupling strength at which synchrony is obtained decreases. The synchrony obtained in the system with cross coupling in x and y variable and no self coupling in z variables ($b_{33} = 0$) is shown in fig. 4.5(b). For $g \approx 0.4$, the system attains complete synchrony for mixed coupling ($\delta = \frac{\pi}{4}$), whereas for cross coupling the complete synchrony is obtained for $g \approx 0.7$. For values above 0.7, the synchrony for mixed and cross coupling coincides with each other. The amount of synchrony obtained with cross coupling in x and y variable and self coupling in z variable ($b_{33} = 1$) is shown in fig. 4.5(c). In comparison to the system with no self coupling in the z variable, the synchronisation is attained at a lower coupling strength. The system attains complete synchrony at $g = 0.1$ and 0.7 for mixed and cross coupling, respectively. The coupling strength at which synchrony is achieved for N coupled neurons, however, is higher than a system with two neurons.

4.3.1 Emergence of chimera, MOS and clusters

The network with $b_{33} = 1$ shows a richer pattern and cluster formations in non-local and local interactions and is shown in fig. 4.6. The multichimera pattern obtained for nonlocal interaction in system with self coupling in x, y and z variables, for $\delta = 0$, is shown in fig. 4.6(a). The self coupling in more than one state variable is capable of inducing chimera states. The same is not obtained when the coupling is for a single variable. This proves that a network is self sufficient of exhibiting chimeras without distance-dependent coupling or cross coupling, under the influence of self coupling in more than one variable. The mixed coupling in x and y variables and self coupling in z variable, for $\delta = \frac{\pi}{4}$, induces chimera

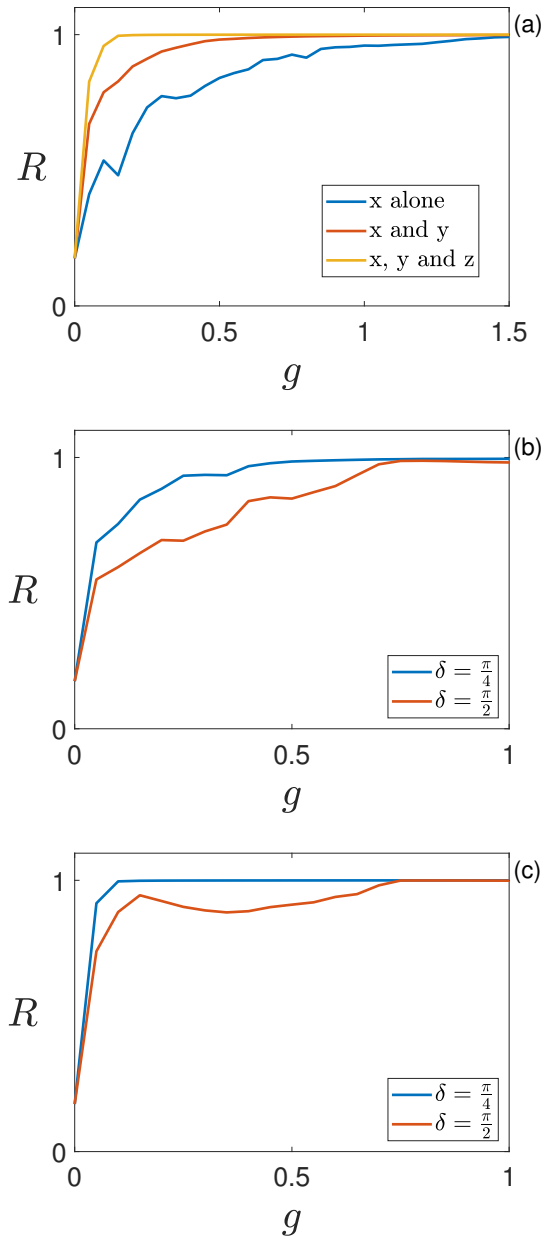


Figure 4.5: Variation of the statistical factor of synchronisation with coupling strength in the HR neural network with global interaction for different values of coupling phase. (a) Self coupling in variables, (b) $b_{33} = 0$, (c) $b_{33} = 1$.

state as shown in fig. 4.6(b). Travelling chimera is obtained for mixed coupling with $\delta = \frac{\pi}{2} - 1$ for $g = 0.09$ and 0.1 , as shown in fig. 4.6(c) and 4.6(d), respectively. Multichimera states are obtained for $\delta = \frac{\pi}{2}$, at $g = 0.17, 0.24$, as shown in figs. 4.6(e) and 4.6(f), respectively. The inhibitor self coupling with $\delta = -\pi$ in nearest neighbour interaction induces mixed oscillatory state, as shown in fig. 4.6(g). In MOS, almost half of the neurons are desynchronised, which are uniformly distributed within the other half that exhibit perfect synchronisation. The synchronised subpopulation shows amplitude death and the desynchronised subpopulation possess spiking character. The corresponding spatiotemporal pattern is shown in fig. 4.6(h). The inset shows the enlarged view of the neurons 1 to 20 for the time range 980 to 1000. The dotted lines present the spiking character and the dark blue solid lines represent the amplitude death states. The oscillators are grouped in to three clusters for locally coupled network, with $\delta = -\pi$ as shown in fig. 4.6(i). The dynamics is amplitude death as shown by the solid lines in fig. 4.6(j). The inset shows the enlarged view of the amplitude death state.

4.3.2 Strength of incoherence and discontinuity measure

The emergence of chimera and multichimera states in the network with self, cross and mixed coupling of state variables is analysed with the help of a quantitative measure called strength of incoherence (SI), given by Eq. (1.13). In order to distinguish chimera from multichimera states, we calculate discontinuity measure (DM), using the formula represented by the Eq. (1.14).

The self coupling in three variables x, y and z induces chimera states in non-locally coupled network as shown in fig. 4.7(a). The fig. 4.7(b) justifies the presence of chimera states. The emergence of chimera or multichimera in non-locally coupled network with mixed coupling in x, y and self coupling in z is shown in fig. 4.7(c). The variation of DM as shown in fig. 4.7(d) distinguishes the chimera and multichimera states. The cross coupling in x and y , along with the self coupling in z variable also induces chimera and multichimera states in the nonlocally coupled network which is visible from fig. 4.7(e). The fig. 4.7(f)

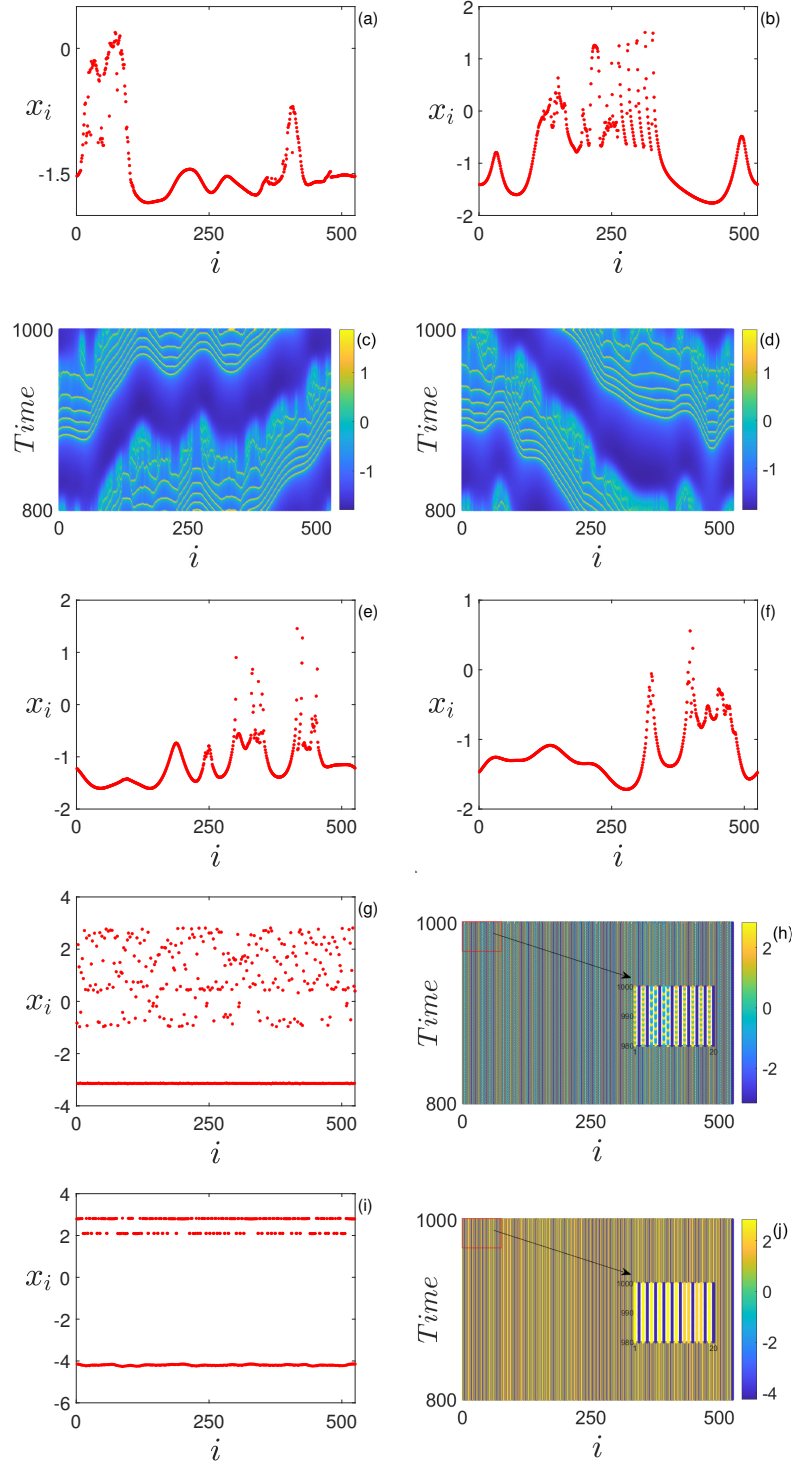


Figure 4.6: Emergence of interesting patterns in the HR network by the variation of coupling phase in nonlocal and local interactions. (a) multichimera ($p = 10, \delta = 0, g = 0.1$) (b) chimera ($p = 10, \delta = \frac{\pi}{4}, g = 0.19$) (c) travelling chimera ($p = 10, \delta = \frac{\pi}{2} - 1, g = 0.09$) (d) travelling chimera ($p = 10, \delta = \frac{\pi}{2} - 1, g = 0.1$) (e) multichimera ($p = 10, \delta = \frac{\pi}{2}, g = 0.17$) (f) multichimera ($p = 10, \delta = \frac{\pi}{2}, g = 0.24$) (g) MOS ($p = 1, \delta = -\pi, g = 0.2$) (h) cluster ($p = 1, \delta = -\pi, g = 0.3$). The colourbar represents the membrane potential, x .

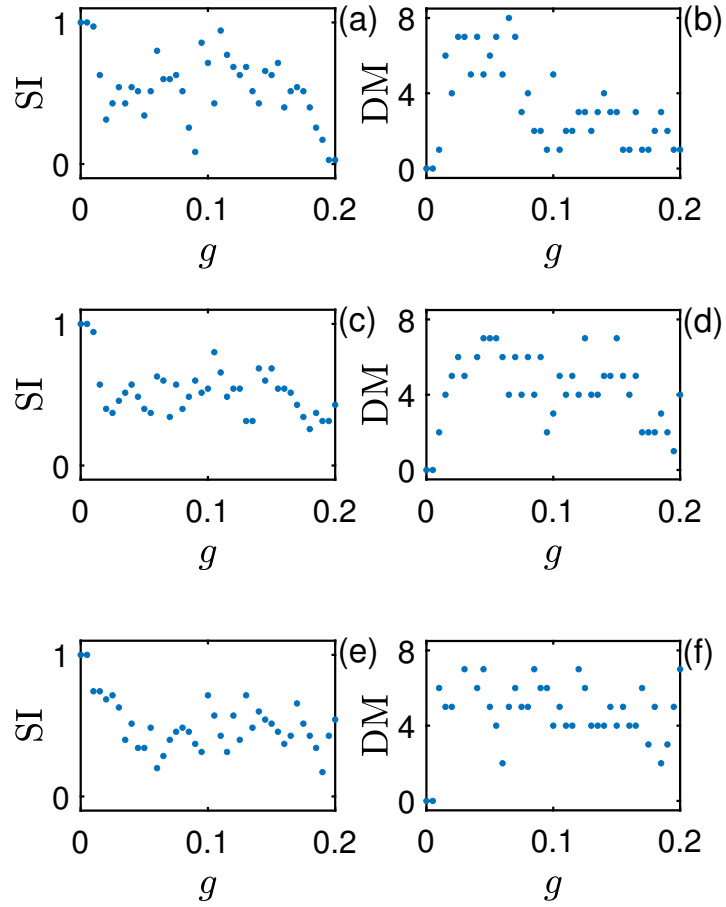


Figure 4.7: Strength of incoherence (SI) and discontinuity measure (DM) for different coupling phases in nonlocal interactions. The left panel shows the values of SI. (a) $\delta = 0$, (c) $\delta = \frac{\pi}{4}$, (e) $\delta = \frac{\pi}{2}$. The right panel shows the variation of DM for the corresponding values of left panel. Here, $M = 35$, $\epsilon = 0.04$, $p = 10$.

shows that there are no chimeras and that the patterns obtained are multichimeras. The studies have shown that under the influence of rotation matrix, chimera states are induced in the nonlocally coupled network with self, mixed and cross interaction and in locally coupled network, neurons show clusterisation. In mixed and cross interactions, the possibilities of obtaining multichimera states are high. In self coupled network, chimera and multichimera states are obtained.

4.4 Results and conclusions

The synchronisation and patterns emerging due to the self and cross interactions of variables are analysed in the network of HR neurons. The activator self coupling in the x variable induces in-phase synchrony whereas the inhibitory mode induces anti-phase oscillations in two coupled systems. When the self coupling in y and z variables are introduced synchrony is attained at a lower coupling strength. Based on the Lyapunov function approach, the stability of activator coupling in x variable is verified for self, mixed and cross coupling modes. When the system achieves synchrony, the time derivative of the function tends to zero. The synchronisation scenario is explained in detail by the parameter space with coupling phase and coupling strength, as the parameters. The complete synchronisation is achieved at a lower coupling strength when self coupling is present in the variables and as cross interactions come into play, synchronisation is achieved at a higher coupling strength.

The network arranged in ring topology has been analysed with global, non-local and local interactions. The in-phase synchrony obtained for activator coupling in x variable with self, mixed or cross coupling has been justified in the globally coupled systems as well. In electrical coupling, the coupling strength at which synchrony is obtained depends on the network size. Interesting patterns like chimera, multichimera and travelling chimera are obtained by the interplay of coupling phase and coupling strength, in nonlocal interactions. The study shows that in networks with self interactions, chimera and multichimera states

are obtained, whereas mixed and cross interactions induce multichimera states. The inhibitor self coupling in x, y and activator self coupling in z variable induces in-phase, anti-phase and out of phase oscillations which result in the occurrence of mixed oscillatory state and clusters in nearest neighbour interactions.

The observed in-phase and anti-phase oscillations might be an indicator of the presence of distinct frequency rhythms and oscillatory patterns in separate regions of extended neural networks. The findings of this work reveal the dynamic processes that cause the coupled neurons to exhibit in-phase and anti-phase oscillations, which is useful for understanding how synapses regulate the rhythms of the brain activity.

Chapter 5

Collective behaviour of magnetically coupled HR network

5.1 Introduction

The use of memristors to represent the electromagnetic field induced by the flow of ions in the neurons was proposed recently [162] and continues to attract researchers [163–166]. The dynamics and energy aspects of HR neurons with quadratic and cubic memristor effects have been analysed [87, 158, 167]. The impact of electromagnetic field on individual and collective dynamics of the neural system has been studied recently [168]. The utilisation of energy for the electrical activities in the presence of magnetic coupling and external stimuli have been studied on the Hodgkin-Huxley model [169]. The memory conductance in the form of hyperbolic tangent function was recognised as being easily implementable in electronic circuits and effective in numerical simulations [170, 171].

The diverse firing patterns and synchronous oscillations are crucial features in neural dynamics of the brains. Both external and inherent stimuli constructively take part in the excitation of neural activity [172]. Zhijun Li, *et al.* investigated the coexistence of multiple firing patterns for different initial conditions with coupling strength as the only control parameter [173]. Different methods have been employed to enhance the synchrony in the neural network owing to its vital

role in signal transmission and processing [174, 175]. However, the unwanted synchrony among neurons which ought to have behaved independently, results in several pathological conditions [47, 176, 177]. Thus, the enhancement and suppression of this synchrony are very necessary [178]. Recently, researchers investigated the phase synchrony of mean field coupled HR neurons with external stimuli in the form of spikes [105]. The external stimuli have the capability of controlling chaotic dynamics in the neural network [179, 180]. However, the influence of square input on neural network is unexplored.

The coupling function always plays an important role in the studies on chimera and it was believed that nonlocal coupling was essential to induce chimera states. But, later, it was found that global coupling and even local coupling (diffusive, to nearest neighbours) also supported chimera states [117, 181]. The existence of chimera and multichimera states has been observed in the locally coupled HR neuron model [64]. The chimera states have also been reported in ephaptically coupled HR ring network [104]. The synchronisation as well as the existence of chimera states have been studied in multilayer networks of neurons under distance-dependent coupling following a power law model [37, 118, 182]. Basic forces such as electrostatic and gravitational forces exhibit interactions that are controlled by a power law exponent [183]. The analysis of synchronisation properties of neural networks under distance-dependent coupling governed by the power law model is a newly emerging field of interest [37, 127].

In this chapter, the dynamics and synchronisation properties of a network of HR neurons, arranged in a linear chain structure with distance-dependent field coupling are analysed. This chapter is organised as follows: The model for the network with distance-dependent memristor coupling in the presence of external stimuli is described in section 5.2. The phase portraits and collective dynamics of the network under the influence of constant current are explained in section 5.2.1. The control of phase space trajectories and synchrony by the combined effect of magnetic coupling and time varying external currents are presented in section 5.2.2. Section 5.2.3 has been devoted to quantifying synchrony in the network with magnetic coupling and external stimuli. The network model with

the combined effect of distance-dependent memristor and mean field coupling is explained in section 5.3. The statistical factor of synchronisation, spatiotemporal dynamics and pattern formations in distance-dependent memristive HR neurons with uniform mean field coupling are analysed in section 5.3.1. The variation of the synchrony pattern and the emergence of chimera states under the influence of memristor and mean field coupling with distance dependence, governed by power law, are studied in section 5.3.2. The results are presented in section 5.4.

5.2 Controlling synchrony using external stimuli

The electromagnetic fields and externally applied stimuli are capable of altering collective electrical activities and signal propagation in a neural network. The current, induced by the change in magnetic flux across the membrane, is represented by the memristor and that, due to the external stimuli is considered under three cases. The dynamical equations for a linear chain of HR neurons are described by [21, 22]:

$$\begin{aligned}
\dot{x}_i &= y_i + ax_i^2 - bx_i^3 - z_i + I - k_1\rho(\phi_i)x_i, \\
\dot{y}_i &= c - dx_i^2 - y_i, \\
\dot{z}_i &= r(s(x_i - x_e) - z_i), \\
\dot{\phi}_i &= k_2x_i - k_3\phi_i + D\left(\phi_i - \sum_{\substack{j=1 \\ j \neq i}}^N \frac{W}{|i-j|} \phi_j\right), \quad i = 1, 2, \dots, N.
\end{aligned} \tag{5.1}$$

Where x_i , y_i and z_i represent the membrane potential, spiking variable and bursting variable of i th neuron, respectively. y_i is constituted by the flow of Na^+ and K^+ ions and the flow of Ca^+ ions constitute the z_i term. The fast oscillations of x_i and y_i correspond to spikes, whereas the slow oscillations of the z_i variable cause bursts [17]. Indices i , j and N , represent presynaptic neurons, postsynaptic neurons and total number of neurons in the network, respectively. The external current, I , is considered as a constant and two varying forms.

The interaction between membrane potential, x_i and magnetic flux, ϕ_i , is realised with the help of memristor, $k_1\rho(\phi_i)x_i$, where, k_1 is the magnetic coupling strength. We have considered the memory conductance term, $\rho(\phi_i)$ as a hyperbolic form, $\tanh(\phi_i)$ [170]. This function can be easily approximated by a linear form. The change in magnetic flux induced by membrane potential is given by k_2x_i and the leakage of the magnetic flux is represented by $k_3\phi_i$. D describes the field interaction between neurons. W represents the intensity of the field effect associated with distance between neurons. The parameters of the model are fixed as, $a = 3.0$, $b = 1.0$, $c = 1$, $d = 5$, $r = 0.006$, $s = 4.0$, $x_e = -1.61$ [18], $k_2 = 0.9$, $k_3 = 0.4$, $D = 0.0001$, $W = 1$ [167].

Collective dynamics and synchronisation scenario

The changes in the firing pattern, phase portraits and synchrony level, under the combined effect of magnetic coupling and external stimulus have been analysed. We have chosen the external stimuli in different forms (i) a constant (I_1) and (ii) as time varying function. The time varying external inputs are considered in two different forms: (a) sinusoidal wave, given as $I_2 = A(\sin(\omega t) + \cos(\omega t))$ with frequency, ω and (b) square wave, represented as $I_3 = A\mathcal{H}\left(\sin\left(\frac{2\pi t}{\rho_s}\right)\right)$, with an interval, ρ_s . \mathcal{H} is the bi-valued Heaviside step function, whose value is zero for negative arguments and one for positive arguments.

5.2.1 Constant external current

In this section, the dynamics, phase portraits and synchrony pattern have been analysed under the memristor effect and constant external current. The dynamics and collective behaviour of the network are analysed numerically by solving Eq. (5.1) for $x_i(t)$, $y_i(t)$, $z_i(t)$ and $\phi_i(t)$ using the Runge-kutta method in step size of 0.1. Initial conditions for different neurons are chosen as, $x_0(t)$, $y_0(t)$ and $z_0(t)$ in the range [-0.5,0.5] and $\phi_0(t)$ in the range [0,1]. The study of variation of x_i reveals the dynamical change induced in each neuron under the influence of magnetic coupling and external stimuli. The average of x_i over the number

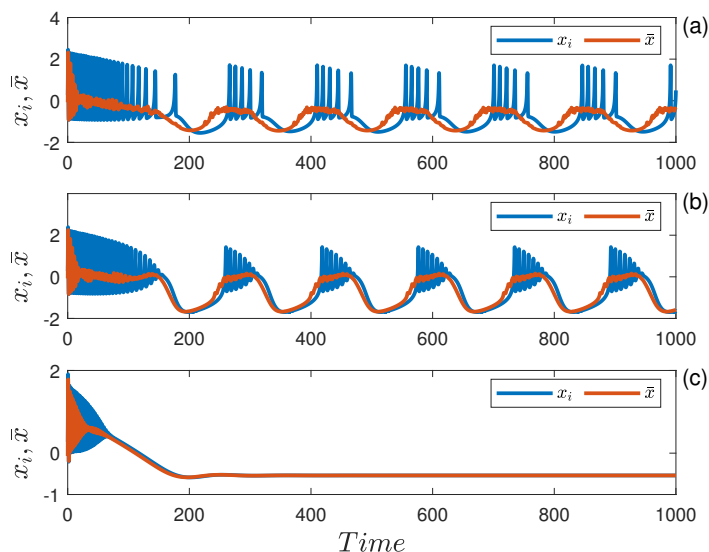


Figure 5.1: Time series of the discrete and average membrane potentials of the magnetically coupled neural network with constant external current ($I = 2.9$). Here, $i = 25$ and the dynamics is consistent for any neuron in the network. (a) $k_1 = 0.1$, (b) $k_1 = 0.3$ and (c) $k_1 = 1.5$.

of neurons in the network reveals the collective behaviour of the network. The average of membrane potentials is given by

$$\bar{x}(t) = \frac{1}{N} \sum_{i=1}^N x_i(t) \quad (5.2)$$

The dynamical change induced in a single neuron and the collective synchrony is analysed in the memristive network for different values of k_1 in the presence of constant external current ($I_1 = 2.9$) and is as shown in fig. 5.1.

For low values of k_1 , the system exhibits square wave bursting with five spikes per burst, as shown in fig. 5.1(a). The lack of synchrony is visible from difference of \bar{x} from the individual membrane potential. We have validated the presence of plateau bursting dynamics with an increase in the value of k_1 , as shown in fig. 5.1(b). The dissimilarity in average membrane potential from the individual values represents the absence of synchrony. On further increasing the value of k_1 , fig. 5.1(c) shows AD state with no oscillations. From the studies, it is clear that magnetic coupling stabilises the system. The system is in complete synchrony, as visible from the convergence of \bar{x} with the individual values. The memristor drives the system from square wave bursting to plateau bursting and to AD state,

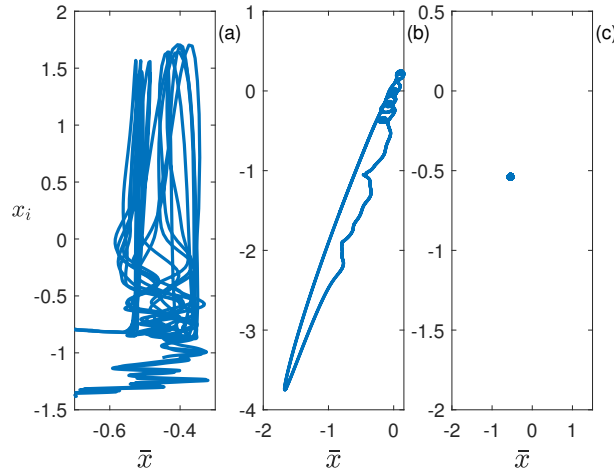


Figure 5.2: Phase portraits of the neural network with magnetic coupling and constant external current ($I = 2.9$). The average membrane potential is plotted on the X-axis and the membrane potential of a single neuron on the Y-axis. Here, $i = 25$. (a) $k_1 = 0.1$, (b) $k_1 = 0.3$ and (c) $k_1 = 1.5$.

where the system exhibits complete synchrony.

The synchrony pattern in the network is further justified by the phase portraits as shown in fig 5.2. The phase space has been plotted with average membrane potential $\bar{x}(t)$ on the X-axis and the membrane potential of a single neuron on the Y-axis. In fig. 5.2(a), the phase space is dense at $k_1 = 0.1$, representing a lack of synchrony. As the value of k_1 is increased, the phase space becomes more controlled and synchronised, as shown in fig. 5.2(b). The phase space shrinks to a single point representing stabilisation of the states, on further increase in k_1 , as in fig. 5.2(c). The increase in magnetic enhancement of synchrony with the strength of magnetic coupling is visible from the controlling and shrinking of phase plots.

5.2.2 Time varying external currents

The variation of firing patterns and the collective dynamics of the network with magnetic coupling under the influence of time varying external stimuli is analysed in this section. The time series of $\bar{x}(t)$ for the two different external stimulus is shown in fig. 5.3. In the presence of memristor and sinusoidal wave, the system exhibits square wave bursting character, as shown in fig. 5.3(a), for low value

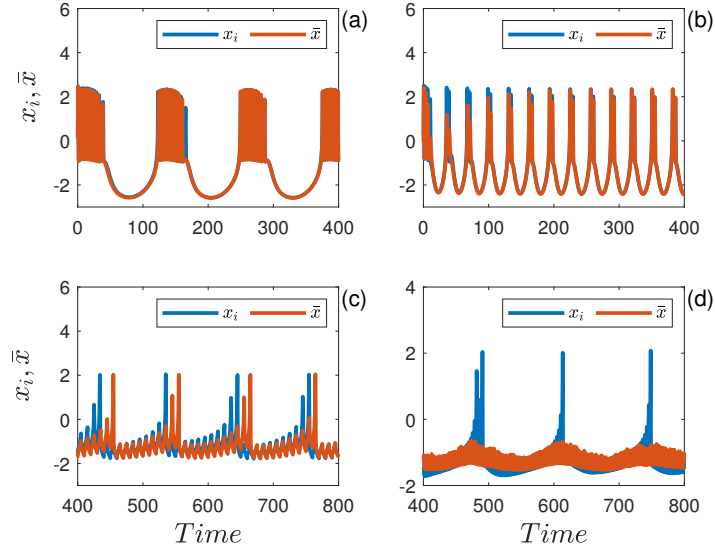


Figure 5.3: Time series of the discrete and average membrane potentials of the magnetically coupled neural network with time varying external stimuli. Here $i = 25$, $k_1 = 0.1$. (a) sinusoidal input ($A = 3$, $\omega = 0.05$), (b) sinusoidal input ($A = 3$, $\omega = 0.2$), (c) square input ($A = 3$, $\rho_s = 10$) and (d) square input ($A = 3$, $\rho_s = 3$).

of input frequency, ω . The initial transients lack complete synchrony, whereas, with evolution of time, the system attains synchrony. This is visible as the convergence of individual and average values of the membrane potential. With an increase in frequency, ω , the number of spikes per burst decreases to two, as shown in fig. 5.3(b). But the synchrony pattern is maintained. Fig. 5.3(c) shows the spiking behaviour under the influence of memristor and square wave. The spikes are induced in the quiescent state. The lack of synchrony is visible from the figure by the separation of individual membrane potential from the average value. With decrease in interval of the square input, the synchrony level is even reduced, which is visible from fig. 5.3(d).

The phase portraits of the system with magnetic coupling and the time varying external stimulus are as shown in fig. 5.4. The top and bottom panels show the phase spaces of the system with sinusoidal and square inputs, respectively. In both panels, the value of k_1 increases from left to right. The fig. 5.4(a) presents the influence of input I_2 on a network with weak magnetic coupling. The phase space exhibits a small dispersion. On increasing the strength of magnetic coupling, k_1 , the phase space is reduced to a beeline as shown in fig 5.4(b). On

further increase of k_1 , the synchrony in the network is preserved by the combined effect of magnetic coupling and sinusoidal input, (I_2), observed as the straight line in phase portrait of fig 5.4(c). The synchrony attained is sustained at an even higher value of magnetic coupling strength, as shown in fig 5.4(d). The dispersed phase portrait for low magnetic coupling strength under the influence of square input, I_3 , represents the lack of synchrony in the network, as shown in fig 5.4(e).

With further increase in magnetic coupling, the phase portrait is still dispersed in the presence of square input, as shown in fig 5.4(f). A slight control in the phase portrait is visible for further increases in magnetic coupling strength, as shown in fig 5.4(g). At high values of magnetic coupling strength, the phase portrait is reduced to a beeline in the presence of input, I_3 , as shown in fig 5.4(h). Thus, it is found that the magnetic coupling helps to control the phase space in the presence of time varying external inputs. However, the control is faster in the presence of sinusoidal input compared to the square input.

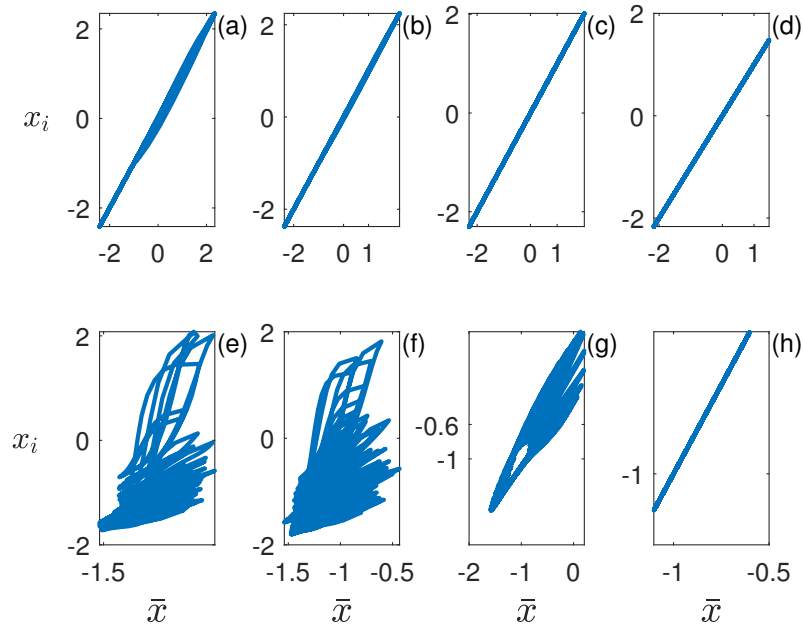


Figure 5.4: Phase space with sinusoidal (top panel) and square input (bottom panel). Here, $i = 25$, $A = 3$, $\omega = 0.2$, $\rho_s = 3$. The values are fixed as (a), (e) $k_1 = 0.1$, (b), (f) $k_1 = 0.3$, (c), (g) $k_1 = 0.7$ and (d), (h) $k_1 = 1.5$.

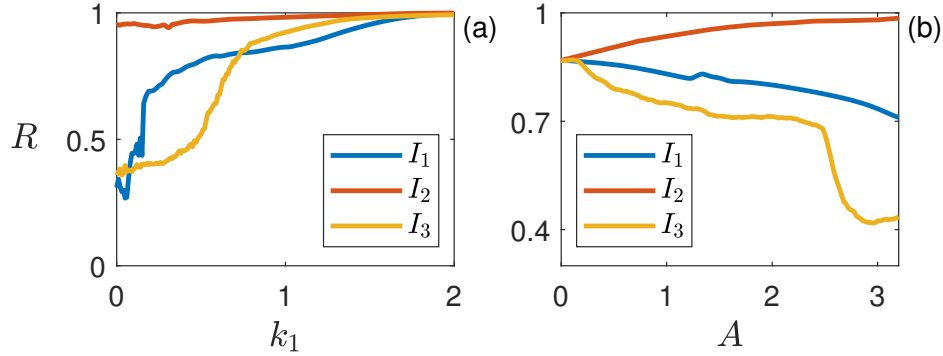


Figure 5.5: Variation of the statistical factor of synchronisation with (a) magnetic coupling strength and (b) amplitude of external input, under the influence of different external stimuli. The constant input, sinusoidal and square inputs are represented by the blue, red and yellow lines respectively. (a) $A = 3$ (b) $k_1 = 0.3$. Here, $\omega = 0.2$, $\rho_s = 3$.

5.2.3 Quantifying synchrony

The synchrony induced by the magnetic coupling, in the presence of external stimuli is quantified using statistical factor of synchronisation, R , given by the Eqn. (1.3).

The variation of R with k_1 in the presence of different external stimuli is shown in fig. 5.5(a). The statistical factor of synchronisation has been calculated using Eqn. (1.3). The blue, red and yellow lines represent the influence of constant, sinusoidal and square input on the magnetically coupled network, respectively. The amplitude of the inputs is fixed at $A = 3$. At low values of k_1 , the value of R is about 0.5, representing partial synchrony. The synchrony obtained by the network, under the influence of a constant current is found to be high compared to the square input. The high value of R obtained for even low value of magnetic coupling in the presence of sinusoidal input represents the synchrony obtained by the network. For weakly coupled system, the synchrony obtained by the constant input lies in between square and sinusoidal input and for high values of k_1 , the magnetic coupling overrides the input effects.

The variation of R with the amplitude of the inputs is presented in fig. 5.5(b).

The colour codes used for the inputs are similar to fig. 5.5(a). In the absence of any external input, the synchrony level is obtained to be about $R = 0.85$, as the value of k_1 is fixed as 0.3. For low intensities of the inputs, the synchrony of the network is reduced from its initial value in the presence of constant input. The synchrony is even low under the influence of square input. The presence of sinusoidal input increases the synchrony in the network. With increase in the intensities of the inputs, the differences in synchrony become more visible. The results obtained are in perfect agreement with the studies of fig. 5.5(a). At sufficiently high amplitudes of the external input, the sinusoidal input is capable of enhancing synchrony compared to the constant input. The desynchronising ability of the square input on the magnetically coupled network is also visible.

The study of synchrony pattern has been extended by varying frequencies of the inputs, I_2 and I_3 . The variation of R with the frequency, ω of sinusoidal input is shown in fig. 5.6(a). For low value of frequency, the synchrony is quantified to be about $R = 0.7$. With further increase in ω the synchrony also increased. Thus the input with high frequency has a greater synchronising ability. The desynchronising ability of the square input is analysed for the variations in the interval of the square input as presented in fig. 5.6(b). For low values of the interval, ρ , (*i.e.*,) high frequency, the synchrony is drastically reduced. But on further increasing the interval (reducing frequency), the synchrony is increasing, representing the inability of the low frequency input to desynchronise. Thus it is inferred that high frequency sinusoidal input and square input have the capability to synchronise and desynchronise the magnetically coupled network, respectively.

5.3 Distance-dependent field couplings

The model of HR neurons with memristor and mean field coupling is modified with distance dependence governed by power law. The dynamics, synchronisation scenario and pattern formations with the neurons arranged in a linear chain

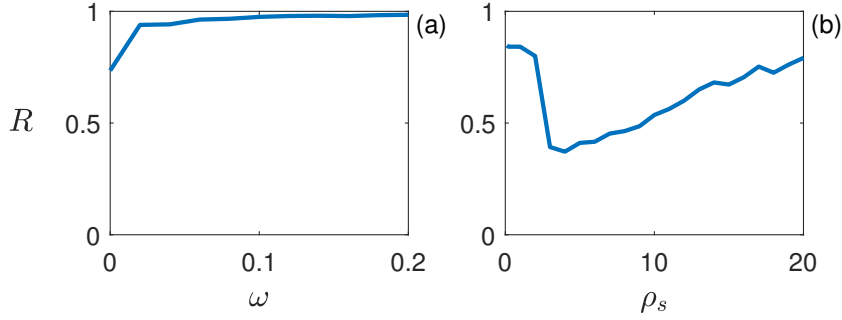


Figure 5.6: Variation of the statistical factor of synchronisation for different parameters of the time varying input. Here, $k_1 = 0.3$, $A = 3$.

structure have been analysed. The modified model has the form: [22, 184]:

$$\begin{aligned}
 \dot{x}_i &= y_i + ax_i^2 - bx_i^3 - z_i + I - k_1\rho(\phi_i) + \frac{g}{N-1} \sum_{\substack{j=1 \\ j \neq i}}^N \frac{x_j(t)}{|i-j|^\alpha}, \\
 \dot{y}_i &= c - dx_i^2 - y_i, \\
 \dot{z}_i &= r(s(x_i - x_e) - z_i), \\
 \dot{\phi}_i &= k_2x_i - k_3\phi_i + D(\phi_i - \sum_{\substack{j=1 \\ j \neq i}}^N \frac{W}{|i-j|} \phi_j), \quad i = 1, 2, \dots, N.
 \end{aligned} \tag{5.3}$$

Where x_i , y_i and z_i represent the membrane potential, spiking variable and bursting variable of i th neuron, respectively. y_i is constituted by the flow of Na^+ and K^+ ions and the flow of Ca^+ ions constitute the z_i term. The fast oscillations of x_i and y_i correspond to spikes, whereas, the slow oscillations of the z_i variable cause burst [17]. Indices i , j and N , represent presynaptic neuron, postsynaptic neuron and total number of neurons in the network, respectively. g represents the mean field coupling strength. The external current, I , controls the qualitative behaviour of the neurons. ϕ_i describes the magnetic flux across the membrane, $k_1\rho(\phi_i)x$ denotes induction current and k_1 is induction coefficient [21, 22]. The term $\rho(\phi_i)$ is the memory conductance of a magnetic flux controlled memristor, which can take different forms. We have considered a hyperbolic function, $\tanh(\phi_i)$, whose state equation can be represented by linear terms [170].

D describes the field interaction between neurons. W represents the intensity of the field effect associated with distance between neurons. In a network of mean field coupled neurons, each neuron is driven by the force, described in terms of the membrane potential of the other neurons [77, 185]. Hence, the potential, x_i , is influenced by the average of potentials, x_j , where, $j = 1, 2, 3, \dots, N; j \neq i$. The value of power law exponent α is varied to study the effect of distance gradient effect of the mean field coupling. When $\alpha = 0$, the interaction is uniform and global. As the value of α increased, the interaction is transformed to global coupling with a distance gradient effect. On further increasing the value of α , the interaction becomes nonlocal with distance gradient effect.

5.3.1 Uniform global interaction

A network of memristive HR neurons with mean field coupling represented by Eq. (5.3) has been analysed with $\alpha = 0$, *i.e.*, uniform global coupling. The spatiotemporal dynamics, statistical factor of synchronisation and pattern formation have been studied by varying k_1 and g . The parameters chosen are: $a = 3$, $b = 1$, $c = 1$, $d = 5$, $r = 0.006$, $s = 4$, $x_e = -1.61$, $I = 3.1$ [18], $k_2 = 0.9$, $k_3 = 0.5$ [21]. The Eq. (5.3) is solved for x , y and z . Initially, the neurons are at a negative resting potential. As time evolves, in the presence of external current, the oscillations in the x variable vary between positive and negative values. The dynamical state of a neuron, characterised by discrete groups of repeated spikes is called bursting. Each burst is followed by a quiescent period after which next burst occurs. The dynamical change induced in the network with the interplay of memristor and mean field effects are shown in fig. 5.7. The memristive effect is characterised by plateau bursting, as shown in fig. 5.7(a). The square wave bursting induced by the mean field coupling in memristive neurons is shown in fig. 5.7(b). For sufficient strength of memristor and mean field effects, the coexistence of plateau and square wave bursting is observed, as shown in fig. 5.7(c). For further increase in k_1 , the system exhibits AD state, where the system attains a stable state condition without oscillations.

The spatiotemporal pattern reveals the dynamical change induced in the AD

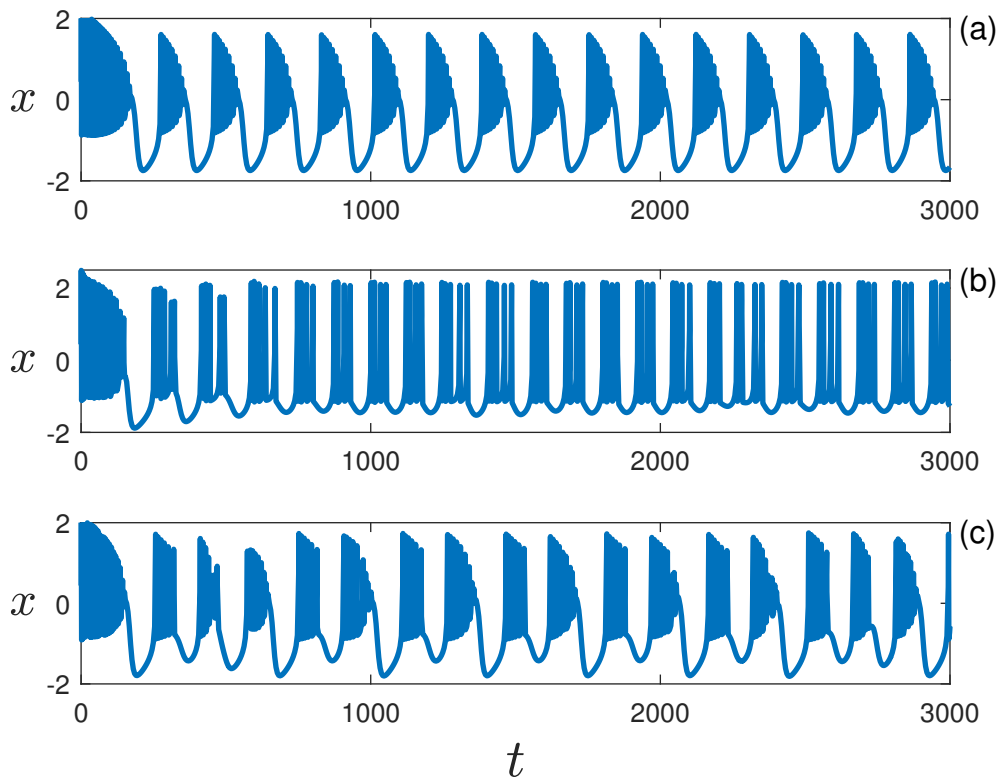


Figure 5.7: Dynamical changes induced by the interplay of memristor and mean field effects. (a) plateau bursting ($k_1 = 0.2$, $g = 0$), (b) square wave bursting ($k_1 = 0.6$, $g = 1$), (c) mixed behaviour ($k_1 = 0.8$, $g = 0.7$). This dynamic is consistent for every neuron in the network.

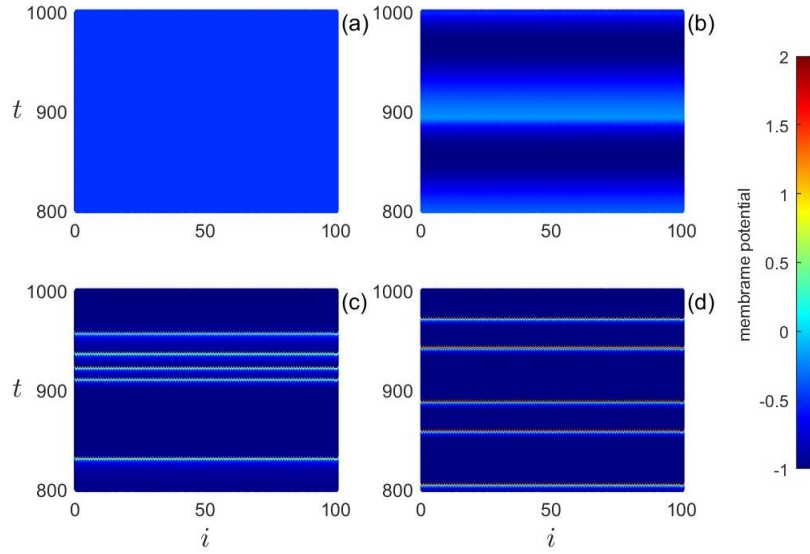


Figure 5.8: Spatiotemporal patterns of the HR neurons with memristor and mean field coupling. (a) AD ($g = 0.5$), (b) plateau bursting ($g = 1$), (c) four spikes per burst ($g = 2$), (d) two spikes per burst ($g = 2.5$). Here, $k_1 = 2$, $D = 0.0001$, $W = 1$, $N = 100$ and $\alpha = 0$. The colourbar represents the membrane potential, x .

state of memristive neurons under the influence of mean field coupling, as shown in fig. 5.8. The value of x variable is represented by the colourbar. For low values of g , every neuron in the system exhibits AD, which is visible as a single colour in fig. 5.8(a). The system shows plateau bursting at $g = 1$, as presented in fig. 5.8(b). The light and dark blue colours show spiking and quiescent period, respectively. As g increases, the dynamics change from plateau to square wave bursting. Figs. 5.8(c) and 5.8(d) show square wave bursting with 4 and 2 spikes per burst respectively. The mean field coupling initiates synchronised oscillations in the AD state of memristive neurons.

The synchronisation scenario of network with memristive and mean field coupling is studied using the statistical factor of synchronisation, R , given by Eq. (1.3).

The variation of the statistical factor of synchronisation, R , with g for different values of k_1 is shown in fig. 5.9. For $g < 1.8$, as shown in fig. 5.9(a), the synchrony increases with an increase in the value of k_1 . For a high value of k_1 , synchrony is high, with $R = 1$, even for low values of g , as represented by the purple line. Fig. 5.9(b) shows the synchronisation scenario for $g > 1.8$.

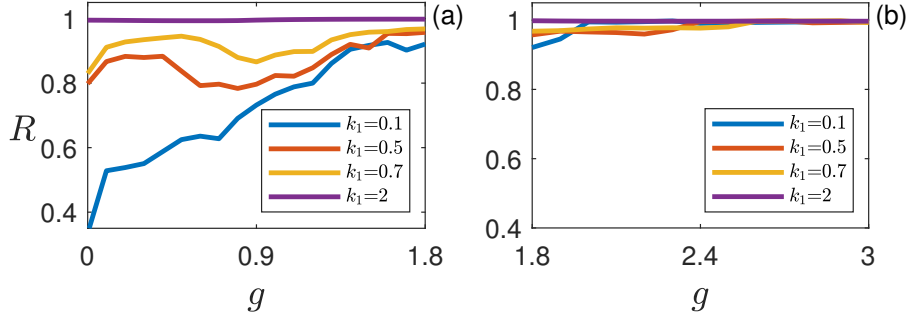


Figure 5.9: Variation of the statistical factor of synchronisation of HR neurons with the mean field coupling strength, for different values of memristor coupling strength. (a) weak coupling, (b) strong coupling. Here, $D = 0.0001$, $W = 1$, $\alpha = 0$ and $N = 100$.

The network shows high synchrony for any value of k_1 , in the presence of strong mean field coupling. It is evident that both memristor and mean field effects help mutually to attain synchrony.

The pattern formations in network with weak memristive coupling are studied for different values of g . The snapshot of x variable at $t = 1000$, is presented in the fig. 5.10. The other variables, y and z , show similar patterns. The system shows desynchrony for weak coupling, represented as scattered points in fig. 5.10(a). As g is increased, the system attains MOS, in which the desynchronised neurons are interspersed among synchronised neurons, as shown in fig. 5.10(b). The imperfect synchrony state with 5 escaping neurons, is shown in fig. 5.10(c), when $g = 1.3$. Fig. 5.10(d) represents the perfect synchrony or global death state when $g = 1.8$.

5.3.2 Emergence of chimera states

The study has been extended to the linear chain of HR neurons with distance-dependent memristor and mean field effects, governed by the power law exponent. The statistical factor of synchronisation, strength of incoherence and discontinuity measure have been studied.

The pattern of synchrony induced in the system is studied by calculating R , for various values of g and α and is shown in fig. 5.11. The influence of power law

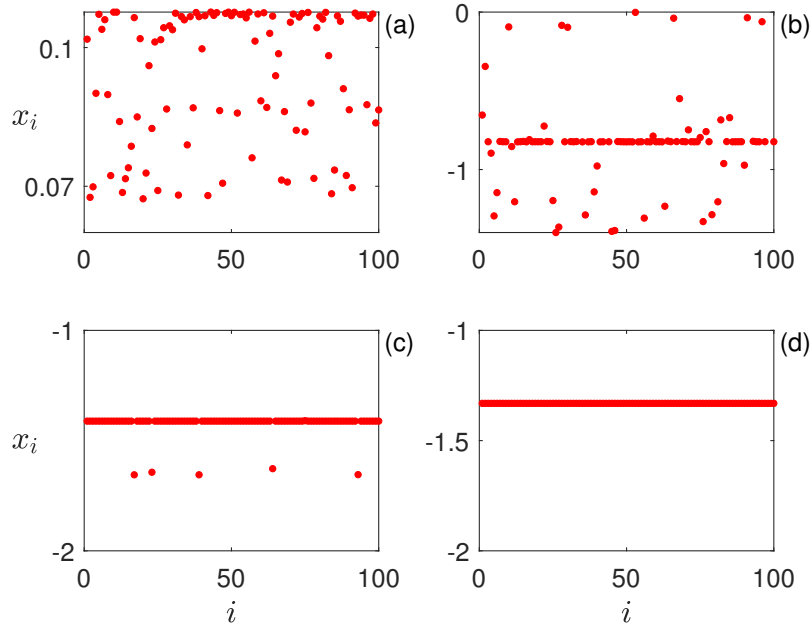


Figure 5.10: Snapshots of the HR neuron network with memristor and mean field effects. Value of $k_1 = 0.5$. (a) incoherent state ($g = 0.1$), (b) MOS ($g = 0.6$), (c) imperfect synchrony ($g = 1.3$), (d) complete synchrony ($g = 1.8$). Here, $D = 0.0001$, $W = 1$, $N = 100$ and $\alpha = 0$.

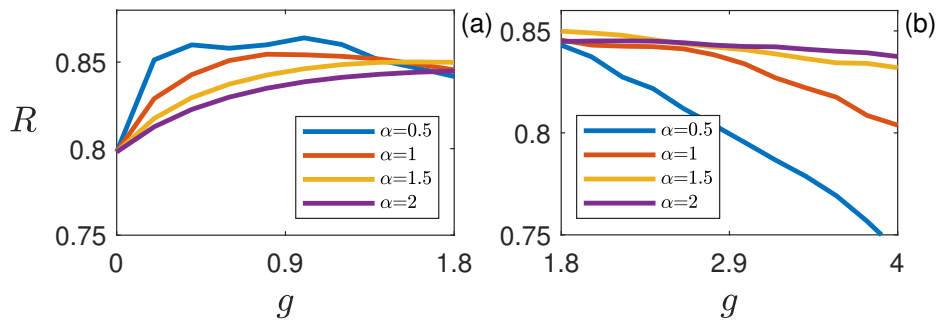


Figure 5.11: Variation of the statistical factor of synchronisation with mean field coupling, for different values of power law exponent. (a) weak coupling, (b) strong coupling. Here, $k_1 = 0.5$, $D = 0.0001$, $W = 1$ and $N = 100$.

exponent, α , on the network with $g < 1.8$ is shown in fig. 5.11(a). It is found that synchrony in the memristive neural network decreases with increasing value of α . For strong mean field coupling, $g > 1.8$, as shown in fig. 5.11(b), the synchrony decreases with increase in coupling strength, for low values of α , represented by the blue and red lines. For higher values of α , the synchrony is unaltered as shown by the yellow and purple lines. Thus, the studies have shown that for low value of α , *i.e.*, global coupling, the synchrony increases with increasing coupling strength and then reduces. But for high values of α , *i.e.*, nonlocal or local interactions, synchrony is rather unaltered.

The existence of incoherent, chimera, multichimera and coherent states is observed in the memristive HR network with distance-dependent coupling due to the interplay between g and α . Fig. 5.12(a) shows incoherent state, whereas fig. 5.12(b) shows imperfect synchronisation with 7 escaping neurons. Figs. 5.12(c)-5.12(e) show chimera states. Multichimera states are shown in fig. 5.12(f) and 5.12(g). Figs 5.12h and 5.12(i) represent coherent states.

To distinguish incoherent, chimera and coherent states, the quantitative measures called SI and DM have been calculated by defining the local standard deviation from the time series, which are given by the formulae in Eqs. (1.13) and (1.14).

We have calculated SI and DM, using Eqs. (1.13), (1.14) for various values of α which are presented in fig. 5.13. As shown in figs. 5.13(a) and 5.13(b), for low values of g , incoherent, chimera, multichimera and coherent states are obtained, whereas for high values of g , the system shows chimera and multichimera states when $\alpha = 0.5$. When $\alpha = 1$, system shows incoherent, chimera, multichimera and coherent states, for $g < 3$ and exhibits coherence for $g > 3$, as shown in figs. 5.13(c) and 5.13(d). As α increases, the value of g for which the system shows coherence also increases. On further increasing α , the system attains incoherent, chimera and multichimera states as shown in figs. 5.13(e), 5.13(f), 5.13(g) and 5.13(h). The study has shown that for high values of α system fails to attain coherence. Hence, the parameter space for low values of α has been drawn to study the rich dynamics exhibited by the system in this regime.

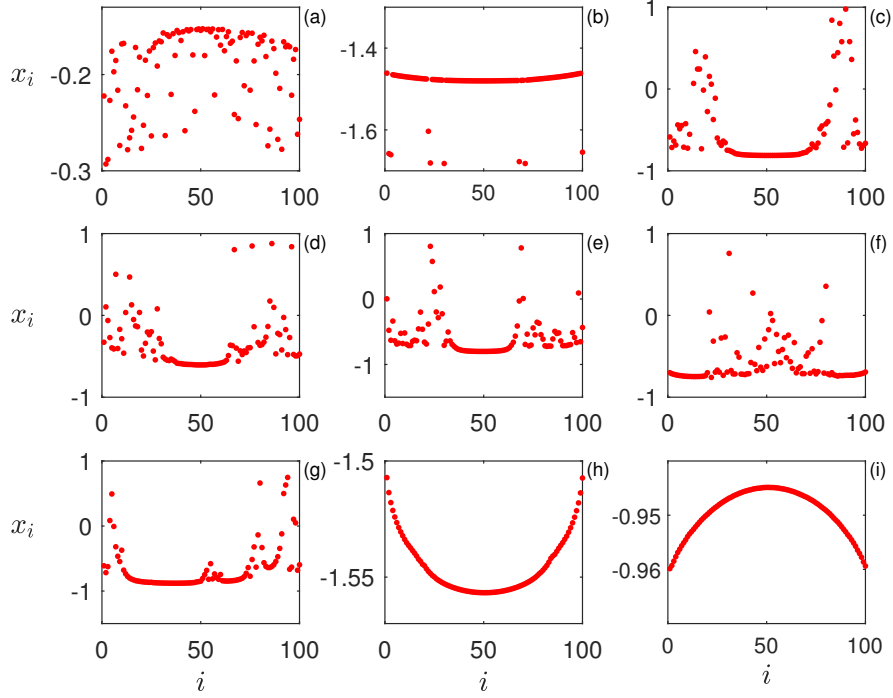


Figure 5.12: Snapshots of the HR network with distance-dependent memristor and mean field effects. (a) incoherent state ($k_1 = 0.5, \alpha = 0.1, g = 0.1$), (b) imperfect synchrony ($k_1 = 0.5, \alpha = 0.1, g = 1.7$), (c) chimera state ($k_1 = 0.5, \alpha = 0.3, g = 1.1$), (d) chimera state ($k_1 = 0.5, \alpha = 0.5, g = 1.37$), (e) chimera state ($k_1 = 0.5, \alpha = 0.5, g = 1.9$), (f) multichimera state ($k_1 = 0.5, \alpha = 0.4, g = 1.8$), (g) multichimera state ($k_1 = 0.5, \alpha = 0.5, g = 2.13$), (h) coherent state ($k_1 = 0.7, \alpha = 0.5, g = 0.9$), (i) coherent state ($k_1 = 1, \alpha = 0.5, g = 0.7$). Here, $D = 0.0001, W = 1$ and $N = 100$.

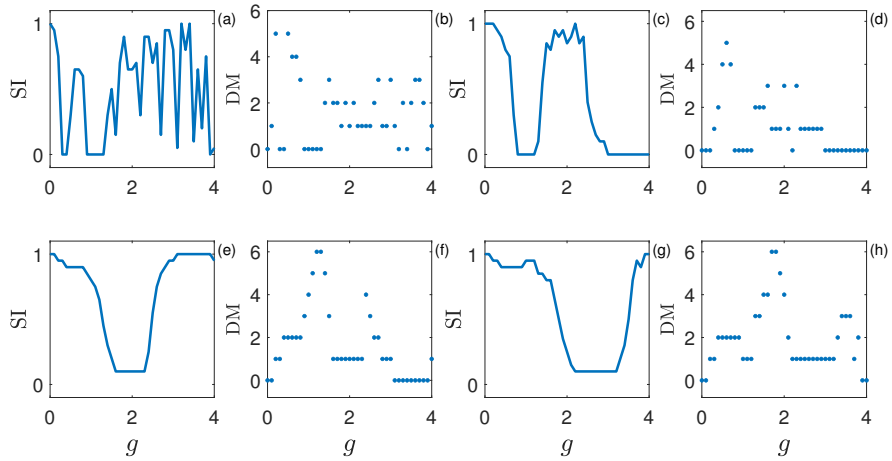


Figure 5.13: Variation of the strength of incoherence and discontinuity measure for different values of the mean field coupling strength. (a) $\alpha = 0.5$, (c) $\alpha = 1$, (e) $\alpha = 1.5$ and (g) $\alpha = 2$ show the strength of incoherence. (b), (d), (f) and (h) present the discontinuity measure for same values of α . Here, $k_1 = 0.5, D = 0.0001, W = 1, N = 100, M = 20, \epsilon = 0.06$.

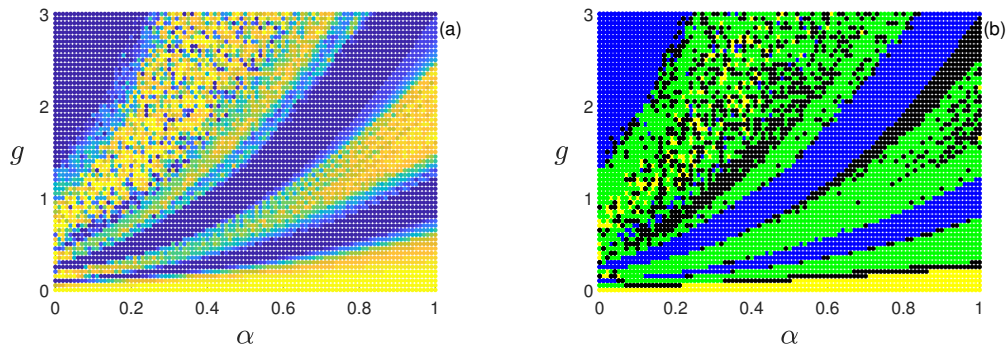


Figure 5.14: Parameter phase diagram in $\alpha - g$ plane for a network of memristive HR neurons. (a) Strength of incoherence and (b) Discontinuity measure. Here, $k_1 = 0.5$, $D = 0.0001$, $W = 1$, $N = 100$, $M = 20$ and $\epsilon = 0.06$.

The parameter space ($\alpha - g$) shows incoherent, chimera, multichimera and coherent states, as shown in fig. 5.14. The variation of SI with parameters α and g is presented in fig. 5.14(a). Incoherent and coherent states are represented by the yellow and the blue colours, respectively. The system exhibits incoherence for low values of g . As α increases, the value of g for which the system shows coherence also increases. The region of occurrence of chimera and multichimera states are exactly distinguished using, DM, as shown in fig. 5.14(b). Yellow, blue, green and black colours indicate incoherence, coherent, multichimera and chimera states, respectively. It is found that the presence of chimera and multichimera states are overlapped with each other. The parameter space reveals the collective dynamics of the system which are in exact agreement with studies of SI and DM.

5.4 Results and conclusions

A linear chain network of HR neurons with magnetic coupling and external stimuli of different forms has been analysed. The magnetic coupling is capable of inducing plateau bursting and amplitude death in the HR neurons with constant external input. The phase space trajectories are controlled and shrink to a single point with the increase in magnetic coupling strength, representing synchrony and amplitude death. The synchrony is quantified using the statistical factor of synchronisation. The HR neural network with magnetic coupling is also analysed in the presence of sinusoidal and square waves. The dynamics of the individual

neurons are square wave bursting and spiking in the presence of sinusoidal and square inputs, respectively. In the presence of time varying external inputs, the phase space trajectories of the system are reduced to beeline for high magnetic coupling strength. The statistical factor of synchronisation justifies the fact that the sinusoidal input enhances synchrony and the square input suppresses the synchrony in the network, compared to the constant input. The inputs with high frequencies have greater ability to enhance and suppress the synchrony.

The HR network has been modified by introducing a distance-dependent mean field coupling with a power law exponent. This modification helps to realise the various types of interactions (such as global, nonlocal, or local coupling) by varying the power law exponent. The uniform mean field (with zero power law exponent) coupling accelerates synchrony in memristive HR neurons. The combined effect of memristor and uniform mean field effects produces mixed dynamics of square wave and plateau bursting. The uniform mean field initiates synchronised bursting in the AD state of memristive network. The study of pattern formations reveals that the system undergoes desynchronised, mixed oscillatory and imperfect synchronised state before attaining complete synchrony. The synchrony level of memristive network increases initially and then decreases with increase in mean field coupling strength, in global coupling, whereas the synchrony is unaltered in nonlocal or local interactions. The complete synchrony or global death state is unattainable in the network with distance dependence governed by power law. The network shows incoherent, chimera, multichimera and coherent states. It is found that, even for low values of power law exponent, incoherent, chimera, multichimera and coherent states are obtained. The existence of chimera states in system with long range interactions are verified by parameter space. The long range interactions are common in many physical and biological systems. The study on such systems will help us to get more information about chimera states.

Chapter 6

Memristive Hindmarsh-Rose neurons with chemical cross coupling

6.1 Introduction

On account of the significance of synchrony, the brain finds its own mechanism to restore the lost synchrony. There are different methods of representing this mechanism mathematically. Adhikari *et al.* analysed the phase transition to synchrony in a network of bursting neurons owing to the time delay in synaptic coupling [132, 186]. The cross coupling between the state variables was also used to boost the synchronisation procedure by getting added to the pre-existing self coupling [187]. The structural anomalies of the brain observed experimentally were given a theoretical foundation by the neuron models with cross coupling of state variables [44]. The phase synchronisation of coupled HR neurons with magnetic and electrical cross couplings is also discussed [45]. Chemical coupling which is nonlinear in nature is found to increase the stochastic coherence of the system, in comparison with the linear electrical coupling [26]. Chimera states were obtained in chemically coupled nonlocal networks of Morris Lecar neurons [55]. The capability of the time delays to induce phase coherent dynamic be-

haviours in chemically coupled network [188].

The energy aspects of HR neurons with electrical, chemical and field couplings have also been analysed [158]. The magnetic stimulation is found to alter firing activity and neural synchronisation in a HR neural network [21, 172]. The suppression of chaotic states and enrichment of neural synchrony in a system of two coupled HR neurons under the effect of electromagnetic induction is reported [180].

In this chapter, the synchronisation scenario of a network of HR neurons with self and cross interactions between membrane potential and magnetic flux in chemical mode is analysed. The chapter is organised as follows: The influence of self, mixed and cross coupling of state variables in two coupled HR neurons is analysed in section 6.2. The stability of the synchrony induced is verified using Lyapunov function approach. The study is extended to N coupled network and is presented in section 6.3. The synchrony in the network, with global interaction, is quantified using the statistical factor of synchronisation which is presented in section 6.3.1. The influence of nonlocal coupling is discussed in section 6.3.2. The studies are concluded in section 6.4.

6.2 Two coupled system

In this chapter, in addition to the magnetic coupling, we also consider the cross synaptic coupling between membrane potential and magnetic flux in chemical mode. The dynamical equations of two coupled system of HR neurons modelled to realise cross interactions between membrane potential and magnetic flux, in chemical mode is given as:

$$\begin{aligned}
 \dot{x}_i &= y_i - ax_i^3 + bx_i^2 - z_i + I - k_1\rho(\phi_i)x_i + g[b_{xx}\Gamma_{i,j}(x) + b_{x\phi}\Gamma_{i,j}(\phi)], \\
 \dot{y}_i &= c - dx_i^2 - y_i, \\
 \dot{z}_i &= r(s(x_i - x_e) - z_i), \\
 \dot{\phi}_i &= k_2x_i - k_3\phi_i + g[b_{\phi x}\Gamma_{i,j}(x) + b_{\phi\phi}\Gamma_{i,j}(\phi)], \quad i, j = 1, 2; i \neq j.
 \end{aligned}
 \tag{6.1}$$

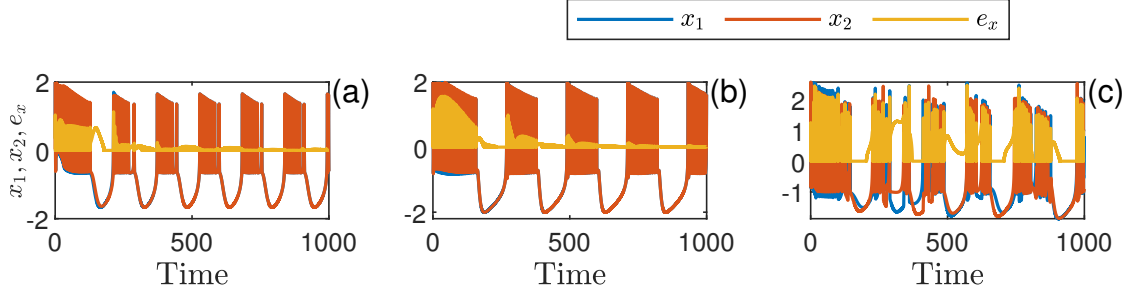


Figure 6.1: Time series of two coupled HR neurons. (a) $\delta = 0, g = 1$, (b) $\delta = \frac{\pi}{4}, g = 0.5$, (c) $\delta = \frac{\pi}{2}, g = 0.5$. Here, $k_1 = 0.4$.

x_i, y_i and z_i represent the membrane potential, spiking variable and bursting variable of i th neuron, respectively. y_i is constituted by the flow of Na^+ and K^+ ions and the flow of Ca^+ ions constitute the z_i term. The fast oscillations of x_i and y_i correspond to spikes, whereas the slow oscillations of the z_i variable cause burst [132]. Indices i, j represent presynaptic neuron and postsynaptic neuron, respectively. g represent the coupling strength. ϕ_i describes the magnetic flux across the membrane, $k_1\rho(\phi_i)x$ denotes induction current and k_1 is the induction coefficient [21, 22]. The term $\rho(\phi_i) = \tanh(\phi_i)$ [170], is the memory-conductance of a magnetic flux-controlled memristor.

The neurons are coupled through chemical synapse represented by the term:

$$\Gamma_{i,j}(x) = (v - x_i)(1/(1 + \exp(-\lambda(x_j - \theta)))), \quad (6.2)$$

In order to maintain the synapse as excitatory, the reversal potential v is always maintained to be greater than the membrane potential x_i of all neurons at all times. The exponential term is a sigmoidal nonlinear function, with λ determining the slope of the function and θ denoting the synaptic firing threshold. The external current, I , controls the qualitative behaviour of the neurons. The parameters are chosen as: $a = 1, b = 3, c = 1, d = 5, r = 0.006, s = 4, x_e = -1.61, I = 3.1$ [18], $k_2 = 0.9, k_3 = 0.5$ [21], $v = 2, \lambda = 7.5, \theta = -0.25$ [158]. The initial conditions (x_0, y_0, z_0) are randomly chosen as to lie in the range $[-0.5, 0.5]$ and ϕ_0 in $[0, 1]$.

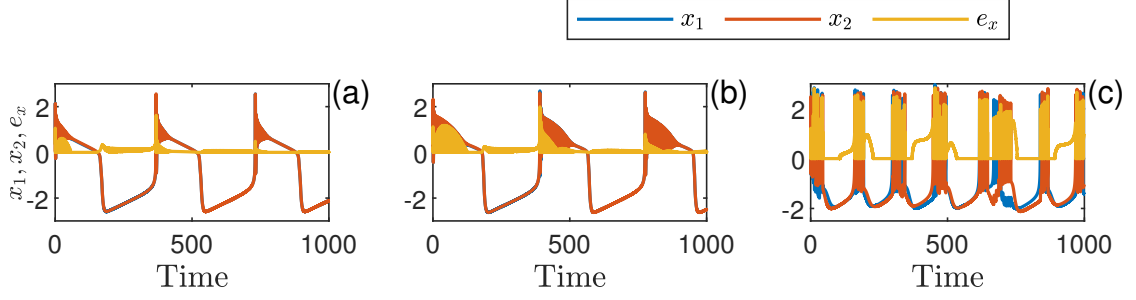


Figure 6.2: Time series of two coupled HR neurons. (a) $\delta = 0, g = 0.5$, (b) $\delta = \frac{\pi}{4}, g = 0.5$, (c) $\delta = \frac{\pi}{2}, g = 0.5$. Here, $k_1 = 1.5$.

The elements $b_{xx}, b_{x\phi}, b_{\phi x}$ and $b_{\phi\phi}$ form the components of a coupling matrix. A general form for this coupling matrix which incorporates self and cross coupling is given by:

$$B = \begin{pmatrix} b_{xx} & b_{x\phi} \\ b_{\phi x} & b_{\phi\phi} \end{pmatrix} = \begin{pmatrix} \cos \delta & \sin \delta \\ -\sin \delta & \cos \delta \end{pmatrix}$$

Where $\delta \in [-\pi, \pi)$ is the coupling phase. The switching between the interactions are made easy by varying the values of δ . We have analysed the system of HR neurons in three different cases:

- (i) Self coupling in x and ϕ , $\delta = 0$.
- (ii) Mixed coupling in x and ϕ , $\delta = \frac{\pi}{4}$.
- (iii) Cross coupling in x and ϕ , $\delta = \frac{\pi}{2}$.

The different firing patterns of the two coupled system is analysed using the time series. The firing patterns of the system with low magnetic coupling ($k_1 = 0.4$) for different interactions in chemical mode is shown in fig. 6.1. The synchrony in the system is exhibited using the error term, $e_x = \sqrt{x_1^2 - x_2^2}$. Both neurons show square wave bursting character which is visible from the red and blue lines (blue line is hidden by the red). The yellow line representing the error indicates the synchrony in the network induced by the self coupling in the variables, for $\delta = 0$, as shown in fig. 6.1(a). The mixed coupling realised with $\delta = \frac{\pi}{4}$ in fig. 6.1(b) also induces synchrony, represented by the yellow line.

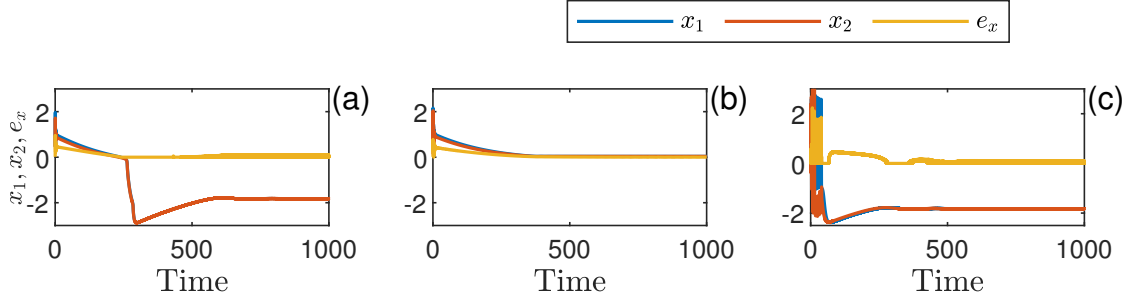


Figure 6.3: Time series of two coupled HR neurons. (a) $\delta = 0, g = 0.5$, (b) $\delta = \frac{\pi}{4}, g = 0.5$, (c) $\delta = \frac{\pi}{2}, g = 0.5$. Here, $k_1 = 2.4$.

The dynamics is square wave bursting with an increased number of spikes per burst. But cross coupling ($\delta = \frac{\pi}{2}$) is incapable of inducing synchrony, as shown in fig. 6.1(c) and the dynamics is irregular bursting. Self and mixed coupling of variables helps attain synchrony whereas, synchrony is unattainable with cross coupling alone.

The changes in firing patterns for $k_1 = 1.5$ is presented in fig. 6.2. With increase in magnetic coupling, the dynamics is transformed from square wave bursting to plateau bursting for self and mixed couplings, as shown in figs. 6.2(a) and (b). The system do exhibit a degree of synchronisation though not achieving complete synchrony. The chaotic irregular bursting and the unattainability of synchrony in system for pure cross coupling ($\delta = \frac{\pi}{2}$) is shown in fig. 6.2(c). The capability of self and mixed coupling in inducing synchrony and unattainability of synchrony in cross coupling is justified at higher magnetic coupling, $k_1 = 1.5$.

The system shows synchronised dynamics at high value of magnetic coupling ($k_1 = 2.4$), for self, mixed and cross coupling, as shown by yellow lines in figs. 6.3(a), (b) and (c), respectively. The dynamics at the synchronised state is Amplitude Death (AD) state, where the oscillations of the system is quenched and a stable state condition is achieved, as represented by the blue and red lines. Here, the magnetic coupling overrides the effect of chemical coupling [153] and induces synchrony in any coupling scheme.

The stability of synchronous states

The stability of the synchrony attained in the two coupled system is analysed using master stability approach. The error dynamical equations are calculated by considering the difference between state variables of the neurons. When the system reaches a synchronised state where $(x_1, y_1, z_1, \phi_1) = (x_2, y_2, z_2, \phi_2)$, the error terms $x_\perp = x_2 - x_1, y_\perp = y_2 - y_1, z_\perp = z_2 - z_1, \phi_\perp = \phi_2 - \phi_1$ approach zero as time approaches infinity and there exist a synchronous solution. The stability equations for perturbations transverse to the synchronisation manifold are of the form:

$$\begin{aligned}
\dot{x}_2 - \dot{x}_1 &= (y_2 - y_1) - 3a(x_2^2 - x_1^2) + 2b(x_2 - x_1) - (z_2 - z_1) - k_1 \left[\tanh(\phi_2)x_2 \right. \\
&\quad \left. - \tanh(\phi_1)x_1 \right] + g \cos \delta \left[(v - x_2)\Gamma(x_1) - (v - x_1)\Gamma(x_2) \right] + g \sin \delta \\
&\quad \left[(v - \phi_2)\Gamma(x_2) - (v - \phi_1)\Gamma(x_1) \right] \\
\dot{y}_2 - \dot{y}_1 &= -2d(x_2 - x_1) - (y_2 - y_1), \\
\dot{z}_2 - \dot{z}_1 &= rs(x_2 - x_1) - r(z_2 - z_1), \\
\dot{\phi}_2 - \dot{\phi}_1 &= k_2(x_2 - x_1) - k_3(\phi_2 - \phi_1) - g \sin \delta \left[(v - x_2)\Gamma(x_1) - (v - x_1)\Gamma(x_2) \right] \\
&\quad + g \cos \delta \left[(v - \phi_2)\Gamma(x_2) - (v - \phi_1)\Gamma(x_1) \right]
\end{aligned} \tag{6.3}$$

On simplifying,

$$\begin{aligned}
\dot{x}_\perp &= y_\perp - 3ax_\perp + 2bx_\perp - z_\perp - k_1(x\phi_\perp + \phi_\perp x) - g \cos \delta \Omega(x)x_\perp - g \sin \delta \Omega(\phi)\phi_\perp \\
\dot{y}_\perp &= -2dx_\perp - y_\perp, \\
\dot{z}_\perp &= rsx_\perp - z_\perp, \\
\dot{\phi}_\perp &= k_2x_\perp - k_3\phi_\perp + g \sin \delta \Omega(x)x_\perp - g \cos \delta \Omega(\phi)\phi_\perp.
\end{aligned} \tag{6.4}$$

Where $\tanh(\phi_{i,j'})x_{i,j'} + \tanh(\phi_{1,j'})x_{1,j'}$ is approximated as $x_{i+1,j'}\phi_{\perp,i,j'} + \phi_{i,j'}x_{\perp,i,j'}$ and $\Omega(f) = (1/(1 + \exp(-\lambda(f-\theta)))) + (v-f)(-\lambda(f-\theta))/(((1 + \exp(-\lambda(f-\theta))))^2)$.

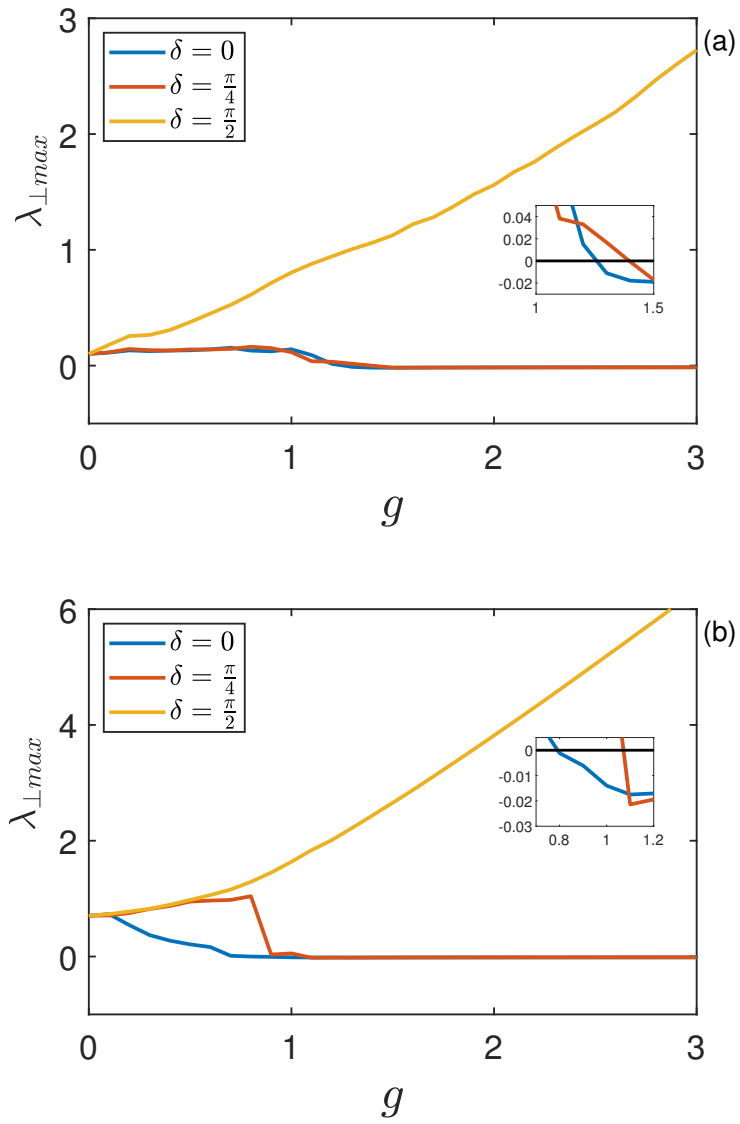


Figure 6.4: Variation of the MTLE with coupling strength (g) for different values of δ . (a) $k_1 = 0.4$ and (b) $k_1 = 1.5$.

The Jacobian for the whole network with chemical cross coupling will have the following structure:

$$\begin{pmatrix} J_{1,1} + \gamma_{1,1}E & \gamma_{1,2}E \\ \gamma_{2,1}E & J_{2,2} + \gamma_{2,2}E \end{pmatrix} \quad (6.5)$$

where,

$$J_{i,i} = \begin{pmatrix} 2ax_i - 3bx_i^2 - k_1\phi_i - g \cos \delta\Omega(x) & 1 & -1 & -k_1x - g \sin \delta\Omega(\phi) \\ -2dx_i & -1 & 0 & 0 \\ rs & 0 & -r & 0 \\ k_2 + g \sin \delta\Omega(x) & 0 & 0 & -k_3 - g \cos \delta\Omega(\phi) \end{pmatrix} \quad (6.6)$$

and

$$E = \begin{pmatrix} \cos \delta & 0 & 0 & \sin \delta \\ 0 & 0 & 0 & 0 \\ 0 & 0 & 0 & 0 \\ -\sin \delta & 0 & 0 & \cos \delta \end{pmatrix} \quad (6.7)$$

The terms $\gamma_{i,i}$ and $\gamma_{i,j}$ are obtained by partially differentiating $g(v - f_i)\Gamma(f_j)$ with respect to f_i and f_j , respectively. The Jacobian given by Eq. (6.5) is diagonalised in a coordinate system that isolates the stability of the synchronisation manifold from the transverse directions. The maximum transverse Lyapunov exponent (MTLE), $\lambda_{\perp max}$ is used as the bifurcation function to study the stability of synchrony. The system is stabilised when MTLE becomes negative. The variation of $\lambda_{\perp max}$ with g for different values of δ and k_1 is presented in fig. 6.4. Fig. 6.4(a) presents the synchrony of the system with $k_1 = 0.4$. The system with self and mixed interactions, presented by blue and red lines are stabilised at $g = 1.3$ and $g = 1.4$, respectively, which is clear from the inset figure. The system with cross coupling presented by the yellow line in fig. 6.4(a) never attains synchrony. The stability of synchrony for self, mixed and cross couplings at $k_1 = 1.5$ is shown in fig. 6.4(b). The self and mixed coupled systems attain

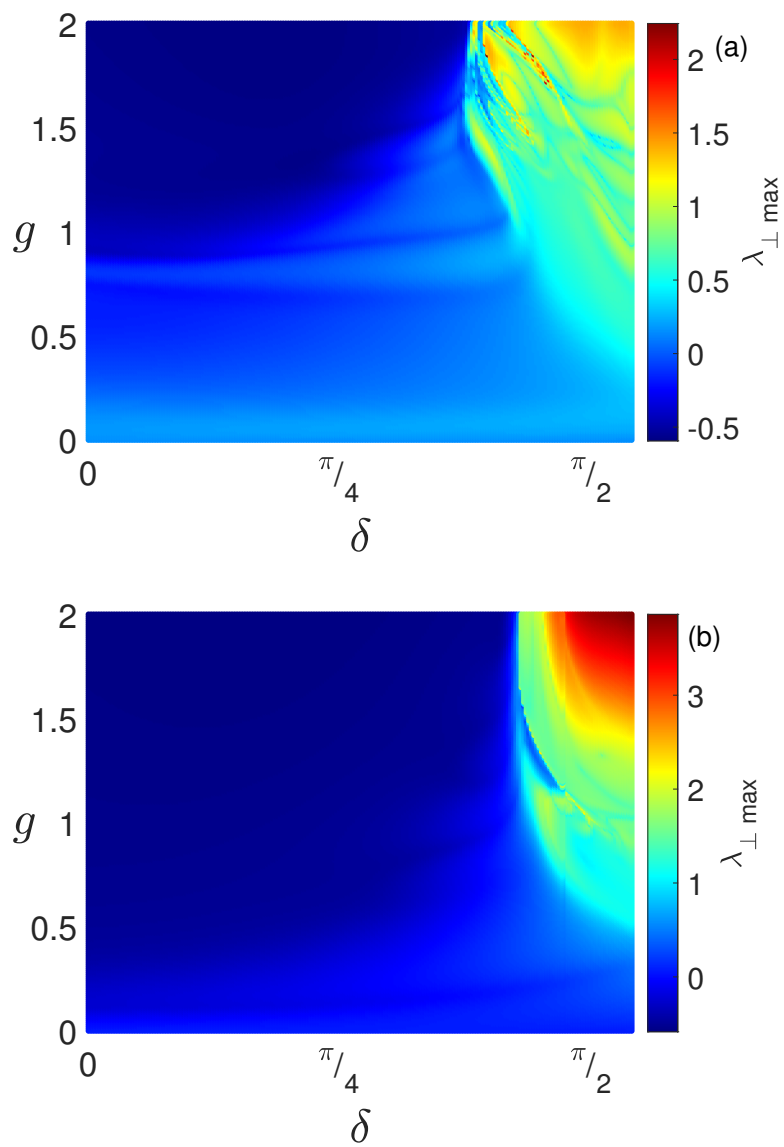


Figure 6.5: Colour coded variation of MTLE for different values of g and δ . (a) $k_1 = 0.4$ and (b) $k_1 = 1.5$.

synchrony at $g = 0.8$ and $g = 1$, respectively, which is well visible in the inset. The cross coupled system never attains synchrony as the yellow line never crosses the zero line. The synchrony is attained at lower coupling strength, compared to a weakly magnetically coupled system. The incapability of cross coupling in inducing synchrony is visible with the yellow line never approaching a zero value, however, it constructively takes part with self coupling in inducing synchrony.

The parameter space with δ on the X-axis and g on the Y-axis with colourbar representing the variation of $\lambda_{\perp max}$ is shown in fig. 6.5. The fig. 6.5(a) reveals the synchronisation scenario with low magnetic coupling strength $k_1 = 0.4$. For low value of chemical coupling, g , synchrony is unattainable. For high value of g , synchrony is obtained for self and mixed interactions. At $\delta = 0$, the interaction is self alone and synchrony is obtained. With an increase in value of δ , the cross coupling comes into action with self coupling to form mixed coupling. The system exhibits synchrony for mixed coupling till $\delta < \frac{3\pi}{8}$. The contributions from self coupling are decreasing and interactions are solely from cross coupling for values $\delta > \frac{3\pi}{8}$. In this region synchrony is unattainable. At high magnetic coupling strength ($k_1 = 1.5$), as shown in fig. 6.5(b), synchrony is obtained for even low values of g in self and mixed interactions. Here, the influence of self coupling is more intense than cross coupling. But for $\delta > \frac{3\pi}{8}$, cross coupling overrides the effect of self coupling and is incapable of inducing synchrony.

6.3 The N coupled system

The influence of cross coupling of state variables has been analysed in a network of HR neurons arranged in ring structure. The dynamical equations are of the

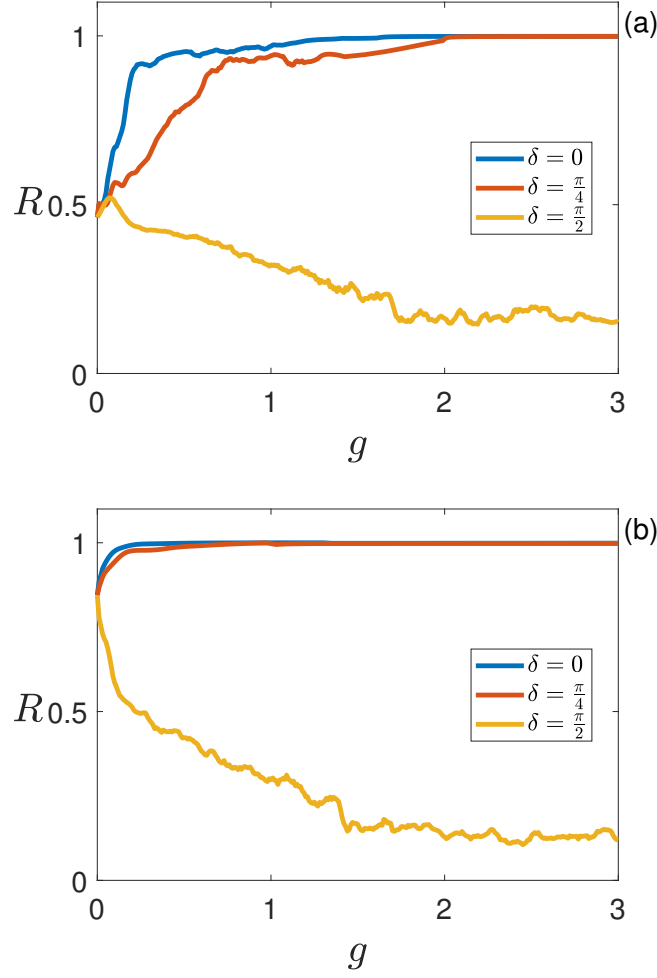


Figure 6.6: Variation of the statistical factor of synchronisation with coupling strength for different values of δ . (a) $k_1 = 0.4$, (b) $k_1 = 1.5$.

form:

$$\begin{aligned}
 \dot{x}_i &= y_i - ax_i^3 + bx_i^2 - z_i + I + \frac{g}{2p} \sum_{j=i-p}^{j=i+p} [b_{xx}\Gamma_{i,j}(x) + b_{x\phi}\Gamma_{i,j}(\phi)], \\
 \dot{y}_i &= c - dx_i^2 - y_i \\
 \dot{z}_i &= r(s(x_i - x_e) - z_i), \\
 \dot{\phi}_i &= k_2x_i - k_3\phi_i + \frac{g}{2p} \sum_{j=i-p}^{j=i+p} [b_{\phi x}\Gamma_{i,j}(x) + b_{\phi\phi}\Gamma_{i,j}(\phi)],
 \end{aligned} \tag{6.8}$$

where $i = 1, 2, \dots, N$. The network consists of N neurons, each of which is coupled to p neighbouring neurons in both directions of the ring.

6.3.1 The synchronisation scenario

The synchronisation scenario in the presence of cross coupling of variables in magnetically coupled HR neurons in ring topology is analysed in this section. The total number of neurons in the network, N is fixed as 135 and $p = \frac{N-1}{2}$, to realise global interaction. The amount of synchrony is quantified using the statistical factor of synchronisation, R , given by the Eq. (1.3).

The variation of R with g , for different values of δ is shown in fig. 6.6. At low magnetic coupling ($k_1 = 0.4$), the synchrony induced in the absence of chemical cross coupling is $R \approx 0.5$, as shown in fig. 6.6(a). The blue, red and yellow lines represent the variation of R for self, mixed and cross coupling. For $g < 2$, the synchrony in the system increases for self and mixed coupling. But it is to be noted that synchrony is attained at a faster rate in self coupled system compared to the one with mixed coupling. For $g > 2$, the self and mixed coupling have the same influence and all the neurons in the network are in AD exhibiting complete synchrony. However, the system with sole cross coupling is incapable of inducing synchrony at any value of g .

The synchrony level is high ($R \approx 0.8$) for $k_1 = 1.5$, in the absence of chemical coupling. Under the influence of self and mixed coupling, the synchrony further increases and approaches unity for low values of g . Both self and mixed coupling have similar influences. In the presence of sole cross coupling, the system is incapable of attaining synchrony. The incapability of sole cross coupling to induce synchrony is justified in a network of neurons with weak and strong magnetic coupling as well.

6.3.2 The pattern formations

The network of HR neurons in ring topology is analysed in nonlocal interactions with cross coupling of variables. The system is found to exhibit chimera and multichimera states under the effect of mixed coupling and is presented in fig. 6.7. The multichimera states obtained for $\delta = \frac{\pi}{2} - 1$ are shown in figs. 6.7(a), (b), (c), (d) and (e) for self and mixed coupling schemes. The chimera states

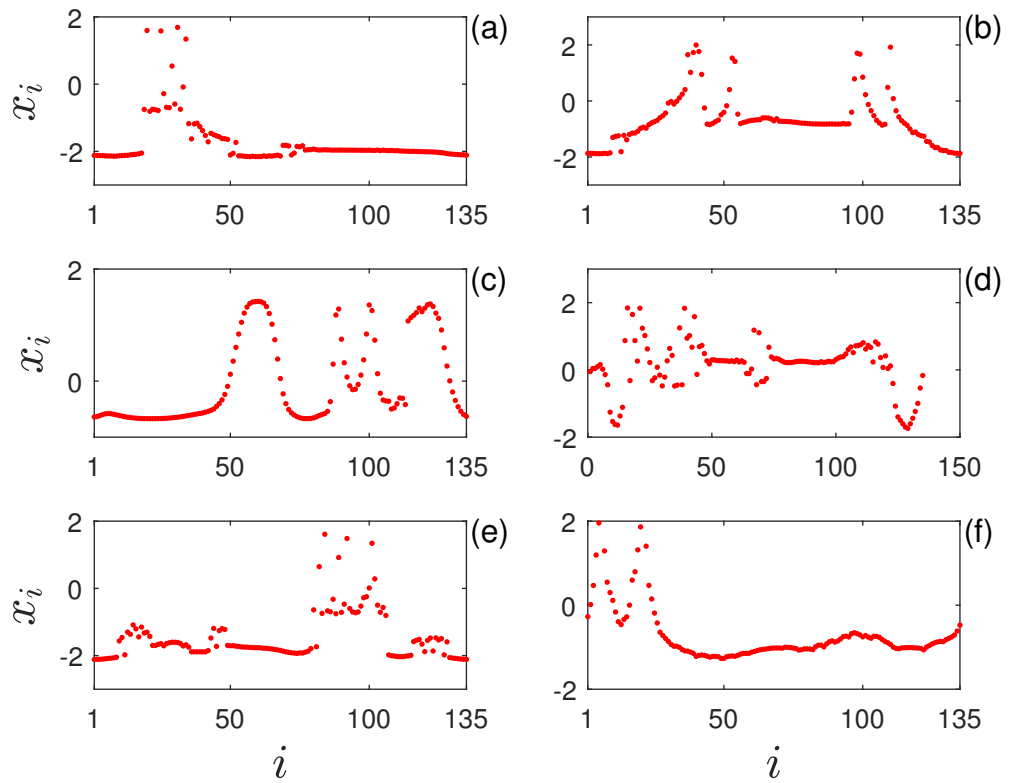


Figure 6.7: Snapshots of membrane potential under the influence of mixed interactions in chemically coupled HR neurons with magnetic coupling. (a) $p = 10, \delta = \frac{\pi}{2} - 1, g = 0.3$, (b) $p = 10, \delta = 0, g = 0.2$, (c) $p = 5, \delta = 0, g = 0.6$, (d) $p = 10, \delta = \frac{\pi}{4}, g = 0.9$, (e) $p = 5, \delta = \frac{\pi}{2} - 1, g = 0.3$, (f) $p = 5, \delta = \frac{\pi}{2} - 1, g = 0.5$.

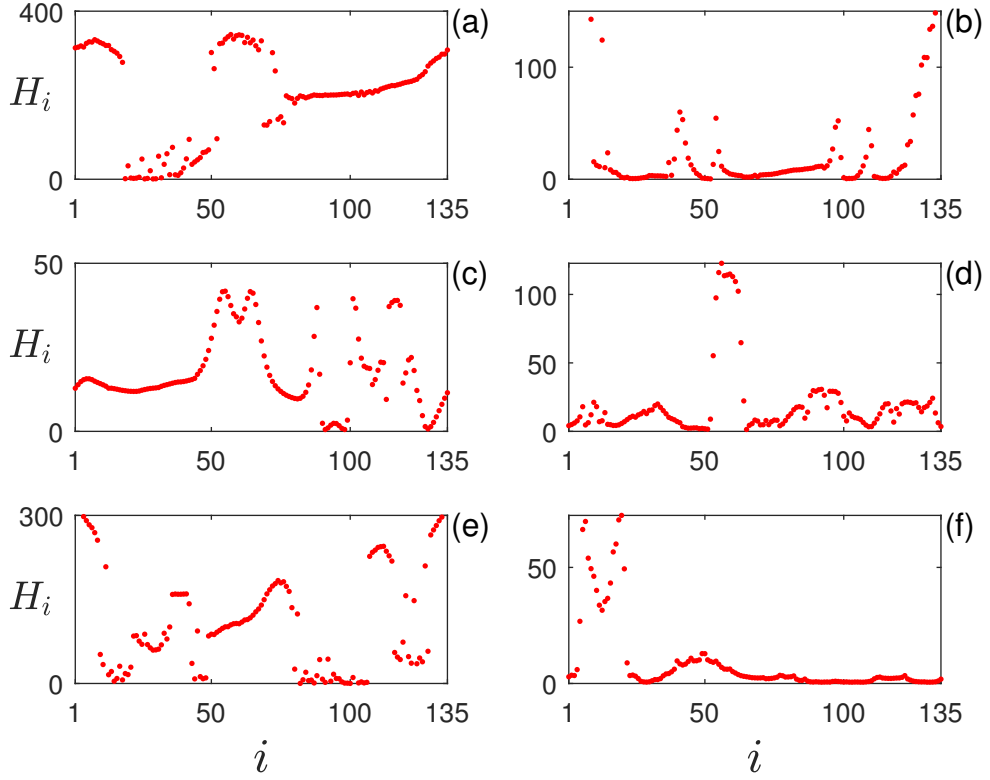


Figure 6.8: The variation of energies of the neurons in the network. (a) $p = 10, \delta = \frac{\pi}{2} - 1, g = 0.3$, (b) $p = 10, \delta = 0, g = 0.2$, (c) $p = 5, \delta = 0, g = 0.6$, (d) $p = 10, \delta = \frac{\pi}{4}, g = 0.9$, (e) $p = 5, \delta = \frac{\pi}{2} - 1, g = 0.3$, (f) $p = 5, \delta = \frac{\pi}{2} - 1, g = 0.5$.

obtained for $\delta = \frac{\pi}{2} - 1$ is presented in fig. 6.7(f).

The chimera states are the coexistence of coherent and incoherent oscillators. The Hamilton energy function has been faithfully used to analyse the energy of the system and the energy function corresponding to the HR system represented by Eq. (6.1) satisfies the equation [21, 87]:

$$(y_i - z_i + I - \phi_i) \frac{\partial H_i}{\partial x_i} + (c - dx_i^2) \frac{\partial H_i}{\partial y_i} + rs(x_i - x_e) \frac{\partial H_i}{\partial z_i} + k_2 x_i \frac{\partial H_i}{\partial \phi_i} = 0 \quad (6.9)$$

A general solution for the Eq. (6.9) is given as:

$$H_i = \frac{2}{3} dx_i^3 - 2x_i + rs(x_i - x_e)^2 + (y_i - z_i + I - \phi_i)^2 + k_2 x_i^2 \quad (6.10)$$

The Eq. (6.10) is used to analyse the energy of each neuron in the network.

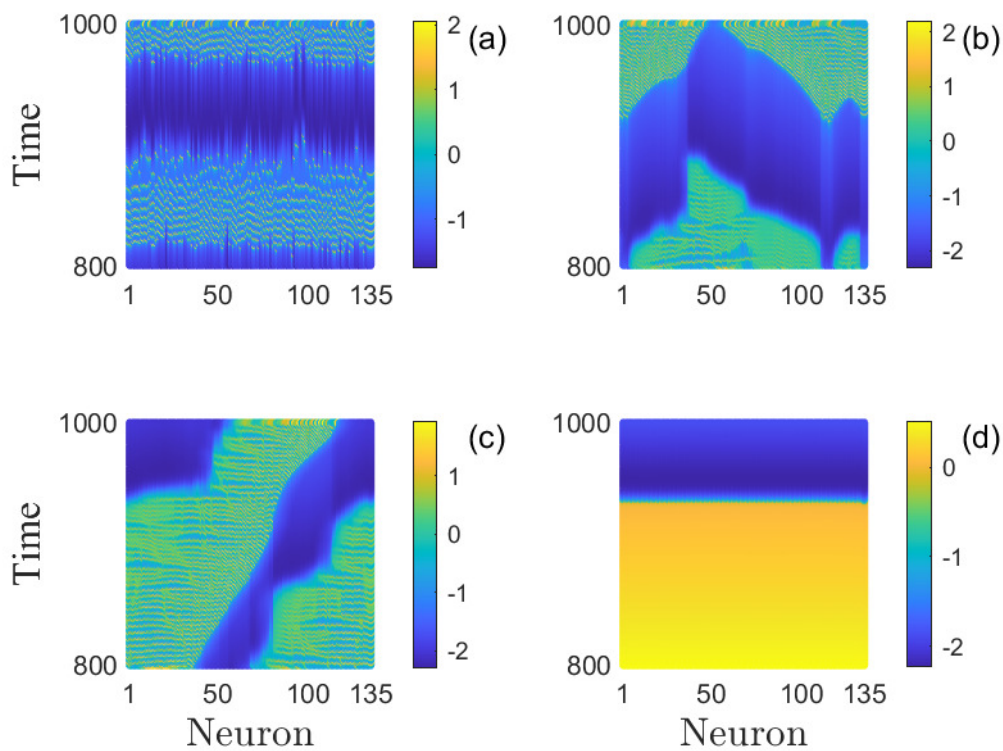


Figure 6.9: The spatiotemporal patterns of the network. (a) desynchrony ($p = 10, \delta = 0, g = 0.1$), (b) travelling chimera ($p = 5, \delta = \frac{\pi}{4}, g = 0.7$), (c) travelling chimera ($p = 10, \delta = 0.8, g = 0.8$) and (d) global synchrony ($p = 5, \delta = 0, g = 1.3$). Here, $k_1 = 0.4$. The colourbar represents the membrane potential, x .

The variations in the Hamilton energy function corresponding to the pattern formations shown in fig. 6.7 are depicted in fig. 6.8. From fig. 6.8(a), it is observed that the energy of the coherent neurons is higher compared to the incoherent ones. Here, the potential of the coherent neurons is at a higher negative potential compared to the incoherent ones. Conversely, in fig. 6.8(b), the potential of the neurons exhibiting coherence is near zero and the energy of the coherent neurons is lower compared to the incoherent states. In figs. 6.8(c) and 6.8(d), the energy of the coherent neurons is also lower than that of the incoherent states and the potential of the neurons in the coherent states is near zero. Similarly, in fig. 6.8(e), the energy of the coherent states is higher compared to the incoherent states with the coherent neurons placed at a high negative potential. Finally, in fig. 6.8(f), the energy of the coherent states is lower, with the potential of coherent neurons near zero. Based on these observations, it can be concluded that to maintain the neurons in a coherent state at a high potential, regardless of polarity, higher energy utilisation is required. On the other hand, if the potential of the neurons in a coherent state is near zero, the energy utilisation is lower.

The spatiotemporal patterns of the network is analysed. The variations in the membrane potential, x_i for the different neuron is analysed in the network for a range of time and presented in fig. 6.9. The neuron number is represented in X-axis and time is presented in Y-axis. The membrane potential is represented by the colourbar. The desynchronised state is represented in fig. 6.9(a). Travelling chimeras obtained are presented in figs. 6.9(b) and (c). Fig. 6.9(d) represents the completely synchronised state.

6.3.3 Quantifying chimeras

The emergence of chimera and multichimera states in the network due to the topology and coupling scheme is analysed with the help of a quantitative measure called strength of incoherence (SI) and discontinuity measure (DM), given by Eqs. (1.13) and (1.14).

The variation of SI and DM with g for different values of δ are presented in fig. 6.10. The incoherent, chimera and coherent states obtained in a system

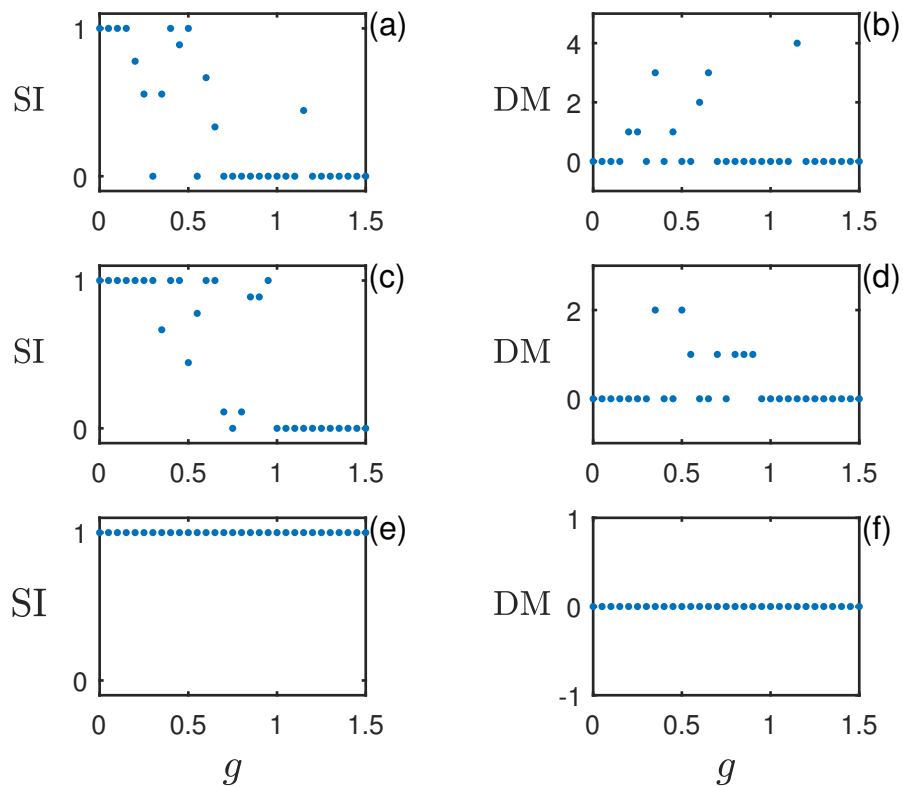


Figure 6.10: Variation of the strength of incoherence and discontinuity measure with coupling strength for self, mixed and cross couplings. The left panel shows the strength of incoherence of (a) self, (c) mixed and (e) cross couplings. The right panel shows the discontinuity measures for (b) self, (d) mixed and (f) cross couplings. Here, $k_1 = 0.4$, $\epsilon = 0.05$, $p = 10$.

with self coupling are presented in fig. 6.10(a). The chimeras and multichimeras are distinguished by using DM as shown in fig. 6.10(b). In a mixed coupled system, incoherent, chimera and coherent states are obtained as shown in fig. 6.10(c). Fig. 6.10(d) distinguishes the chimeras and multichimeras for mixed coupling. From fig. 6.10(e), it is clear that the cross coupled system exhibits only incoherent states. The chimera or coherent states are never obtained in the cross coupled system. It is further justified by DM as shown in fig. 6.10(f).

6.4 Results and conclusions

The synchrony and pattern formations in HR neurons with self, mixed and cross interactions between membrane potential and electromagnetic flux in chemical mode are analysed in this chapter. In the system of two coupled neurons, the time series shows that self coupling induces synchrony in the system. Sole cross coupling is incapable of inducing synchrony. However, cross coupling acts along with self coupling to form mixed coupling and the system exhibits synchrony. The analysis of time series also indicates that, at low magnetic coupling strength, dynamics is square wave bursting. With an increase in magnetic coupling, the dynamics is transformed into plateau bursting. The inability of the cross coupling to induce synchrony is evident in the plateau bursting regime as well. With further increase in magnetic coupling, the system attains an amplitude death state marked by suppressed oscillations. At this state, the magnetic coupling overrides the effect of chemical coupling and the system is synchronised for any interactions *viz.*, self, cross or mixed. The stability of the synchrony attained in self and mixed coupling is justified by the master stability function. The maximum transverse Lyapunov exponent crosses the zero line when the system attains stabilised synchrony. Whereas in cross coupled interactions, stabilised synchrony is never attained. The parameter space gives a better idea about the bifurcation point at which cross coupling makes the influence of self coupling ineffective.

The synchronisation scenario is analysed in a network of HR neurons in ring

topology with self, mixed and cross chemical coupling. The synchrony quantified by the statistical factor of synchronisation justifies the fact that synchrony is unattainable in cross coupling alone and that its effect is nullified in the presence of strong self coupling. The mixed coupling of variables in ring topology along with nonlocal interactions are found to induce chimera and multichimera states in the network. The presence of travelling chimeras in the network is uncovered through the analysis of the spatiotemporal patterns. The Hamilton energy function analysis reveals that to maintain the coherent neurons at high potential, higher energy is utilised. Our findings may help in exploring the collective behaviour of neuronal systems, including physical mechanisms and can be applied to the study of synchronisation in large-scale networks, including multilayer networks.

Chapter 7

Memristive Hindmarsh-Rose neurons with distance-dependent coupling in 2D lattice

7.1 Introduction

Understanding the role of structural and dynamical symmetries in the appearance of distant synchronisation is important for a wide range of applications, including the design and optimisation of communication networks and the understanding of brain function. Traditional single layer networks are limited in their ability to accurately represent complex systems because they only capture one type of interaction or connection [189–191]. By using multilayer models, we can gain a more detailed understanding of the structure and function of the neuronal network and how it changes over time [192]. Multilayer networks have gained significant attention in recent years because of their potential ability to model real world complex systems with multiple levels of connectivity [193]. Majhi *et al.* used a three layer network model to study the role of indirect connections in the emergence of a chimera state in the uncoupled layer [182]. Spatial chimeras were obtained in locally coupled neural network with a topology of cubic lattice [155]. Studies have shown that the evolution of functional network topology with

different layers can have a significant impact on the processing of visual information and other cognitive tasks. For example, research has demonstrated that the intralayer interaction (interactions within a single layer) can play a critical role in the processing of visual information [194].

In the case of a triplex network with a ring topology, the outer layers can synchronise through the intermediate middle layer [195]. Studies have shown that bounded noise can have a significant impact on the formation and instability of spiral waves in a 2D lattice of neurons. It can either enhance or suppress the formation of spiral waves, depending on the strength and type of noise [196]. The significant impact of time delay on the contrast behaviour of each layer in a three layer is also reported [197]. A study has been conducted on two dimensional array of neuron models represented by Rulkov maps with the coupling between neurons arranged in a square shape, but without distance dependence [34].

In this chapter, the synchronisation behaviour and pattern formations of memristive HR network in 2D lattice with distance-dependent chemical coupling are analysed. The studies are carried out by varying the number of connections to each neuron and altering the strength of distance dependence in coupling. The network model is presented in section 7.2. Section 7.3 analyses the synchrony pattern between and within 1D arrays. The dependence of synchrony on coordination number is found out in section 7.3.1, whereas section 7.3.2 is devoted to the analysis of the stability of the network's synchronised states using the Lyapunov stability theory. Section 7.4 exhibits the interesting spatiotemporal patterns and snapshots arising naturally in the arrays of the network. Section 7.5 summarises the results of the chapter.

7.2 HR network in 2D lattice

The network consists of Hindmarsh-Rose neurons, evenly arranged in a 2D lattice made up of five linear chains. The position of each neuron is identified by its indices i, j , where i denotes the position along the X-axis and j denotes the position along the Y-axis. n is the number of neurons present in each 1D array

and N represents the total number of neurons in the network, which is equal to $5n$. The model is given as:

$$\begin{aligned}
\dot{x}_{i,j} &= y_{i,j} - ax_{i,j}^3 + bx_{i,j}^2 - z_{i,j} + I - k_1\rho(\phi_{i,j})x_{i,j} + T_{i,j}, \\
\dot{y}_{i,j} &= c - dx_{i,j}^2 - y_{i,j}, \\
\dot{z}_{i,j} &= r(s(x_{i,j} - x_e) - z_{i,j}), \\
\dot{\phi}_{i,j} &= k_2x_{i,j} - k_3\phi_{i,j}, \quad i = 1, 2, \dots, n; j = 1, 2, \dots, 5.
\end{aligned} \tag{7.1}$$

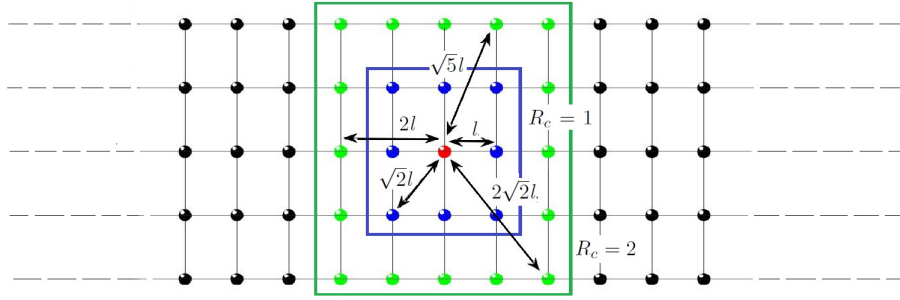


Figure 7.1: Scheme of coupling between the reference neuron (red) and its neighbours, for coupling range $R_c = 2$. The blue balls represent the neurons in the first square and green balls show the neurons in the next square.

Where $x_{i,j}$, $y_{i,j}$ and $z_{i,j}$ represent the membrane potential, spiking variable and bursting variable of the neuron in the (i, j) th position in the 2D lattice, respectively. n is the number of neurons in each array of the network. The external current, I , controls the qualitative behaviour of the neurons. $\phi_{i,j}$ describes the magnetic flux across the membrane, $k_1\rho(\phi_{i,j})x_{i,j}$ denotes induction current and k_1 is induction coefficient [21, 22]. The term $\rho(\phi_{i,j})$ is the memory conductance of a magnetic flux controlled memristor, which can take different forms. We have considered a hyperbolic function, $\tanh(\phi_{i,j})$, whose state equation can be represented by linear terms [170].

The term $T_{i,j}$ represents the nonlinear chemical connections between the neurons. The coupling scheme is as shown in fig. 7.1. The coupling range, R_c , is used to explain the coordination number for the neurons. When $R_c = 1$, each neuron (using the red ball as a reference) is coupled to the neurons in the first nearest square (represented by the blue balls in the figure). The coordination

number in this case is eight, with four neurons at a distance of l and the remaining four at a distance of $\sqrt{2}l$, where l is the lattice parameter. Then the coupling term has the form:

$$T_{i,j} = \frac{g}{8}(v - x_{i,j}) \left[\frac{1}{l^\alpha} [\Gamma(x_{i-1,j}) + \Gamma(x_{i+1,j}) + \Gamma(x_{i,j-1}) + \Gamma(x_{i,j+1})] + \frac{1}{(\sqrt{2}l)^\alpha} [\Gamma(x_{j-1,i-1}) + \Gamma(x_{j-1,i+1}) + \Gamma(x_{j+1,i-1}) + \Gamma(x_{j+1,i+1})] \right]. \quad (7.2)$$

Where g is the coupling constant that represents the magnitude of the interaction between the neurons. The reversal potential v is so chosen that the coupling is always excitatory in nature. An exponential function which models the synaptic junction between the neurons is given by:

$$\Gamma(x_{i,j}) = 1/(1 + \exp(-\lambda(x_{i,j} - \theta))) \quad (7.3)$$

The parameters λ and θ represent the slope of the sigmoidal function and the synaptic firing threshold, respectively.

When $R_c = 2$, each neuron is coupled with neurons in the next square along with the first nearest square (blue and green balls as in fig. 7.1). The coordination number for the second square alone is sixteen with four neurons at a distance of $2l$, four neurons being at $2\sqrt{2}l$ and eight situated at a distance of $\sqrt{5}l$. The coupling term is of the form:

$$T_{i,j} = \frac{g}{16}(v - x_{i,j}) \left[\frac{1}{(2l)^\alpha} [\Gamma(x_{i+2,j}) + \Gamma(x_{i-2,j}) + \Gamma(x_{i,j+2}) + \Gamma(x_{i,j-2})] + \frac{1}{(2\sqrt{2}l)^\alpha} [\Gamma(x_{i+2,j+2}) + \Gamma(x_{i+2,j-2}) + \Gamma(x_{i-2,j+2}) + \Gamma(x_{i-2,j-2})] + \frac{1}{(\sqrt{5}l)^\alpha} [\Gamma(x_{i+1,j-2}) + \Gamma(x_{i+1,j+2}) + \Gamma(x_{i-1,j+2}) + \Gamma(x_{i-1,j-2}) + \Gamma(x_{i+2,j-1}) + \Gamma(x_{i+2,j+1}) + \Gamma(x_{i-2,j+1}) + \Gamma(x_{i-2,j-1})] \right]. \quad (7.4)$$

The lattice parameters $l, \sqrt{2}l, 2l, 2\sqrt{2}l, \sqrt{5}l$ along with the power law exponent,

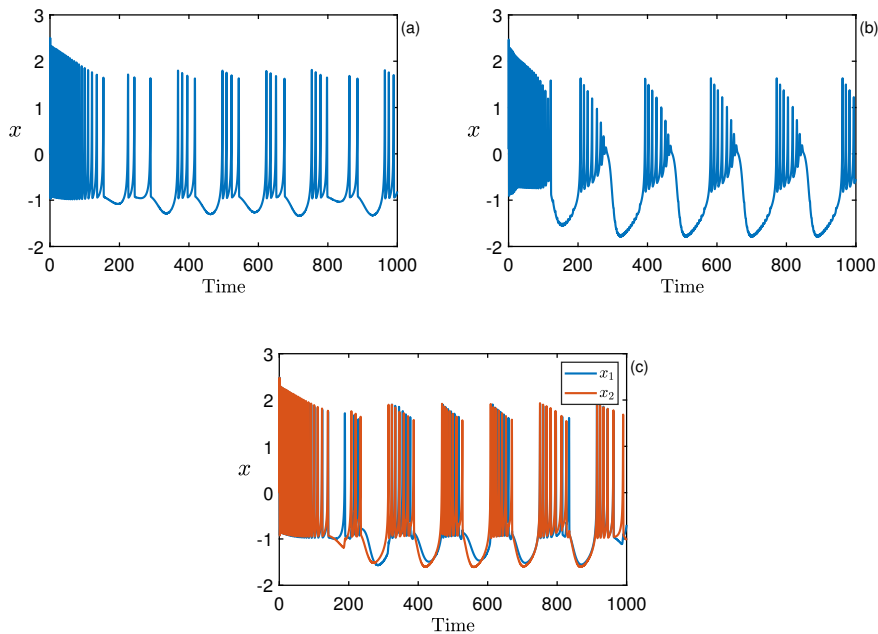


Figure 7.2: Dynamics of HR neuron. (a) uncoupled chaotic bursting ($k_1 = 0, g = 0$), (b) uncoupled plateau bursting ($k_1 = 0.2, g = 0$), (c) coupled chaotic bursting ($k_1 = 0.1, g = 0.2$). Here $I = 3.1$.

α , give a distance dependence to the coupling terms. The ratio of g to lattice parameters ensures that the interaction between neurons decreases with distance. However, this decrease is typically very steep and only the nearest neighbors have a significant contribution. To address this issue, an additional term, α , is introduced which produces a gradual decrease in the interaction strength with distance.

The collective behaviour of the network is analysed by varying the values of g and α , while keeping l as 1. The value of n is set at 100 unless otherwise specified. The initial conditions for each oscillator are taken as $x_{i,j}(0) = 0.001[N - (i + j)]$, $y_{i,j}(0) = 0.002[N - (i + j)]$, $z_{i,j}(0) = 0.003[N - (i + j)]$, $\phi_{i,j}(0) = 0.004[N - (i + j)]$ for $i, j = 1, 2, \dots, n$ [155]. We use the following periodic boundary conditions: $x_{0,j} = x_{n,j}, x_{n+1,j} = x_{1,j}; x_{i,0} = x_{i,n}, x_{i,n+1} = x_{i,1}$. The other parameters are fixed as $a = 3, b = 1, c = 1, d = 5, R = 4, r = 0.006, I = 3.1, x_e = 1.61$ [18], $\lambda = 10, V = 2, \theta = -0.25$ [155], $k_1 = 0.1, k_2 = 0.9, k_3 = 0.4$ [21].

The dynamics of a HR neuron for different system parameters is presented in fig. 7.2. Fig. 7.2(a) shows the chaotic bursting of a single neuron. The system

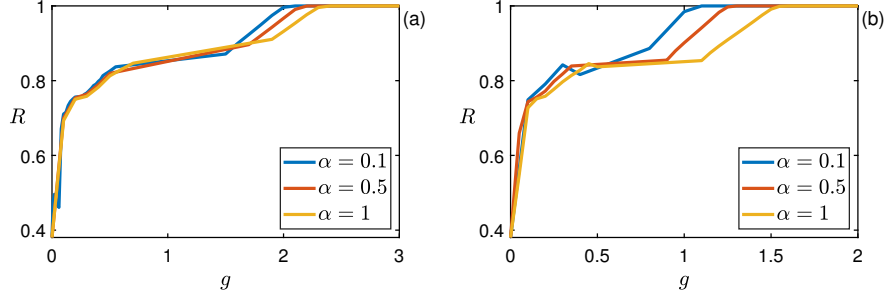


Figure 7.3: Variation of the statistical factor of synchronisation within each 1D array of the 2D lattice network. (a) $R_c = 1$ (b) $R_c = 2$.

exhibits plateau bursting under memristor effects and is presented in fig. 7.2(b). The chaotic bursting of the coupled system under memristor effect and chemical coupling is presented in fig. 7.2(c).

7.3 Synchronisation scenario

In this section, the intra and inter array synchronisation in 1D arrays of the 2D lattice is analysed for different values of α and k (by changing R_c). The intra array synchrony is quantified using the statistical factor of synchronisation, R , based on the mean field theory. The synchrony within each 1D array is calculated using Eq. (1.3). Then it is averaged over the number of arrays.

The pattern of synchrony is analysed in the network with $R_c = 1$ and is shown in fig. 7.3(a). With increase in the value of α , the threshold for coupling also increases. On the other hand, when $R_c = 2$, each neuron is connected to 24 neighboring neurons, forming two squares of neurons surrounding it as shown in fig. 7.3(b). As the value of α increases, the coupling strength at which synchrony is attained also increases. The network in which neurons are coupled to a larger number of neurons is found to synchronise at a faster rate.

The synchrony between the arrays are evaluated using the formula [195]:

$$E_{ij} = \lim_{T \rightarrow \infty} \frac{1}{nT} \int_0^T \sum_{k=1}^n \|\mathbf{X}_k^i(t) - \mathbf{X}_k^j(t)\| dt \quad (7.5)$$

where $\|\cdot\|$ is the Euclidean norm and $i, j = 1, 2, \dots, 5$ denote the array number.

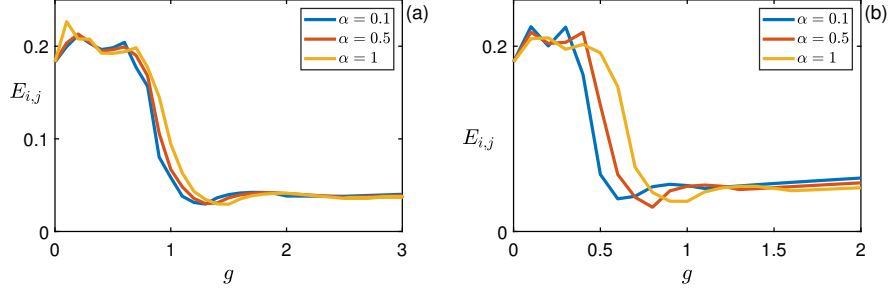


Figure 7.4: Variation of the inter array error between the 1D arrays of the 2D lattice network. (a) $R_c = 1$ (b) $R_c = 2$.

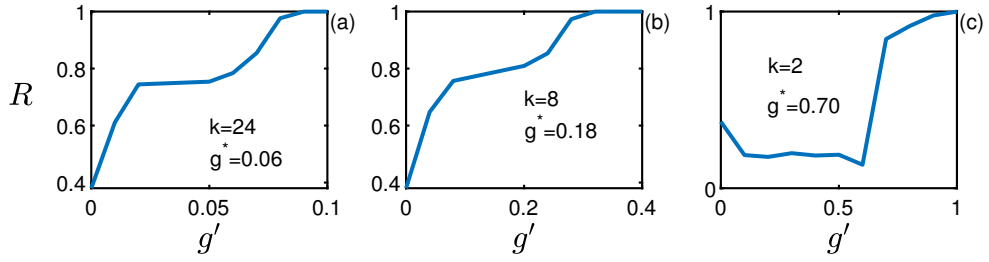


Figure 7.5: Variation of the statistical factor of synchronisation with coupling threshold for different coordination number. (a) $k = 24$, (b) $k = 8$, (c) $k = 2$.

$\mathbf{X}_k^i(t)$ represents the variables x, y, z and ϕ of k th neuron in i th array, at time t . The differences between all the arrays are then averaged to obtain the value of E_{ij} . A low value of E_{ij} represents synchrony between the arrays, while a high value corresponds to lack of synchrony.

The error between the arrays of the network at $R_c = 1$ is shown in fig. 7.4(a). It is observed that for low values of g , the error between the arrays is high, indicating low levels of synchrony. As the value of g increases, the network achieves inter array synchrony. However, even at high values of coupling strength between the arrays, the error is not completely eliminated, suggesting that the different arrays are stabilised at slightly different potential levels.

The synchrony between the 1D arrays in the network with $R_c = 2$ is shown in fig. 7.4(b). The synchrony between arrays is visible from this plot as well. The synchrony is obtained at lower value of g compared to the network with $R_c = 1$.

7.3.1 Coordination number and synchrony

The dependence of synchrony on the coordination number of the neurons is analysed in this section. The synchrony pattern is analysed using the statistical factor of synchronisation. The variation of R with g is analysed. It has been already reported that in a chemically coupled network, the synchronisation threshold is given by $g^* = g_{(n=2)}/k$, where, $g_{(n=2)}$ is the constant corresponding to the synchronisation coupling threshold between two mutually coupled HR neurons and k is the coordination number *i. e.*, the number of neurons to which each neuron is coupled [30]. The value of $g_{(n=2)}$ is numerically found to be 1.402. The variation of R is analysed for different values of k and is plotted in fig. 7.5. The quantity $g' = g/k$ is plotted on the X-axis. The coordination number and theoretically calculated g^* are presented in the legend. In fig. 7.5(a), the variation of R is presented for the network with $R_c = 2$. Thus, the coordination number is 24. The expected threshold g^* obtained theoretically is 0.06 and numerically we have obtained it as 0.08. The coupling threshold for a network with $R_c = 1$, the coordination number being 8, is theoretically obtained as 0.18, which is related to the numerical value 0.3, within permissible error. This is shown in fig. 7.5(b). The synchrony pattern in the network with $R_c = 1$ and fixing j is shown in fig. 7.5(c). The coordination number is 2 and the calculated coupling threshold is 0.7, which corresponds to the numerically obtained value of 0.9.

7.3.2 Network size and stability of synchrony

In this section, we have analysed the dependence of synchrony on the network size. The synchrony in the network is quantified using R , given by Eq. (1.3). The variation of R with g for different values of n is presented in fig. 7.6(a). The network attains synchrony at $g = 1.5$, irrespective of the size of the network. The master stability approach is used to analyse the stability of the synchronised states. It was developed by Louis M. Pecora and Thomas L. Carroll in the 1990s and it has become a widely used tool in the study of synchronisation phenomena in a variety of contexts [74]. Later the theory was developed by

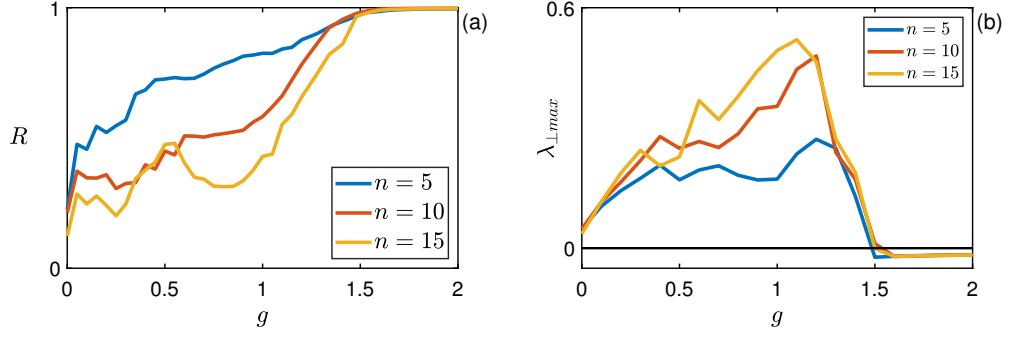


Figure 7.6: Variation of (a) statistical factor of synchronisation and (b) maximum transverse Lyapunov exponent with coupling strength for different network size.

Dhamala *et al.* and was utilised to find the transition to synchrony in various networks with different couplings and topologies [174, 198]. Researchers continue to rely on the master stability function to quantify the stability of systems [161, 180]. The stability of the system has been analysed by fixing $j = j'$, $R_c = 1$. The error dynamical equations are calculated by considering the first neuron as the reference and finding the difference of each oscillator from the first neuron. At the synchronised state $(x_{1,j'}, y_{1,j'}, z_{1,j'}, \phi_{1,j'}) = (x_{2,j'}, y_{2,j'}, z_{2,j'}, \phi_{2,j'}) = \dots = (x_{n,j'}, y_{n,j'}, z_{n,j'}, \phi_{n,j'})$ and the error terms defined as $x_{\perp i,j'} = x_{i,j'} - x_{1,j'}$, $y_{\perp i,j'} = y_{i,j'} - y_{1,j'}$, $z_{\perp i,j'} = z_{i,j'} - z_{1,j'}$, $\phi_{\perp i,j'} = \phi_{i,j'} - \phi_{1,j'}$, where $i = 2, 3, \dots, n$ vanish in the limit of $t \rightarrow \infty$ and a synchronous solution exist. The stability equations for perturbations transverse to the synchronisation manifold are expressed as:

$$\begin{aligned} \dot{x}_{\perp i,j'} = & y_{\perp i,j'} - 3ax_{i,j'}^2 x_{\perp i,j'} + 2bx_{i,j'} x_{\perp i,j'} - z_{\perp i,j'} - k1 \left[\tanh(\phi_{i,j'}) x_{i,j'} \right. \\ & \left. + \tanh(\phi_{1,j'}) x_{1,j'} \right] + \frac{g}{2} \left[(v - x_{i,j'}) (\Gamma(x_{i+1,j'}) + \Gamma(x_{i-1,j'})) - \right. \\ & \left. (v - x_{1,j'}) (\Gamma(x_{2,j'}) + \Gamma(x_{n,j'})) \right] \end{aligned} \quad (7.6)$$

$$\dot{y}_{\perp i,j'} = -2dx_{i,j'} - y_{\perp i,j'},$$

$$\dot{z}_{\perp i,j'} = rsx_{\perp i,j'} - z_{\perp i,j'},$$

$$\dot{\phi}_{\perp i,j'} = k_2 x_{\perp i,j'} - k_3 \phi_{\perp i,j'}.$$

On simplifying,

$$\begin{aligned}
\dot{x}_{\perp i,j'} &= y_{\perp i,j'} - 3ax_{i,j'}^2 x_{\perp i,j'} + 2bx_{i,j'} x_{\perp i,j'} - z_{\perp i,j'} - k_1(x_{i+1,j'} \phi_{\perp i,j'} + \phi_{i,j'} x_{\perp i,j'}) - \\
&\quad \frac{g}{2} \Omega(x_{i,j'}) x_{\perp i,j'} \\
\dot{y}_{\perp i,j'} &= -2dx_{i,j'} - y_{\perp i,j'}, \\
\dot{z}_{\perp i,j'} &= rsx_{\perp i,j'} - z_{\perp i,j'}, \\
\dot{\phi}_{\perp i,j'} &= k_2 x_{\perp i,j'} - k_3 \phi_{\perp i,j'}.
\end{aligned} \tag{7.7}$$

Where, $\tanh(\phi_{i,j'})x_{i,j'} + \tanh(\phi_{1,j'})x_{1,j'}$ is approximated as $x_{i+1,j'}\phi_{\perp i,j'} + \phi_{i,j'}x_{\perp i,j'}$ and $\Omega(x_{i,j'}) = g(1/(1 + \exp(-\lambda(x_{i,j'} - \theta)))) + g(v - x_{i,j'})(-\lambda(x_{i,j'} - \theta))/(((1 + \exp(-\lambda(x_{i,j'} - \theta))))^2)$

The Jacobian for the whole network with chemical coupling will have the following structure:

$$\begin{bmatrix}
J_{1,1} + \gamma_{1,1}E & \gamma_{1,2}E & 0 & 0 & \cdots & 0 & \gamma_{1,n}E \\
\gamma_{2,1}E & J_{2,2} + \gamma_{2,2}E & \gamma_{2,3}E & 0 & \cdots & 0 & 0 \\
0 & \gamma_{3,2}E & J_{3,3} + \gamma_{3,3}E & \gamma_{3,4}E & \cdots & 0 & 0 \\
\vdots & \vdots & \vdots & \vdots & \vdots & \vdots & \vdots \\
\gamma_{n,1}E & 0 & 0 & 0 & \cdots & \gamma_{n,n-1}E & J_{n,n} + \gamma_{n,n}E
\end{bmatrix}, \tag{7.8}$$

where

$$J_{i,i} = \begin{pmatrix}
2ax_i - 3bx_i^2 - k_1\phi_i + \Omega(x_i) & 1 & -1 & -k_1x_i \\
-2dx_i & -1 & 0 & 0 \\
rs & 0 & -r & 0 \\
k_2 & 0 & 0 & -k_3
\end{pmatrix} \tag{7.9}$$

and

$$E = \begin{pmatrix} 1 & 0 & 0 & 0 \\ 0 & 0 & 0 & 0 \\ 0 & 0 & 0 & 0 \\ 0 & 0 & 0 & 0 \end{pmatrix} \quad (7.10)$$

The terms $\gamma_{i,i}$ and $\gamma_{i,j}$ is obtained by partially differentiating $\frac{g}{2}(v-x_i)[\Gamma(x_{i+1} + \Gamma(x_{i-1}))]$ with respect to x_i and x_j , respectively. The Jacobian given by Eq. (7.8) is diagonalised in a coordinate system that isolates the stability of the synchronisation manifold from the transverse directions. The Maximum Transverse Lyapunov Exponent (MTLE), $\lambda_{\perp max}$ is used as the bifurcation function to study the stability of synchrony. The system is stabilised when MTLE becomes negative. The variation of $\lambda_{\perp max}$ with g for different values of n is presented in fig. 7.6(b). The MTLE crosses the zero line for $g = 1.5$, irrespective of the value of n . It is justified that the stability of synchronised states in chemically coupled networks is independent of the network size [30].

7.4 Spatiotemporal patterns

This section presents the different spatiotemporal patterns in the 2D lattice network with distance-dependent coupling. All the neurons in the network show bursting dynamics for $g = 0.1$, as shown in fig. 7.7(a). The dynamics of a single neuron from each array shown in fig. 7.7(b) justifies the result. Two arrays exhibit amplitude death and the other three arrays show bursting dynamics, as shown in fig. 7.7(c). The corresponding dynamics of a single neuron is presented in fig. 7.7(d). All the arrays in the network show amplitude death, as shown in fig. 7.7(e) which is justified by the time series of a single neuron from each array as shown in fig. 7.7(f).

The 1D arrays of the network exhibit contrasting behaviour for weak coupling and synchrony with each other when coupling is strong. The contrast behaviors of each 1D array for different coupling strengths and power law exponent factors are shown in fig. 7.8. The network shows perfect synchrony in the first array and

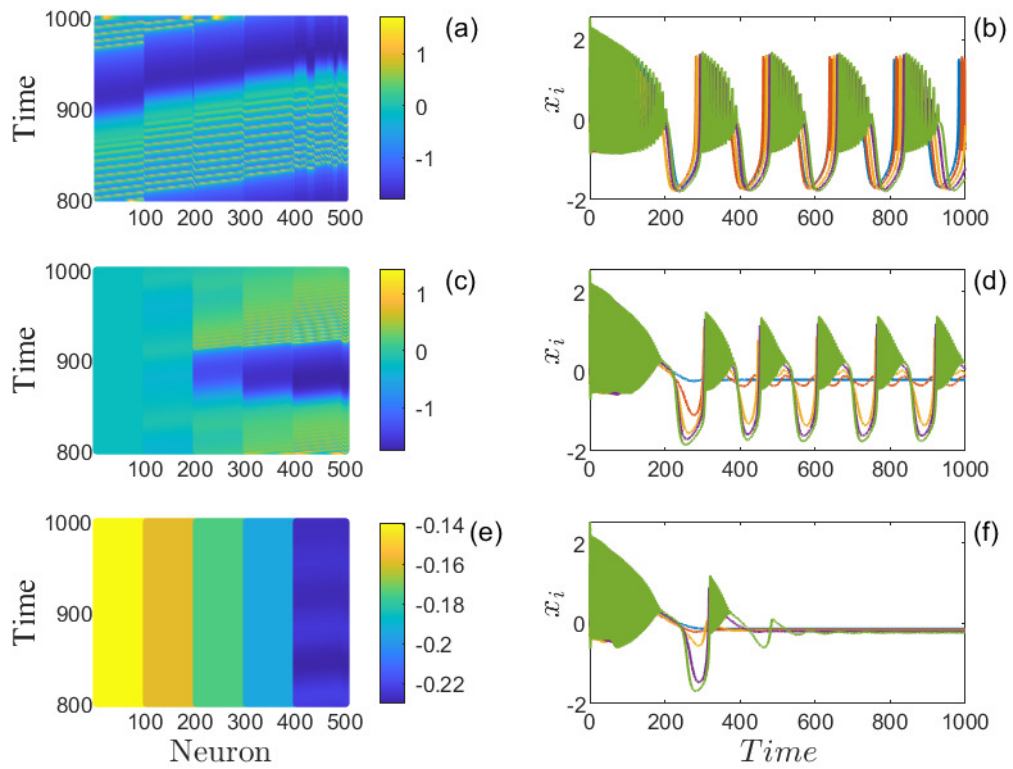


Figure 7.7: Spatiotemporal evaluation of membrane potential. (a) bursting ($g = 0.1$), (c) mixed behaviour of bursting and amplitude death ($g = 0.4$) and (e) amplitude death ($g = 0.48$). The dynamics of the neuron from each layer is represented in the right panel, (b), (d) and (f). Here, $\alpha = 0.1$. The colourbar represents the membrane potential, x .

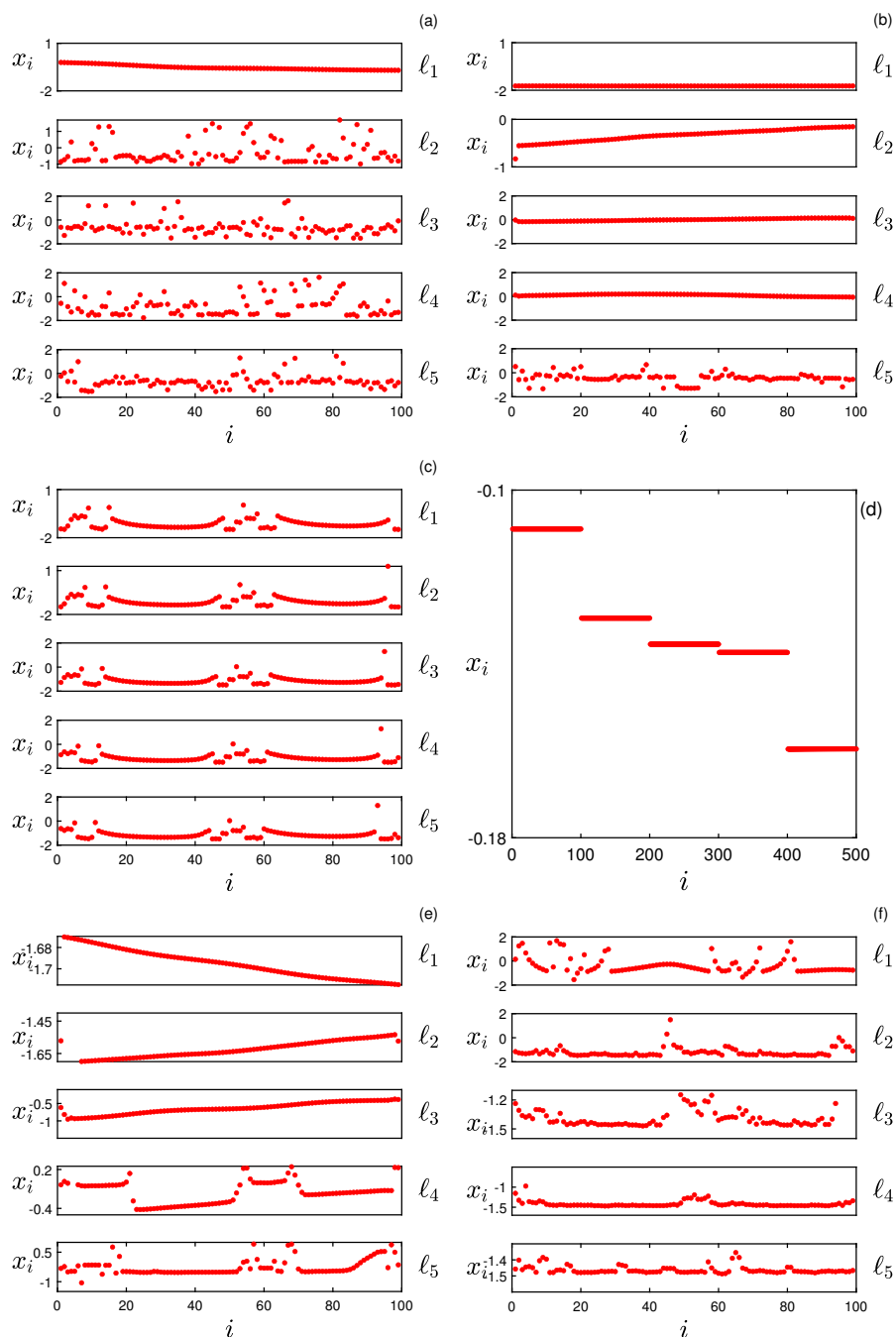


Figure 7.8: Snapshots of the different 1D arrays of the network. (a) $\alpha = 0.1, g = 0.05, R_c = 1$, (b) $\alpha = 0.1, g = 0.11, R_c = 1$, (c) $\alpha = 0.1, g = 0.05, R_c = 1$, (d) $\alpha = 0.1, g = 1, R_c = 1$, (e) $\alpha = 0.1, g = 0.06, R_c = 2$ and (f) $\alpha = 0.5, g = 0.04, R_c = 1$. Here, l_j , where $j = 1, 2, \dots, 5$ represents the different 1D arrays of the lattice.

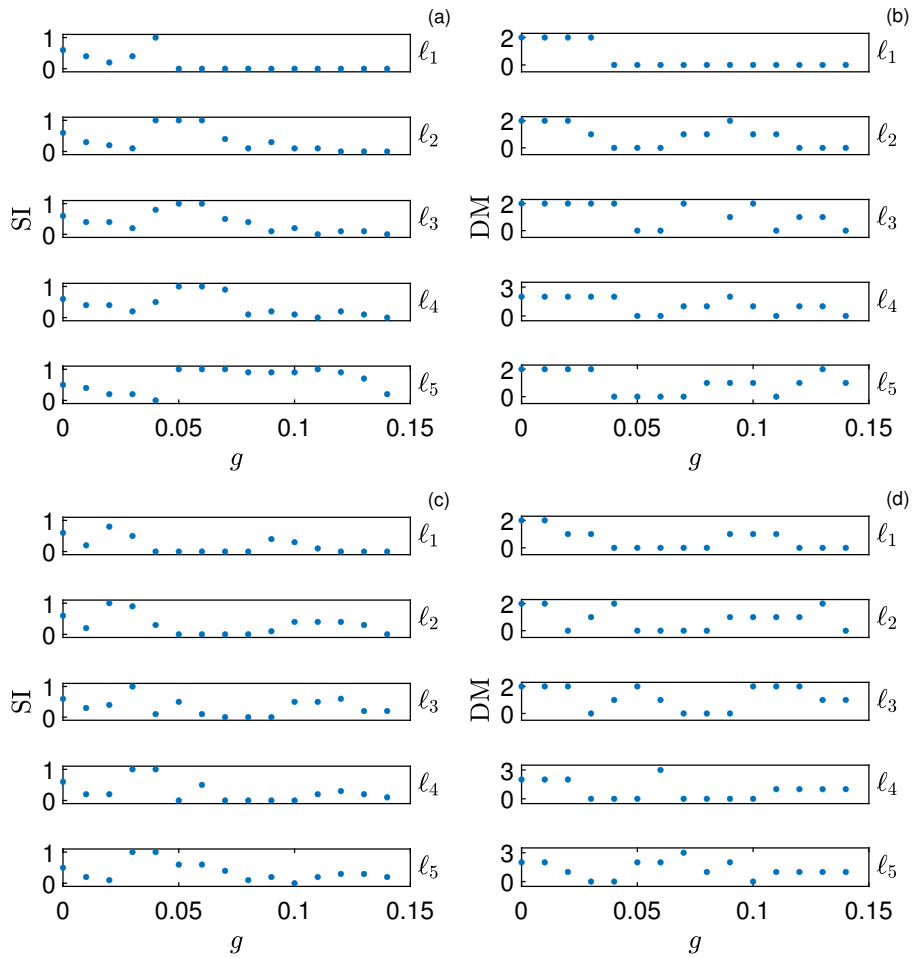


Figure 7.9: Variation of the strength of incoherence and discontinuity measure for different values of coupling strength. (a), (b) $R_c = 1$ and (c),(d) $R_c = 2$. Here, $\alpha = 0.1$. Here, l_j , where $j = 1, 2, \dots, 5$ represents the different 1D arrays of the lattice.

desynchronisation in all the other arrays for $R_c = 1$, as shown in fig. 7.8(a). The fifth array in 7.8(b) is desynchronised, while all other arrays are synchronised. All the arrays show multichimera states for $R_c = 1$, as shown in fig. 7.8(c). The network with $R_c = 1$ shows clustered synchrony, where each array is perfectly synchronised at slightly different membrane potentials, as shown in fig. 7.8(d). First three arrays are synchronised and rest two arrays show multichimera states in the network with $R_c = 2$, which is shown in fig. 7.8(e). First array exhibits multichimera state and the other four arrays are in imperfect synchrony, with $R_c = 1$, as shown in fig. 7.8(f). These results are consistent for networks with higher dimensions as well.

The emergence of chimera and multichimera states in the network due to the topology and distance-dependent coupling is analysed with the help of a quantitative measure called strength of incoherence (SI). The local standard deviation, $\sigma(m)$, has been defined from the time series. The total number of oscillators in a single array is divided into 'M' bins of equal length 'n'' = n/M and the difference dynamical variable is calculated as $\omega_j = x_j - x_{j+1}$. Then the local standard deviation is defined as [76]:

$$\sigma(m) = \left\langle \sqrt{\frac{1}{n'} \sum_{j=n'(m-1)+1}^{mn'} [\omega_j - \langle \omega \rangle]^2} \right\rangle_t, \quad (7.11)$$

where, $m = 1, 2, \dots, M$; $\langle \omega \rangle = \frac{1}{n'} \sum_{i=1}^{n'} \omega_i(t)$. $\langle \dots \rangle_t$ denotes the average over time. The term SI is defined as:

$$SI = 1 - \frac{\sum_{m=1}^M s_m}{M}, \quad s_m = \mathcal{H}(\epsilon - \sigma(m)), \quad (7.12)$$

where \mathcal{H} is the Heaviside step function and ϵ is a predefined threshold. The values of SI are 1, 0 or between 1 and 0, representing incoherent, coherent and chimera or multichimera states, respectively. In order to distinguish chimera from multichimera states, we calculate discontinuity measure (DM) [76], which is defined as:

$$DM = \frac{\sum_{i=1}^M |s_{i+1} - s_i|}{2}, \quad (7.13)$$

where, $s_{M+1} = s_1$. For chimera, $DM = 1$ and for multichimera $2 \leq DM \leq \frac{M}{2}$.

The variation of SI and DM with g , for $R_c = 1$ and $R_c = 2$ is shown in fig. 7.9. The first array exhibits multichimera states for low values of g and coherence at other values. The remaining four arrays display chimera and multichimera states for various values of g , when $R_c = 1$, as shown in fig. 7.9(a) and 7.9(b). When $R_c = 2$, all the five arrays exhibit chimera and multichimera states for different values of g as shown in fig. 7.9(c) and 7.9(d).

7.5 Results and conclusions

In this chapter, we have analysed the influence of distance-dependent chemical connections in a 2D array of modified HR neurons. The synchronisation scenario and pattern formation are studied by altering the coordination number, strength of coupling and distance dependence. The study reveals that as the coordination number increases, the threshold for coupling strength to attain synchrony decreases. The stability of the completely synchronous state in chemically coupled networks depends only on the number of neurons to which each neuron is coupled and is independent of the network size. We have used the Lyapunov function approach to measure the stability of the synchronised states in the network. The network shows low intra and inter array synchrony at low coupling strengths and the synchrony increases with coupling strength. Additionally, the different 1D arrays display unique spatiotemporal patterns, chimeras and clusters for various coupling strengths. The strength of incoherence and the discontinuity measure have been analysed to verify the presence of chimera and multichimera states. The significance of our study is that it focuses on intralayer interaction, which is crucial for visual information processing in the brain. Interlayer synchrony has also been observed in cognitive processes such as perception, memory, and attention.

Chapter 8

Emergence of spatial chimeras in cross coupled network of 2D lattice

8.1 Introduction

The dimensionality of a network refers to the number of nodes and the connections between them, can have a significant impact on the synchronisation behaviour and the emergence of interesting patterns in the network [199]. A single layer of neurons has limitations in terms of its ability to process complex information, whereas lattice topology can perform more complex computations by creating a network of interconnected neurons, which can avoid the limitations of single layer networks. It is important to analyse the synchronisation stability and evolution of collective behaviours like spatial and spiral chimeras, in a spatially coupled network [65, 200–203]. The cross coupling between state variables is an unconventional type of coupling and has been effectively used to induce chimera states in networks [151, 204–206]. The symmetry breaking induced by power law coupling has also been used to produce chimera states [37, 127]. Therefore, the interaction modes, coupling scheme, topology and dimensionality have a significant impact on the dynamical analysis of neuronal networks.

The emergence of spiral wave chimera patterns in a locally coupled ecological network composed of diffusible prey predator species was reported [207]. Spiral

wave chimeras were also obtained in a two dimensional network with nonlocal coupling [208]. Two dimensional spot and stripe chimeras were observed in a network of oscillators arranged in a flat torus topology [209]. The rotation speed of the spiral wave chimeras was calculated using perturbation theory in a network of phase oscillators [210]. A delayed asymmetric synapse coupling was effectively used to suppress spiral waves in a lattice array of coupled neurons [211].

In this chapter, the synchronisation scenario and the emergence of spatial chimeras are analysed in a network of memristive HR neurons with distance-dependent and cross chemical coupling schemes. The model is explained in section 8.2. The synchronisation behaviour of the network is analysed in section 8.3. The interesting patterns obtained are presented in section 8.4. The energy analysis of the network is carried out in section 8.5 and section 8.6 summarises the results of the chapter.

8.2 Chemical cross coupling in 2D lattice

The dynamic equations of the network arranged in a 2D lattice with cross coupling between membrane potential and electromagnetic flux is of the form:

$$\begin{aligned}
\dot{x}_{i,j} &= y_{i,j} - ax_{i,j}^3 + bx_{i,j}^2 - z_{i,j} + I - k_1\rho(\phi_{i,j})x_{i,j} + b_{xx}T_{i,j}^x + b_{x\phi}T_{i,j}^\phi, \\
\dot{y}_{i,j} &= c - dx_{i,j}^2 - y_{i,j}, \\
\dot{z}_{i,j} &= r(s(x_{i,j} - x_e) - z_{i,j}), \\
\dot{\phi}_{i,j} &= k_2x_{i,j} - k_3\phi_{i,j} + b_{\phi x}T_{i,j}^x + b_{\phi\phi}T_{i,j}^\phi, \quad i, j = 1, 2, \dots, n.
\end{aligned} \tag{8.1}$$

Where $x_{i,j}$, $y_{i,j}$ and $z_{i,j}$ represent the membrane potential, spiking variable and bursting variable of neuron in the (i, j) th position in the 2D lattice, respectively. n is the number of neurons in each array of the network. The external current, I , controls the qualitative behaviour of the neurons. The magnetic flux across the membrane is described by $\phi_{i,j}$, the induction current is represented by $k_1\rho(\phi_{i,j})x_{i,j}$ and the induction coefficient is represented by k_1 [21, 22]. The term $\rho(\phi_{i,j})$ is the memory conductance of a magnetic flux controlled memris-

tor, which can take different forms. We have considered a hyperbolic function, $\tanh(\phi_{i,j})$, whose state equation can be represented by the linear terms [170].

The term $T_{i,j}^x$ represents the nonlinear chemical connections between the neurons in x , given by Eqs. 7.2 and 7.4, respectively for $R_c = 1$ and $R_c = 2$. The coordination numbers are 8 and 24 when $R_c = 1$ and $R_c = 2$, respectively. The chemical coupling term in ϕ is given by:

$$T_{i,j}^\phi = \frac{g}{8}(v - \phi_{i,j}) \left[\frac{1}{l^\alpha} [\Gamma(\phi_{i-1,j}) + \Gamma(\phi_{i+1,j}) + \Gamma(\phi_{i,j-1}) + \Gamma(\phi_{i,j+1})] + \frac{1}{(\sqrt{2}l)^\alpha} [\Gamma(\phi_{j-1,i-1}) + \Gamma(\phi_{j-1,i+1}) + \Gamma(\phi_{j+1,i-1}) + \Gamma(\phi_{j+1,i+1})] \right]. \quad (8.2)$$

Where g is the coupling constant that represents the magnitude of the interaction between the neurons. The reversal potential v is so chosen that the coupling is always excitatory in nature. The exponential function that models the chemical coupling is given as:

$$\Gamma(\phi_{i,j}) = 1/(1 + \exp(-\lambda(\phi_{i,j} - \theta))) \quad (8.3)$$

The parameters λ and θ represent the slope of the sigmoidal function and the synaptic firing threshold, respectively. The coupling term for $R_c = 2$ is of the form:

$$T_{i,j}^\phi = \frac{g}{16} \left[\frac{1}{(2l)^\alpha} [\Gamma(\phi_{i+2,j}) + \Gamma(\phi_{i-2,j}) + \Gamma(\phi_{i,j+2}) + \Gamma(\phi_{i,j-2})] + \frac{1}{(2\sqrt{2}l)^\alpha} [\Gamma(\phi_{i+2,j+2}) + \Gamma(\phi_{i+2,j-2}) + \Gamma(\phi_{i-2,j+2}) + \Gamma(\phi_{i-2,j-2})] + \frac{1}{(\sqrt{5}l)^\alpha} [\Gamma(\phi_{i_1,j-2}) + \Gamma(\phi_{i+1,j+2}) + \Gamma(\phi_{i-1,j+2}) + \Gamma(\phi_{i-1,j-2}) + \Gamma(\phi_{i+2,j-1}) + \Gamma(\phi_{i+2,j+1}) + \Gamma(\phi_{i-2,j+1}) + \Gamma(\phi_{i-2,j-1})] \right]. \quad (8.4)$$

The lattice parameters $l, \sqrt{2}l, 2l, 2\sqrt{2}l, \sqrt{5}l$ give a distance dependence to the

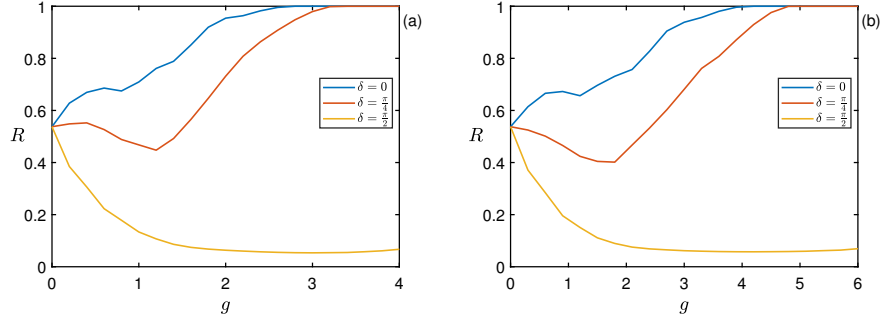


Figure 8.1: Variation of the statistical factor of synchronisation (R) with coupling constant (g) for different values of coupling phase (δ).

coupling terms. The elements b_{xx} , $b_{x\phi}$, $b_{\phi x}$ and $b_{\phi\phi}$ form the components of a coupling matrix. A general form for this coupling matrix which incorporates self and cross coupling is given by:

$$B = \begin{pmatrix} b_{xx} & b_{x\phi} \\ b_{\phi x} & b_{\phi\phi} \end{pmatrix} = \begin{pmatrix} \cos \delta & \sin \delta \\ -\sin \delta & \cos \delta \end{pmatrix} \quad (8.5)$$

Where $\delta \in [-\pi, \pi)$ is the coupling phase. The switching between the interactions is made easy by varying the values of δ . We have analysed the system of HR neurons in three different cases:

- (i) Self coupling in x and ϕ , $\delta = 0$.
- (ii) Mixed coupling in x and ϕ , $\delta = \frac{\pi}{4}$.
- (iii) Cross coupling in x and ϕ , $\delta = \frac{\pi}{2}$.

8.3 The synchronisation scenario

The synchronisation scenario in the presence of cross coupling of variables in magnetically coupled HR neurons in 2D lattice has been analysed in this section. The lattice has dimensions of $N = n * n$, where $n = 40$ and $N = 1600$. The amount of synchrony is quantified using the statistical factor of synchronisation, R , given by the equation, Eq. (1.3).

The relation between coordination number and coupling threshold to attain

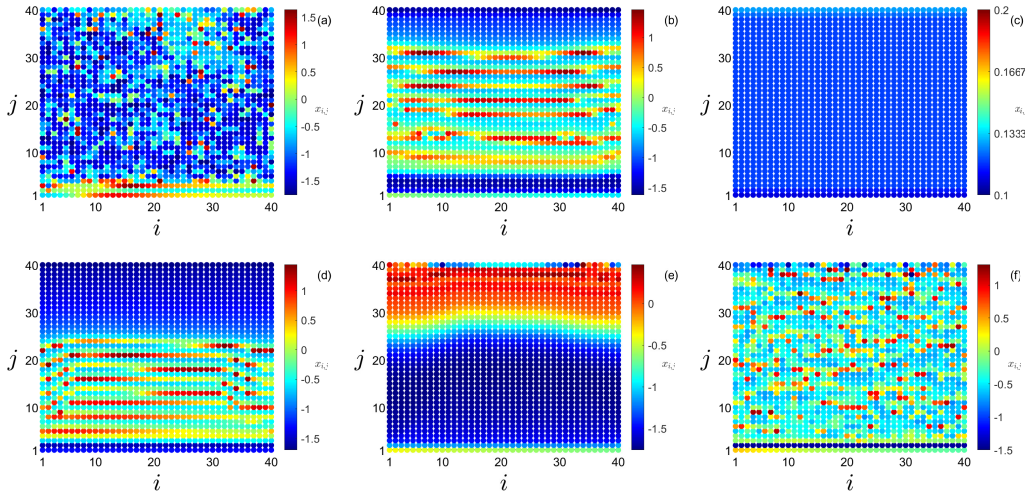


Figure 8.2: Snapshots of membrane potential. (a) desynchrony, $g = 0.1$, $\delta = \frac{\pi}{4}, R_c = 2$, (b) chimera, $g = 0.5$, $\delta = \frac{\pi}{4}, R_c = 2$, (c) synchrony $g = 0.4$, $\delta = \frac{\pi}{4}, R_c = 1$, (d) chimera, $g = 0.3$, $\delta = \frac{\pi}{4}, R_c = 2$ (e) patched synchrony $g = 0.9$, $\delta = \frac{\pi}{4}, R_c = 2$ (f) $g = 0.9$, $\delta = \frac{\pi}{2}, R_c = 1$. The colourbar represents the membrane potential, x .

synchrony is determined by analysing the variation of R with g . The variations in R with g for $R_c = 1$ are shown in fig. 8.1(a). For self ($\delta = 0$) and mixed ($\delta = \frac{\pi}{4}$) interactions, synchrony is obtained at $g \approx 3$, but for cross coupling ($\delta = \frac{\pi}{2}$) synchrony is never obtained. For $R_c = 2$, the synchrony is obtained at $g = 4$, for self coupling, as shown in fig. 8.1(b). For mixed coupling, synchrony is obtained at $g \approx 5$. The synchrony is never obtained for cross coupling.

8.4 Emergence of spatial chimeras

The topology, distance dependent non linear coupling and cross interactions lead to emergence of interesting spatial chimeras in the network. The snapshots of the variable x at particular time t (here, 1000 units) of the neurons in the 2D lattice is presented in fig. 8.2. The incoherent system is shown in fig. 8.2 (a). The spatial chimera emerging in the network is presented in figs. 8.2 (b). The completely synchronised state is shown in fig. 8.2 (c). Fig. 8.2 (d) presents a spatial chimera. Patched synchrony is shown in fig. 8.2 (e). Incoherent state for cross coupling is presented in fig. 8.2 (f).

The travelling chimera exhibited by the network with $g = 0.5$, $\delta = \frac{\pi}{4}, R_c = 2$

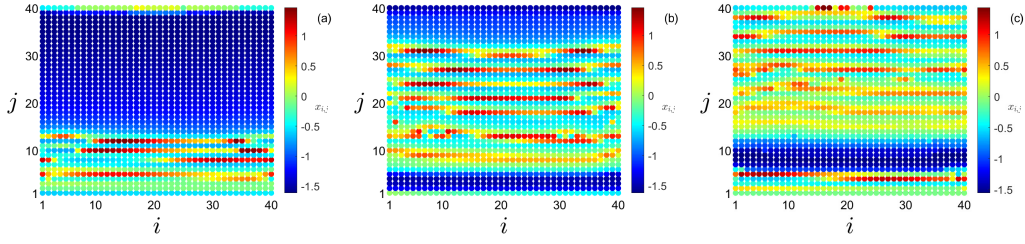


Figure 8.3: Snapshots of membrane potential. $g = 0.5$, $\delta = \frac{\pi}{4}$, $R_c = 2$. (a) $t = 800$, (b) $t = 1000$ and (c) $t = 1200$. The colourbar represents the membrane potential, x .

is shown in fig. 8.3. Figs. 8.3 (a), (b) and (c), represent the travelling spatial chimeras obtained for $t = 800, 1000$ and 1200 , respectively.

8.5 Energy aspects

The energy analysis provides insight into the internal behavior of the oscillators under study. Sarasola et al. have proposed the mathematical formalism for the energy functions for well known chaotic systems. This method is used to analyse the energy of the oscillators of the 2D lattice. Using Helmholtz theorem, the speed vector is decomposed in to conservative and dissipative part. Then according to Eq. [21, 87], the Hamilton energy corresponding to the system will satisfy the following partial differential equation :

$$(y - z + I - \phi) \frac{\partial H_{i,j}}{\partial x_{i,j}} + (1 - bx_{i,j}^2) \frac{\partial H_{i,j}}{\partial i,j} + rR(x_{i,j} - x_e) \frac{\partial H_{i,j}}{\partial z_{i,j}} + k_2 x_{i,j} \frac{\partial H_{i,j}}{\partial \phi_{i,j}} = 0 \quad (8.6)$$

A general solution for the above equation is of the form

$$H = \frac{2}{3}bx_{i,j}^3 - 2x_{i,j} + rR(x_{i,j} - x_e)^2 + (y_{i,j} - z_{i,j} + I - \phi_{i,j})^2 + k_2x_{i,j}^2 \quad (8.7)$$

The energy function of the system is calculated for the values of the parameters corresponding to fig. 8.2, using the eqn. 8.7 and is presented in fig. 8.4. Fig. 8.4(a) shows the values of the energy function, for an incoherent network. The energy pattern for the spatial chimera state is shown in fig. 8.2(b). The energy of

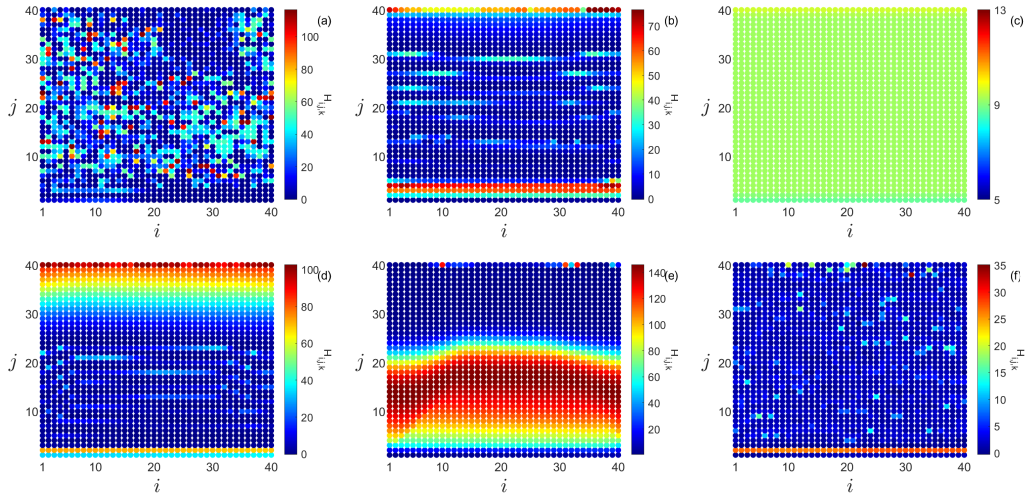


Figure 8.4: Snapshots of Hamilton energy function. (a) $g = 0.1$, $\delta = \frac{\pi}{4}$, $R_c = 2$, (b) $g = 0.5$, $\delta = \frac{\pi}{4}$, $R_c = 2$, (c) $g = 0.4$, $\delta = \frac{\pi}{4}$, $R_c = 1$, (d) $g = 0.3$, $\delta = \frac{\pi}{4}$, $R_c = 2$ (e) $g = 0.9$, $\delta = \frac{\pi}{4}$, $R_c = 2$ (f) $g = 0.9$, $\delta = \frac{\pi}{2}$, $R_c = 1$. The colourbar represents the energy function, H .

the incoherent region is found to be low compared to the coherent region. When the system is in completely synchronised state, the energy of the system is found to be uniform. In fig. 8.2(d) also, the energy of the incoherent system is found to be low. The energy plot corresponding to the clustered synchrony as shown in fig. 8.2(e) indicates that the energy of the system is high if the potential of the neurons are maintained at high potential irrespective of the polarity of the membrane potential. The energy of the neurons in incoherent state, shown in fig. 8.2(f), is low compared to the system in fig. 8.2(a). The majority of the neurons are maintained at high negative potential in the system as shown in the fig. 8.2(a), compared to the system in fig. 8.2(f). Thus, the energy of the neurons is low when the membrane potential is nearly zero. The system requires high energy to maintain at a higher potential regardless of the polarity.

8.6 Results and conclusions

The synchronisation behavior and emergence of spatial chimeras are analysed in a network of memristive HR neurons with nonlinear chemical cross-coupling arranged in a 2D lattice topology. Self and mixed interactions induces both synchrony and chimera states, whereas cross interactions are incapable of inducing

either. These results are consistent for different coordination numbers. The time series analysis indicates that the spatial chimeras are travelling in nature. The energy analysis points out that the system requires high energy to maintain a high membrane potential regardless of the polarity.

Chapter 9

Conclusions and future prospects

9.1 Summary

This thesis presents the study of the influences of external stimuli, synaptic connections, coupling schemes and topology in inducing synchrony, desynchrony and chimera states in the Hindmarsh-Rose networks. The first chapter explains the basic concepts and terminologies used in this thesis. The work in the thesis has been presented in next seven chapters. The results are summarised and future prospects are presented in the ninth chapter.

- The phase synchrony in the HR network with mean field coupling and its control using external stimuli are analysed in linear chain topology. The high frequency input with optimum amplitude and pulse width is found to have better desynchronising ability. The synchrony and variations in IBI are quantified using the Kuramoto order parameter and the coefficient of variability. The mean field coupled HR network is also analysed with an exponentially decaying coupling strength. The synchrony is found to decrease with an increase in the decay constant. The decaying coupling scheme induces chimera states in the network. The chimeras are quantified using the strength of incoherence.
- The mean field coupled network is analysed under the influence of distance-dependent coupling governed by a power law exponent in ring topology.

The network is studied in global, non local and local interactions. The synchrony in the network is quantified using the statistical factor of synchronisation. The synchronisation behaviour is verified through error analysis as well. The uniform global interaction induces incoherent, imperfect synchrony and synchronised states. The distance-dependent field coupling induces chimera states in globally coupled network, which is a rare phenomenon. Even though chimera states are reported in nonlocal interactions, the influence of distance-dependent coupling enhances the emergence of chimera states. Chimera states in local or nearest neighbour coupling are also very difficult to obtain. The initial conditions are modified to obtain travelling chimeras in the network with local coupling.

- The synchronisation scenario and pattern formations in the HR network coupled by a rotation matrix that helps to realise different coupling schemes such as self, mixed and cross interactions by varying the coupling phase have been analysed. In two coupled system, in-phase and anti-phase oscillations are obtained for the activator and inhibitor modes of electrical coupling, respectively. When the off diagonal elements of the matrix are zero, the system shows self coupling of the three variables, which helps to attain synchrony faster. The off diagonal elements give cross interactions between the variables, which reduces synchrony. The stability of the synchrony attained is analysed using Lyapunov function approach. The self coupling in three variables is sufficient to induce chimera states in nonlocal coupling. The strength of incoherence and discontinuity measure validate the existence of chimera and multichimera states. The inhibitor self coupling in local interaction induces interesting patterns like Mixed Oscillatory State and clusters. In a nonlocally coupled network, chimeras, multichimeras, travelling chimeras, MOS and clusters are obtained.
- The HR network has been modified with distance-dependent memristor and mean field couplings. Memristors are used to represent the electromagnetic effects. The changes in firing patterns and the collective behaviour

due to the memristor effect are studied using the mean field approach in linear chain topology. The network with memristor effects is analysed under the influence of constant and time varying inputs. The memristor is found to control the phase space even in the presence of inputs. The sine input is found to enhance synchrony and the square input controls the synchrony. The inputs with high frequency and optimum amplitude have high synchronising and desynchronising abilities. The influence of distance-dependent mean field coupling has been analysed in the memristive HR network. Square wave bursting is caused by the mean field coupling, while plateau bursting is caused by the memristors in the network. By using suitable values for both the memristor and mean field coupling, a combination of bursting patterns are induced. When memristor coupling is strong, the network shows an amplitude death state. In such a network, mean field coupling is capable of inducing synchronised bursts. The synchrony pattern under the influence of memristor coupling is quantified using the statistical factor of synchronisation. The interplay of memristors and uniform mean field coupling results in the emergence of coherent, MOS, imperfectly synchronised and perfectly synchronised states. The chimera states are obtained under the influence of distance-dependent coupling scheme. The parameter space for the strength of incoherence and discontinuity measure is also analysed.

- The chemically coupled HR network is analysed with cross interactions between membrane potential and magnetic flux. In a two coupled system, the network is synchronised for self and mixed interactions, but not for cross interactions. The stability of the synchrony is proven using MTLE. The synchrony pattern for the network for self, mixed and cross interactions is quantified using the statistical factor of synchronisation. Chimera and multichimera states are obtained which are verified by the strength of incoherence and discontinuity measure.
- The work has been extended to memristive HR network in a 2D lattice

with distance-dependent coupling governed by the power law exponent. The coordination number of each neuron is varied using coupling range. The threshold for coupling strength in terms of the coordination number is evaluated theoretically and numerically. In chemically coupled network, the threshold is independent of the network size, which is analysed using MTLE. The spatiotemporal patterns justify the fact that each 1D array shows different firing patterns for the same coupling strength. The snapshots of membrane potential shows that the 1D arrays also exhibit interesting patterns like desynchronised, chimera, multichimera and synchronised states.

- The emergence of spatial chimeras in a network of memristive HR neurons in 2D lattice with distance-dependent and cross coupling in chemical mode has been analysed. The self and mixed interactions induce synchrony and chimera states, whereas cross coupling is incapable of them. The spatial chimeras are observed as a result of network topology and interactions.
- The external inputs are capable of controlling synchrony in the HR network. The power law exponent reduces synchrony in the network and also induces chimera states, even in the globally coupled network. The emergence of chimera states in mixed and cross interactions is verified. The study shows that chimera states are induced in the network as a result of self interactions in multiple variables. In the electrically coupled network, the coupling threshold required to attain synchrony depends on the size of the network. However, in the chemically coupled network, the coupling threshold is independent of the network size. In the cross coupled network, synchrony is obtained in electrical mode whereas chemical coupling is incapable of inducing synchrony. Increasing the dimensionality and size of the network leads to the emergence of spatial chimeras.

9.2 Future prospects

There is significant difference between the synchronisation characteristics of one-dimensional and two-dimensional networks. When higher dimensions are used to analyse the network, its behaviour becomes more complex, which leads to the emergence of fascinating patterns. This highlights the importance of considering higher dimensions to achieve a more accurate representation of real world systems.

- There is ample scope for further study using various topologies, such as oscillators being positioned on the surface of a sphere or arranged in lattices inspired by solid-state physics, such as simple cubic, body-centered or face-centered configurations. These topologies shall be considered with distance-dependent interactions between oscillators, allowing to study the behaviour and function of networks in different contexts.
- The choice of random and small-world networks provides a better simulation of the connectivity in real neuron networks. Such networks could lead to a variety of interesting results and patterns.
- The heterogeneity in coupling schemes can lead to rich dynamics and open new directions for future research. Networks with mixed coupling of electrical, chemical and field interactions, with time-dependent coupling strengths, can exhibit interesting synchronisation behaviours. The dynamics of such a network can be highly complex and may result in various forms of synchronisation that are not observed in homogeneous networks.
- The work in 2D lattice can be extended to 3D network with distance-dependent and cross coupling. Proper selection of coupling strength and topology may yield interesting patterns such as spatial, spiral, spirally oscillating, rotating or 3D chimeras. These patterns may have wide spread applications in oscillatory biological networks like human heart and brain networks.

Bibliography

- [1] S. H. Strogatz, *Nonlinear dynamics and chaos: with applications to physics, biology, chemistry, and engineering* (CRC press, 2018).
- [2] J. D. Murray, *Mathematical Biology*, Springer **17** (2002).
- [3] M. I. Rabinovich, P. Varona, A. I. Selverston and H. D. Abarbanel, *Reviews of Modern Physics* **78**, p. 1213 (2006).
- [4] T. Nowotny, R. Huerta and M. I. Rabinovich, *Chaos: An Interdisciplinary Journal of Nonlinear Science* **18**, p. 5692 (2008).
- [5] E. R. Kandel, J. H. Schwartz, T. M. Jessell, S. Siegelbaum, A. J. Hudspeth, S. Mack *et al.*, *Principles of neural science* (McGraw-hill New York, 2000).
- [6] A. L. Hodgkin and A. F. Huxley, *The Journal of Physiology* **117**, p. 500 (1952).
- [7] E. M. Izhikevich and R. FitzHugh, *Scholarpedia* **1**, p. 1349 (2006).
- [8] E. M. Izhikevich, *IEEE Transactions on neural networks* **14**, 1569 (2003).
- [9] J. L. Hindmarsh and R. Rose, *Proceedings of the Royal society of London. Series B. Biological sciences* **221**, 87 (1984).
- [10] Y.-H. Liu and X.-J. Wang, *Journal of Computational Neuroscience* **10**, 25 (2001).
- [11] G. Innocenti, A. Morelli, R. Genesio and A. Torcini, *Chaos: An Interdisciplinary Journal of Nonlinear Science* **17**, p. 043128 (2007).
- [12] D. Jun, Z. Guang-Jun, X. Yong, Y. Hong and W. Jue, *Cognitive Neurodynamics* **8**, 167 (2014).
- [13] D. Hrg, *Neural Networks* **40**, 73 (2013).

- [14] Y. Xie, Z. Yao, G. Ren and J. Ma, *Physics Letters A* , p. 128693 (2023).
- [15] J. M. González-Miranda, *Chaos: An Interdisciplinary Journal of Nonlinear Science* **13**, 845 (2003).
- [16] X. Hu, G. Feng, S. Duan and L. Liu, *IEEE transactions on neural networks and learning systems* **28**, 1889 (2016).
- [17] N. Burić, D. Ranković, K. Todorović and N. Vasović, *Physica A: Statistical Mechanics and its Applications* **389**, 3956 (2010).
- [18] X. Shi and Z. Wang, *Nonlinear Dynamics* **69**, 2147 (2012).
- [19] L. Chua, *IEEE Transactions on circuit theory* **18**, 507 (1971).
- [20] D. B. Strukov, G. S. Snider, D. R. Stewart and R. S. Williams, *Nature* **453**, 80 (2008).
- [21] Y. Xu, H. Ying, Y. Jia, J. Ma and T. Hayat, *Scientific Reports* **7**, p. 43452 (2017).
- [22] Y. Xu, Y. Jia, J. Ma, T. Hayat and A. Alsaedi, *Scientific Reports* **8**, 1 (2018).
- [23] K. O. Stanley, J. Clune, J. Lehman and R. Miikkulainen, *Nature Machine Intelligence* **1**, 24 (2019).
- [24] S. Curteanu and H. Cartwright, *Journal of Chemometrics* **25**, 527 (2011).
- [25] A. E. Pereda, *The Journal of Physiology* **594**, p. 2561 (2016).
- [26] P. Balenzuela and J. García-Ojalvo, *Physical Review E* **72**, p. 021901 (2005).
- [27] M. Rosenblum and A. Pikovsky, *Physical Review E* **70**, p. 041904 (2004).

- [28] X. Miao, W. Zhang, Y. Shao, B. Cui, L. Chen, C. Zhang and J. Jiang, *IEEE Transactions on Knowledge and Data Engineering* (2021).
- [29] D. Erhan, Y. Bengio, A. Courville and P. Vincent, *University of Montreal* **1341**, p. 1 (2009).
- [30] I. Belykh, E. De Lange and M. Hasler, *Physical Review Letters* **94**, p. 188101 (2005).
- [31] X. Sun, Z. Liu and M. Perc, *Nonlinear Dynamics* **96**, 2145 (2019).
- [32] H. F. El-Nashar, Y. Zhang, H. A. Cerdeira and F. Ibiyinka A, *Chaos: An Interdisciplinary Journal of Nonlinear Science* **13**, 1216 (2003).
- [33] B. Kriener, M. Helias, S. Rotter, M. Diesmann and G. T. Einevoll, *Frontiers in Computational Neuroscience* **7**, p. 187 (2014).
- [34] E. Rybalova, A. Bukh, G. Strelkova and V. Anishchenko, *Chaos: An Interdisciplinary Journal of Nonlinear Science* **29**, p. 101104 (2019).
- [35] S. Guo, Q. Dai, H. Cheng, H. Li, F. Xie and J. Yang, *Chaos, Solitons & Fractals* **114**, 394 (2018).
- [36] B. Kriener, M. Helias, A. Aertsen and S. Rotter, *Journal of Computational Neuroscience* **27**, 177 (2009).
- [37] R. Budzinski, K. Rossi, B. Boaretto, T. Prado and S. Lopes, *Physical Review Research* **2**, p. 043309 (2020).
- [38] M. Strüber, J.-F. Sauer, P. Jonas and M. Bartos, *Nature Communications* **8**, p. 758 (2017).
- [39] A. Levina, J. M. Herrmann and T. Geisel, *Nature Physics* **3**, 857 (2007).
- [40] C. I. Bargmann and E. Marder, *Nature Methods* **10**, 483 (2013).

- [41] A. E. Pereda, *Nature Reviews Neuroscience* **15**, 250 (2014).
- [42] J. C. Magee, *Nature Neuroscience* **2**, 508 (1999).
- [43] J. Ma and J. Tang, *Science China Technological Sciences* **58**, 2038 (2015).
- [44] I. Koulierakis, D. Verganelakis, I. Omelchenko, A. Zakharova, E. Schöll and A. Provata, *Chaos: An Interdisciplinary Journal of Nonlinear Science* **30**, p. 113137 (2020).
- [45] Y. Zhao, X. Sun, Y. Liu and J. Kurths, *Nonlinear Dynamics* **93**, 1315 (2018).
- [46] S. Shirasaka, N. Watanabe, Y. Kawamura and H. Nakao, *Physical Review E* **96**, p. 012223 (2017).
- [47] G. Buzsaki, *Rhythms of the Brain* (Oxford university press, 2006).
- [48] J. Shlens, F. Rieke and E. Chichilnisky, *Current Opinion in Neurobiology* **18**, 396 (2008).
- [49] V. L. Galinsky and L. R. Frank, *Journal of Cognitive Neuroscience* **32**, 2178 (2020).
- [50] M. P. Richardson, *Journal of Neurology, Neurosurgery & Psychiatry* **83**, 1238 (2012).
- [51] S. P. Kelly, E. C. Lalor, R. B. Reilly and J. J. Foxe, *Journal of Neurophysiology* **95**, 3844 (2006).
- [52] X.-J. Wang, *Physiological Reviews* **90**, 1195 (2010).
- [53] N. C. Rattenborg, C. J. Amlaner and S. L. Lima, *Neuroscience & Behavioral Reviews* **24**, 817 (2000).

- [54] L. Khaleghi, S. Panahi, S. N. Chowdhury, S. Bogomolov, D. Ghosh and S. Jafari, *Physica A: Statistical Mechanics and its Applications* **536**, p. 122596 (2019).
- [55] A. Calim, P. Hövel, M. Ozer and M. Uzuntarla, *Physical Review E* **98**, p. 062217 (2018).
- [56] B. K. Bera, D. Ghosh and T. Banerjee, *Physical Review E* **94**, p. 012215 (2016).
- [57] G. R. Simo, P. Louodop, D. Ghosh, T. Njougouo, R. Tchitnga and H. A. Cerdeira, *Physics Letters A* **409**, p. 127519 (2021).
- [58] B.-W. Li and H. Dierckx, *Physical Review E* **93**, p. 020202 (2016).
- [59] R. Xu, X. Li, A. J. Boreland, A. Posyton, K. Kwan, R. P. Hart and P. Jiang, *Nature Communications* **11**, p. 1577 (2020).
- [60] M. Wickramasinghe and I. Z. Kiss, *Physical Chemistry Chemical Physics* **16**, 18360 (2014).
- [61] D. Dudkowski, K. Czołczyński and T. Kapitaniak, *Nonlinear Dynamics* **95**, 1859 (2019).
- [62] I. Omelchenko, E. Omel'chenko, P. Hövel and E. Schöll, *Physical Review Letters* **110**, p. 224101 (2013).
- [63] L. Gambuzza, L. Minati and M. Frasca, *Chaos, Solitons & Fractals* **138**, p. 109907 (2020).
- [64] B. K. Bera and D. Ghosh, *Physical Review E* **93**, p. 052223 (2016).
- [65] J. Hizanidis, V. G. Kanas, A. Bezerianos and T. Bountis, *International Journal of Bifurcation and Chaos* **24**, p. 1450030 (2014).

- [66] K. Usha, P. Subha and C. R. Nayak, *Chaos, Solitons & Fractals* **108**, 25 (2018).
- [67] Y. Kuramoto, *Chemical oscillations, waves and turbulence*. mineola (2003).
- [68] C. F. Stevens and A. M. Zador, *Nature Neuroscience* **1**, 210 (1998).
- [69] K. L. Rossi, R. C. Budziszki, J. A. P. Silveira, B. R. R. Boaretto, T. L. Prado, S. R. Lopes and U. Feudel, *arXiv preprint arXiv:2003.03289* (2020).
- [70] A. Wolf, J. B. Swift, H. L. Swinney and J. A. Vastano, *Physica D: nonlinear phenomena* **16**, 285 (1985).
- [71] K. Pyragas, *Physical Review E* **56**, p. 5183 (1997).
- [72] K.-S. Hong *et al.*, *Mathematics and Computers in Simulation* **82**, 590 (2011).
- [73] J. Heagy, T. Carroll and L. Pecora, *Physical Review E* **50**, p. 1874 (1994).
- [74] L. M. Pecora and T. L. Carroll, *Physical Review Letters* **80**, p. 2109 (1998).
- [75] L. M. Pecora, *Physical Review E* **58**, p. 347 (1998).
- [76] R. Gopal, V. Chandrasekar, A. Venkatesan and M. Lakshmanan, *Physical Review E* **89**, p. 052914 (2014).
- [77] A. Pikovsky and M. Rosenblum, *Chaos: An Interdisciplinary Journal of Nonlinear Science* **25**, p. 097616 (2015).
- [78] X. Zhang, A. Pikovsky and Z. Liu, *Scientific Reports* **7**, 1 (2017).
- [79] I. Ratas and K. Pyragas, *Physical Review E* **90**, p. 032914 (2014).
- [80] E. Baspinar, L. Schülen, S. Olmi and A. Zakharova, *Physical Review E* **103**, p. 032308 (2021).

- [81] H. Schmidt and D. Avitabile, *Chaos: An Interdisciplinary Journal of Nonlinear Science* **30**, p. 033133 (2020).
- [82] P. Bressloff, *Physical Review E* **60**, p. 2160 (1999).
- [83] J. Milton and P. Jung, *Epilepsy as a Dynamic Disease* , 341 (2003).
- [84] A. T. Winfree, *The Geometry of Biological Time* (Springer, 1980).
- [85] S. H. Strogatz, *Physica D: Nonlinear Phenomena* **143**, 1 (2000).
- [86] B. Lysyansky, O. V. Popovych and P. A. Tass, *Journal of Neural Engineering* **8**, p. 036019 (2011).
- [87] K. Usha and P. Subha, *Chinese Physics B* **28**, p. 020502 (2019).
- [88] L. Lu, M. Ge, Y. Xu and Y. Jia, *Physica A: Statistical Mechanics and its Applications* **535**, p. 122419 (2019).
- [89] M. Rosenblum, *Chaos: An Interdisciplinary Journal of Nonlinear Science* **30**, p. 093131 (2020).
- [90] Z. Yao, C. Wang, P. Zhou and J. Ma, *Communications in Nonlinear Science and Numerical Simulation* **95**, p. 105583 (2021).
- [91] M. Ogura and H. Kita, *Journal of Neurophysiology* **83**, 3366 (2000).
- [92] A. Cooper and I. Stanford, *Neuropharmacology* **41**, 62 (2001).
- [93] P. A. Tass, *Phase resetting in medicine and biology: stochastic modelling and data analysis* (Springer Science & Business Media, 2007).
- [94] D. Golomb, D. Hansel and G. Mato, Mechanisms of synchrony of neural activity in large networks, in *Handbook of Biological Physics*, (Elsevier, 2001), pp. 887–968.

- [95] C. Batista, S. R. Lopes, R. L. Viana and A. M. Batista, *Neural Networks* **23**, 114 (2010).
- [96] H. Zhang, Q. Wang and G. Chen, *Chaos: An Interdisciplinary Journal of Nonlinear Science* **24**, p. 033134 (2014).
- [97] C. Batista, R. Viana, F. Ferrari, S. Lopes, A. Batista and J. Coninck, *Physical Review E* **87**, p. 042713 (2013).
- [98] P. A. Tass, *Progress of Theoretical Physics Supplement* **139**, 301 (2000).
- [99] R. Ramasubbu, S. Lang and Z. H. Kiss, *Frontiers in Psychiatry* **9**, p. 302 (2018).
- [100] S. Santaniello, J. T. Gale and S. V. Sarma, *Wiley Interdisciplinary Reviews: Systems Biology and Medicine* **10**, p. e1421 (2018).
- [101] D. Hansel and H. Sompolinsky, *Physical Review Letters* **68**, p. 718 (1992).
- [102] C. Batista, E. Lameu, A. Batista, S. Lopes, T. Pereira, G. Zamora-López, J. Kurths and R. Viana, *Physical Review E* **86**, p. 016211 (2012).
- [103] H. Yamamoto, S. Kubota, F. A. Shimizu, A. Hirano-Iwata and M. Niwano, *Frontiers in computational neuroscience* **12**, p. 17 (2018).
- [104] S. Majhi and D. Ghosh, *Chaos: An Interdisciplinary Journal of Nonlinear Science* **28**, p. 083113 (2018).
- [105] T. Remi, P. Subha and K. Usha, *International Journal of Modern Physics C* **33**, p. 2250058 (2022).
- [106] F. P. Kemeth, S. W. Haugland, L. Schmidt, I. G. Kevrekidis and K. Krischer, *Chaos: An Interdisciplinary Journal of Nonlinear Science* **26**, p. 094815 (2016).

- [107] F. P. Kemeth, S. W. Haugland and K. Krischer, *Physical Review Letters* **120**, p. 214101 (2018).
- [108] S. Majhi, B. K. Bera, D. Ghosh and M. Perc, *Physics of Life Reviews* **28**, 100 (2019).
- [109] Y. Kuramoto and D. Battogtokh, *arXiv preprint cond-mat/0210694* (2002).
- [110] R. Levy, W. D. Hutchison, A. M. Lozano and J. O. Dostrovsky, *Journal of Neuroscience* **20**, 7766 (2000).
- [111] G. Ayala, M. Dichter, R. Gummit, H. Matsumoto and W. Spencer, *Brain Research* **52**, 1 (1973).
- [112] L. Schmidt, K. Schönleber, K. Krischer and V. García-Morales, *Chaos: An Interdisciplinary Journal of Nonlinear Science* **24**, p. 013102 (2014).
- [113] G. C. Sethia and A. Sen, *Physical Review Letters* **112**, p. 144101 (2014).
- [114] A. Mishra, C. Hens, M. Bose, P. K. Roy and S. K. Dana, *Physical Review E* **92**, p. 062920 (2015).
- [115] L. Schmidt and K. Krischer, *Physical Review Letters* **114**, p. 034101 (2015).
- [116] I. Omelchenko, A. Zakharova, P. Hövel, J. Siebert and E. Schöll, *Chaos: An Interdisciplinary Journal of Nonlinear Science* **25**, p. 083104 (2015).
- [117] C. R. Laing, *Physical Review E* **92**, p. 050904 (2015).
- [118] T. Banerjee, P. S. Dutta, A. Zakharova and E. Schöll, *Physical Review E* **94**, p. 032206 (2016).
- [119] S. A. Cannas and F. A. Tamarit, *Physical Review B* **54**, p. R12661 (1996).
- [120] S. Raghavachari and J. A. Glazier, *Physical Review Letters* **74**, p. 3297 (1995).

- [121] N. Uchida and R. Golestanian, *Physical Review Letters* **106**, p. 058104 (2011).
- [122] R. Golestanian, J. M. Yeomans and N. Uchida, *Soft Matter* **7**, 3074 (2011).
- [123] C. Anteneodo, S. E. d. S. Pinto, A. M. Batista and R. L. Viana, *Physical Review E* **68**, p. 045202 (2003).
- [124] H.-Y. Kuo and K.-A. Wu, *Physical Review E* **92**, p. 062918 (2015).
- [125] J. L. Rogers and L. T. Wille, *Physical Review E* **54**, p. R2193 (1996).
- [126] B. G. Szaro, R. Tompkins and B. G. Szaro, *Journal of Comparative Neurology* **258**, 304 (1987).
- [127] B. Bandyopadhyay, T. Khatun, P. S. Dutta and T. Banerjee, *Chaos, Solitons & Fractals* **139**, p. 110289 (2020).
- [128] Z. Faghani, Z. Arab, F. Parastesh, S. Jafari, M. Perc and M. Slavinec, *Chaos, Solitons & Fractals* **114**, 306 (2018).
- [129] E. A. Martens, M. J. Panaggio and D. M. Abrams, *New Journal of Physics* **18**, p. 022002 (2016).
- [130] S. Rakshit, B. K. Bera, M. Perc and D. Ghosh, *Scientific Reports* **7**, 1 (2017).
- [131] M. J. Panaggio and D. M. Abrams, *Physical Review E* **91**, p. 022909 (2015).
- [132] N. Burić, K. Todorović and N. Vasović, *Physical Review E* **78**, p. 036211 (2008).
- [133] I. Omelchenko, M. Rosenblum and A. Pikovsky, *The European Physical Journal Special Topics* **191**, 3 (2010).

- [134] S. Rakshit, B. K. Bera, D. Ghosh and S. Sinha, *Physical Review E* **97**, p. 052304 (2018).
- [135] L. L. Colgin, *Nature Reviews Neuroscience* **17**, 239 (2016).
- [136] E. Lee and D. Terman, *SIAM Journal on Applied Dynamical Systems* **14**, 448 (2015).
- [137] R. Vicente, L. L. Gollo, C. R. Mirasso, I. Fischer and G. Pipa, *Proceedings of the National Academy of Sciences* **105**, 17157 (2008).
- [138] B. Jia, Y. Wu, D. He, B. Guo and L. Xue, *Nonlinear Dynamics* **93**, 1599 (2018).
- [139] C. M. Lewis, A. Baldassarre, G. Committeri, G. L. Romani and M. Corbetta, *Proceedings of the National Academy of Sciences* **106**, 17558 (2009).
- [140] K. Shmueli, P. van Gelderen, J. A. de Zwart, S. G. Horovitz, M. Fukunaga, J. M. Jansma and J. H. Duyn, *Neuroimage* **38**, 306 (2007).
- [141] M. Corbetta and G. L. Shulman, *Nature Reviews Neuroscience* **3**, 201 (2002).
- [142] J. R. Simpson, A. Z. Snyder, D. A. Gusnard and M. E. Raichle, *Proceedings of the National Academy of Sciences* **98**, 683 (2001).
- [143] D. Mantini, M. G. Perrucci, C. Del Gratta, G. L. Romani and M. Corbetta, *Proceedings of the National Academy of Sciences* **104**, 13170 (2007).
- [144] S. G. Horovitz, A. R. Braun, W. S. Carr, D. Picchioni, T. J. Balkin, M. Fukunaga and J. H. Duyn, *Proceedings of the National Academy of Sciences* **106**, 11376 (2009).
- [145] G. S. Cymbalyuk, E. Nikolaev and R. Borisyuk, *Biological Cybernetics* **71**, 153 (1994).

- [146] R. Merrison-Hort and R. Borisyuk, *Frontiers in Computational Neuroscience* **7**, p. 173 (2013).
- [147] D. Li and C. Zhou, *Frontiers in Systems Neuroscience* **5**, p. 100 (2011).
- [148] A. G. Korotkov, A. O. Kazakov, T. A. Levanova and G. V. Osipov, *Communications in Nonlinear Science and Numerical Simulation* **71**, 38 (2019).
- [149] R. D. Pinto, P. Varona, A. Volkovskii, A. Szücs, H. D. Abarbanel and M. I. Rabinovich, *Physical Review E* **62**, p. 2644 (2000).
- [150] R. Erichsen Jr, M. Mainieri and L. Brunnet, *Physical Review E* **74**, p. 061906 (2006).
- [151] Z. Wang and Z. Liu, *Frontiers in Physiology* **11**, p. 724 (2020).
- [152] Z. Wang, Y. Xu, Y. Li, T. Kapitaniak and J. Kurths, *Chaos, Solitons & Fractals* **148**, p. 110976 (2021).
- [153] T. Remi, P. Subha and K. Usha, *Communications in Nonlinear Science and Numerical Simulation* **110**, p. 106390 (2022).
- [154] A. Zakharova, M. Kapeller and E. Schöll, *Physical Review Letters* **112**, p. 154101 (2014).
- [155] S. Kundu, B. K. Bera, D. Ghosh and M. Lakshmanan, *Physical Review E* **99**, p. 022204 (2019).
- [156] Y. Zhang and A. E. Motter, *Physical Review Letters* **126**, p. 094101 (2021).
- [157] M. Asllani, B. A. Siebert, A. Arenas and J. P. Gleeson, *Chaos: An Interdisciplinary Journal of Nonlinear Science* **32**, p. 013107 (2022).
- [158] K. Usha and P. Subha, *Nonlinear Dynamics* **96**, 2115 (2019).
- [159] R. Erichsen Jr and L. Brunnet, *Physical Review E* **78**, p. 061917 (2008).

- [160] A. Buscarino, M. Frasca, M. Branciforte, L. Fortuna and J. C. Sprott, *Nonlinear Dynamics* **88**, 673 (2017).
- [161] M. E. Yamakou, *Nonlinear Dynamics* **101**, 487 (2020).
- [162] Y. Xu, Y. Jia, J. Ma, A. Alsaedi and B. Ahmad, *Chaos, Solitons & Fractals* **104**, 435 (2017).
- [163] J.-Q. Yang, R. Wang, Z.-P. Wang, Q.-Y. Ma, J.-Y. Mao, Y. Ren, X. Yang, Y. Zhou and S.-T. Han, *Nano Energy* **74**, p. 104828 (2020).
- [164] L. Xu, G. Qi and J. Ma, *Applied Mathematical Modelling* **101**, 503 (2022).
- [165] K. Rajagopal, A. Karthikeyan, S. Jafari, F. Parastesh, C. Volos and I. Hussain, *International Journal of Modern Physics B* **34**, p. 2050157 (2020).
- [166] H. Bao, Y. Zhang, W. Liu and B. Bao, *Nonlinear Dynamics* **100**, 937 (2020).
- [167] K. Usha and P. Subha, *Biosystems* **178**, 1 (2019).
- [168] N. Zandi-Mehran, S. Jafari, S. M. R. Hashemi Golpayegani, F. Nazarimehr and M. Perc, *Nonlinear Dynamics* **100**, 1809 (2020).
- [169] F. Wu, J. Ma and G. Zhang, *Science China Technological Sciences* **63**, 625 (2020).
- [170] Y. Tan and C. Wang, *Chaos: An Interdisciplinary Journal of Nonlinear Science* **30**, p. 053118 (2020).
- [171] M. Chen, C.-j. Chen, B.-c. Bao and Q. Xu, Multi-stable patterns coexisting in memristor synapse-coupled hopfield neural network, in *Mem-elements for Neuromorphic Circuits with Artificial Intelligence Applications*, (Elsevier, 2021), pp. 439–459.

- [172] A. S. Eteme, C. B. Tabi and A. Mohamadou, *Communications in Nonlinear Science and Numerical Simulation* **72**, 432 (2019).
- [173] Z. Li, H. Zhou, M. Wang and M. Ma, *Nonlinear Dynamics* **104**, 1455 (2021).
- [174] M. Dhamala, V. K. Jirsa and M. Ding, *Physical Review Letters* **92**, p. 074104 (2004).
- [175] Y. Sakurai, K. Song, S. Tachibana and S. Takahashi, *Frontiers in Systems Neuroscience* **8**, p. 11 (2014).
- [176] P. J. Uhlhaas and W. Singer, *Neuron* **52**, 155 (2006).
- [177] A. Schnitzler and J. Gross, *Nature Reviews Neuroscience* **6**, 285 (2005).
- [178] M. Rosenblum, *Chaos: An Interdisciplinary Journal of Nonlinear Science* **30**, p. 093131 (2020).
- [179] H. Lin, C. Wang, W. Yao and Y. Tan, *Communications in Nonlinear Science and Numerical Simulation* **90**, p. 105390 (2020).
- [180] A. S. Eteme, C. B. Tabi, J. F. Beyala Ateba, H. P. Ekobena Fouda, A. Mohamadou and T. Crepin Kofane, *Nonlinear Dynamics* **105**, 785 (2021).
- [181] P. Kalle, J. Sawicki, A. Zakharova and E. Schöll, *Chaos: An Interdisciplinary Journal of Nonlinear Science* **27**, p. 033110 (2017).
- [182] S. Majhi, M. Perc and D. Ghosh, *Scientific Reports* **6**, 1 (2016).
- [183] R. P. Feynman, R. B. Leighton and M. Sands, *American Journal of Physics* **33**, 750 (1965).
- [184] M. Lv, J. Ma, Y. Yao and F. Alzahrani, *Science China Technological Sciences* **62**, 448 (2019).

- [185] F. Devalle, E. Montbrió and D. Pazó, *Physical Review E* **98**, p. 042214 (2018).
- [186] B. M. Adhikari, A. Prasad and M. Dhamala, *Chaos: An Interdisciplinary Journal of Nonlinear Science* **21**, p. 023116 (2011).
- [187] S. Saha, A. Mishra, P. K. Roy and S. K. Dana, *Opera Medica et Physiologica*, 93 (2017).
- [188] X. Liang, M. Tang, M. Dhamala and Z. Liu, *Physical Review E* **80**, p. 066202 (2009).
- [189] M. Kivela, A. Arenas, M. Barthelemy, J. P. Gleeson, Y. Moreno and M. A. Porter, *Journal of Complex Networks* **2**, 203 (2014).
- [190] M. De Domenico, C. Granell, M. A. Porter and A. Arenas, *Nature Physics* **12**, 901 (2016).
- [191] L. V. Gambuzza, M. Frasca, L. Fortuna and S. Boccaletti, *Physical Review E* **93**, p. 042203 (2016).
- [192] M. Vaiana and S. F. Muldoon, *Journal of Nonlinear Science* **30**, 2147 (2020).
- [193] S. Boccaletti, G. Bianconi, R. Criado, C. I. Del Genio, J. Gómez-Gardenes, M. Romance, I. Sendina-Nadal, Z. Wang and M. Zanin, *Physics Reports* **544**, 1 (2014).
- [194] N. S. Frolov, V. A. Maksimenko, M. V. Khramova, A. N. Pisarchik and A. E. Hramov, *The European Physical Journal Special Topics* **228**, 2381 (2019).
- [195] F. Drauschke, J. Sawicki, R. Berner, I. Omelchenko and E. Schöll, *Chaos: An Interdisciplinary Journal of Nonlinear Science* **30**, p. 051104 (2020).

- [196] Y. Yao, H. Deng, M. Yi and J. Ma, *Scientific Reports* **7**, 1 (2017).
- [197] M. Shafiei, S. Jafari, F. Parastesh, M. Ozer, T. Kapitaniak and M. Perc, *Communications in Nonlinear Science and Numerical Simulation* **84**, p. 105175 (2020).
- [198] M. Dhamala, V. K. Jirsa and M. Ding, *Physical Review Letters* **92**, p. 028101 (2004).
- [199] F. P. Ulloa Severino, J. Ban, Q. Song, M. Tang, G. Bianconi, G. Cheng and V. Torre, *Scientific Reports* **6**, 1 (2016).
- [200] A. Koch and H. Meinhardt, *Reviews of Modern Physics* **66**, p. 1481 (1994).
- [201] D. Dudkowski, Y. Maistrenko and T. Kapitaniak, *Physical Review E* **90**, p. 032920 (2014).
- [202] Y. Wang, D. Song, X. Gao, S.-X. Qu, Y.-C. Lai and X. Wang, *Nonlinear Dynamics* **93**, 1671 (2018).
- [203] J. Ma, J. Tang, A. Zhang and Y. Jia, *Science China Physics, Mechanics and Astronomy* **53**, 672 (2010).
- [204] I. Omelchenko, A. Provata, J. Hizanidis, E. Schöll and P. Hövel, *Physical Review E* **91**, p. 022917 (2015).
- [205] T. Remi and P. A. Subha, *Journal of biological physics* , 1 (2023).
- [206] T. Remi and P. Subha, *Journal of Physics A: Mathematical and Theoretical* **56**, p. 345701 (2023).
- [207] S. Kundu, S. Majhi, P. Muruganandam and D. Ghosh, *The European Physical Journal Special Topics* **227**, 983 (2018).
- [208] A. Schmidt, T. Kasimatis, J. Hizanidis, A. Provata and P. Hövel, *Physical Review E* **95**, p. 032224 (2017).

- [209] M. J. Panaggio and D. M. Abrams, *Physical Review Letters* **110**, p. 094102 (2013).
- [210] E. A. Martens, C. R. Laing and S. H. Strogatz, *Physical Review Letters* **104**, p. 044101 (2010).
- [211] K. Rajagopal, S. Jafari, C. Li, A. Karthikeyan and P. Duraisamy, *Chaos, Solitons & Fractals* **146**, p. 110855 (2021).